

**AN ELECTRICALLY SMALL, WIRELESS SENSOR  
PLATFORM DESIGNED FOR ARBITRARY  
ORIENTATION**

**A Thesis  
Submitted to the Graduate Faculty  
of the  
North Dakota State University  
of Agriculture and Applied Science**

**By**

**Layne Albert Berge**

**In Partial Fulfillment of the Requirements  
for the Degree of  
MASTER OF SCIENCE**

**Major Department:  
Electrical and Computer Engineering**

**March 2013**

**Fargo, North Dakota**

North Dakota State University  
Graduate School

---

Title

An Electrically Small, Wireless Sensor Platform Designed for Arbitrary  
Orientation

---

By

Layne Albert Berge

---

The Supervisory Committee certifies that this *disquisition* complies with North Dakota State  
University's regulations and meets the accepted standards for the degree of

**MASTER OF SCIENCE**

SUPERVISORY COMMITTEE:

Dr. Michael T. Reich

---

Chair

Dr. Benjamin D. Braaten

---

Dr. David A. Rogers

---

Dr. Orven F. Swenson

---

Approved:

March 28, 2013

---

Date

Dr. Rajendra Katti

---

Department Chair

## ABSTRACT

Wireless sensors are currently used for data collection where it is either too dangerous and/or menial for a human to collect the data or impractical to use wired devices. Current wireless sensors are either too expensive or have too short of a battery life in order to be useful. The wireless sensor platform developed in this work solves these issues by using the RFID communications protocol. This allows for low-power communications while using inexpensive hardware. The sensor has been tested and shown to exhibit a near-isotropic radiation pattern, allowing the placement orientation to be uncontrolled. The antenna design exhibits two separate tuning mechanisms, allowing the antenna to be tuned for different UHF RFID ICs or different UHF RFID frequency spectrums. The wireless sensor platform currently is capable of taking temperature measurements and interfacing with additional sensor electronics via serial communications.

## ACKNOWLEDGEMENTS

The number of people who have helped me up to this point is beyond measure. No matter the contribution, from words of encouragement to hours of assistance, you have my deepest gratitude. I will, however, attempt to mention those most responsible for the completion of this thesis and my degree.

First, I would like to thank Aaron Reinholz at the Center for Nanoscale Science and Engineering (CNSE). Aaron made possible my graduate studies at CNSE. More importantly, however, I thank Aaron for hiring me during my first year of college. I would not be where I am at today if it were not for CNSE.

I would also like to thank Nathan Schneck at CNSE. His help was invaluable in building the prototypes for this thesis. In addition, the work that he did for the demonstration at my defense was invaluable. His time and encouragement made this thesis possible.

Next, I would like to thank my committee members: Dr. Michael T. Reich, Dr. Benjamin D. Braaten, Dr. David A. Rogers, and Dr. Orven F. Swenson. They made it possible for me to complete my degree at an accelerated pace. Special thanks goes to Dr. Braaten for encouraging me to pursue research early. His constant encouragement and guidance helped me to complete graduate classes during my undergraduate studies and to navigate the publication process. By far, however, the most thanks goes to Dr. Reich and Cherish Bauer-Reich. The years of guidance and support they both gave me while working at CNSE gave me the ability to continue on towards a graduate degree. Besides knowledge, his tolerance of me early on while working at CNSE is deeply appreciated. My pursuit of a master's degree started with his question early on: "Would you stay for a master's degree if it only took a year?" The support and encouragement by both Mike and Cherish throughout coursework, publications, and research helped me to arrive where I am at today.

Lastly, I would like to thank my parents. Their endless encouragement and support, through grade school and college, helped define who I am today. Listening to my ideas, no matter how nonsensical, from a very young age with patience taught me to refine and pursue my passions. Thank you for always guiding me with love and compassion.

This material is based on research sponsored by the Defense Microelectronics Activity under agreement number H94003-11-2-1102. The United States Government is authorized to reproduce and distribute reprints for government purposes, notwithstanding any copyright notation thereon.

## DEDICATION

To my parents, Don and Terry.

Thanks for always being there for me, Mom and Dad.

*For where your treasure is, there will your heart be also.*

Fortunately, my treasure is not here...

# TABLE OF CONTENTS

ABSTRACT.....	iii
ACKNOWLEDGEMENTS.....	iv
DEDICATION.....	vi
LIST OF TABLES.....	x
LIST OF FIGURES.....	xi
CHAPTER 1. INTRODUCTION.....	1
1.1. RF: The Beginning.....	1
1.2. RFID.....	2
1.3. Wireless Sensors.....	3
1.4. Project Motivation.....	4
CHAPTER 2. THEORETICAL BACKGROUND.....	6
2.1. Electromagnetic Propagation.....	6
2.2. Antenna Theory.....	11
2.3. Impedance Matching.....	15
2.4. RFID.....	20
CHAPTER 3. PREVIOUS WORK.....	24
3.1. Wireless Sensor Designs.....	24
3.2. Previous Antenna Designs for Wireless Sensors.....	29
CHAPTER 4. SIMULATION SETUP AND VALIDATION.....	33
4.1. Model Setup.....	33

4.2. Simulation Results.....	36
CHAPTER 5. ANTENNA DESIGN AND SIMULATION.....	39
5.1. Design Goals.....	39
5.2. Initial Spherical-Cap Single Dipole Design .....	41
5.3. Spherical-Cap Double Dipole Design.....	48
CHAPTER 6. ANTENNA PROTOTYPING AND MEASUREMENT .....	61
6.1. Constructing the Prototype.....	61
6.2. Testing the Prototype Antenna .....	64
6.3. Results of the Prototype Antenna.....	68
6.4. Design Repeatability .....	74
CHAPTER 7. SENSOR ELECTRONICS INTEGRATION.....	78
7.1. Multifunctional RFID IC .....	78
7.2. Initial Wireless Sensor Design .....	79
7.3. IDS Wireless Sensor Simulation and Construction .....	81
7.4. IDS Wireless Sensor Testing and Results.....	84
CHAPTER 8. CONCLUSIONS.....	88
REFERENCES.....	91
APPENDIX A. MATLAB CODE.....	98
A.1. Simulated Data Plotting .....	98
A.2. Simulated to Measured Radiation Pattern Comparison ....	113
A.3. Pattern Interpolation.....	116
A.4. MEG and Gain Calculations .....	117



A.5. MEG Function .....	119
APPENDIX B. PYTHON CODE.....	120
B.1. Measured Maximum Read Range Plotting .....	120

## LIST OF TABLES

<u>Table</u>	<u>Page</u>
3.1. Comparison of previous antenna designs.....	31
5.1. Bandwidth and operating frequency comparison between double dipole antenna designs. Included are the cap heights, $h$ , and the series inductor value used for each design. ....	58
5.2. Gain comparison between antenna designs.....	59
7.1. Dimensional, bandwidth, and operating frequency comparison between the antenna design utilizing the Higgs 3 IC and the IDS IC.....	81
7.2. Gain comparison between the Higgs 3 antenna design and the IDS design.	84

## LIST OF FIGURES

<u>Figure</u>	<u>Page</u>
2.1. TEM wave propagation, as shown in [8]. .....	7
2.2. A typical dipole antenna and a radiation pattern typical of the antenna type. ....	12
2.3. A typical horn antenna and a radiation pattern typical of the antenna type. ....	13
2.4. Spherical coordinate system [8]. ....	14
2.5. Typical matching circuits. ....	17
2.6. Examples of a parallel stub match and a quarter-wave transformer. ....	18
4.1. The antenna design presented in [40]. ....	33
4.2. The antenna design presented in [40] as modeled in HFSS. ....	35
4.3. Negative return loss plot for the antenna design, as shown in Figure 2a of [40]. ....	37
4.4. Negative return loss plot for the antenna design in [40], simulated in HFSS and shown modeled in Figure 4.2. ....	38
5.1. Drawing of the single dipole, spherical-cap design. The Feed Wire connects to the inside, center of the spherical-cap. ....	42
5.2. HFSS model of the spherical-cap, single dipole antenna with a 1 mm thick ABS shell. ....	43
5.3. PRC and impedance plots comparing the performance of two iterations of the single dipole design shown in Figure 5.2. ....	45
5.4. HFSS model of the helical-coil, spherical-cap, single dipole antenna with a 1 mm thick ABS shell. ....	46
5.5. PRC and impedance plots for the helical-coil, spherical-cap single dipole design shown in Figure 5.4. ....	47

5.6.	Radiation pattern plots (E-field) for the three principal planes for the antenna shown in Figure 5.4 at 915 MHz.....	48
5.7.	HFSS model of the helical-coil, spherical-cap, double dipole antenna with a 1 mm thick ABS shell.....	49
5.8.	HFSS model of the spherical-cap double dipole antenna with PCB and a 1 mm thick ABS shell. ....	50
5.9.	The PCB design used for sensor electronics and matching components in the double dipole antenna. ....	51
5.10.	HFSS model of the second double dipole design option, with one antenna leg skewed by 90 degrees. ....	52
5.11.	HFSS model of the third double dipole design option, with two legs skewed by 90 degrees. Note how the legs all reside in the upper hemisphere of the spherical volume. ....	53
5.12.	ADS layout for the test microstrip transmission line with a characteristic impedance of 50 $\Omega$ . ....	54
5.13.	ADS schematic for the test microstrip transmission line with a characteristic impedance of 50 $\Omega$ . ....	55
5.14.	ADS layout to determine the characteristic impedance of the antenna traces used in the spherical-cap, double dipole antenna design. ....	56
5.15.	ADS schematic to determine the characteristic impedance of the antenna traces used in the spherical-cap, double dipole antenna design. ....	57
5.16.	PRC comparison between the three double dipole designs. ....	58
5.17.	Simulated, normalized, electric field intensity patterns for the prototype antenna shown in Figure 5.8 at 915 MHz.....	60
6.1.	Assembly of the antenna. ....	62
6.2.	The fully assembled PCB shown placed into the bottom hemisphere of the ABS shell. ....	63
6.3.	Exploded antenna showing the top and bottom hemispheres of the ABS shell and the completed PCB.....	64

6.4.	Partially assembled antenna. ....	65
6.5.	Fully assembled wireless sensor antenna. ....	65
6.6.	Complete measurement test setup. ....	66
6.7.	Relative radiation pattern measurements given as maximum read distance calculated using Equation 6.1. The units are in mm. ....	69
6.8.	Normalized plot, comparing the simulated PRC for the prototype antenna to the measured minimum turn-on power. ....	71
6.9.	Normalized radiation pattern comparison at 915 MHz between the simulated total electric field intensity, shown in Figure 5.17, and the minimum read range plot, shown in Figure 6.7. ....	74
6.10.	Normalized plot, comparing the measured minimum turn-on power between the four prototype antennas. ....	75
6.11.	Normalized radiation pattern plots comparing the minimum read range between the four prototype antennas at 915 MHz. ....	75
6.12.	Normalized radiation pattern plots comparing the minimum read range between the four prototype antennas at 965 MHz. ....	77
7.1.	Model of the antenna and PCB used to test the wireless sensor utilizing the IDS RFID IC [55]. The IDS IC allows for temperature measurements internally and external control of additional sensor electronics. ....	80
7.2.	PRC comparison between the antenna design for the Higgs 3 IC and the design for the IDS IC. ....	82
7.3.	Simulated, normalized, electric field intensity patterns for the IDS IC antenna design. The plots are from simulation results. ....	83
7.4.	PCB design used for the IDS IC based wireless sensor antenna. ....	84
7.5.	Relative radiation pattern measurements given as maximum read distance calculated using Equation 6.1. The units are in mm. ....	85
7.6.	Normalized plot, comparing the simulated PRC for the IDS IC antenna to the measured minimum turn-on power. ....	86

7.7. Normalized radiation pattern comparison between the simulated total electric field intensity and the minimum read range plot shown in Figure 6.7 at 915 MHz..... 87

7.8. Comparison between the measured maximum read range for the Higgs 3 antenna design (Sphere1) and the IDS antenna design (IDS1) at 915 MHz. .... 87

# CHAPTER 1. INTRODUCTION

## 1.1. RF: The Beginning

When Guglielmo Marconi sent the first wireless message across a channel of water in the spring of 1897, he began a revolution in communication. The effects of the information he later sent across the English Channel sent ripples of understanding through the consciousness of the public on the possibilities for communication via radio waves. However, Marconi simply utilized a natural phenomenon present in the world and noticed by mankind since the first rays of sunlight lit the faces of humans, electromagnetic radiation. Years before Marconi utilized electromagnetic radiation for communications, physicists theorized the existence and interactions of electric charges and currents. With the foundational studies from Gauss, Faraday, and Ampère, James Maxwell formulated his famous set of differential equations describing electromagnetic radiation. With the later recasting of these equations by Oliver Heaviside into their current form, along with the experiments by Heinrich Hertz, the fruits of these scientists along with many others sat ready to be picked by Marconi.

The work started by Marconi resulted in the increased speed and frequency of communication. Trans-Atlantic wireless messages soon became commonplace. It was not until the Second World War however, that a new usage for radio waves became known. The warplanes of World War I soon transitioned from using wood and fabric to metal for World War II. These flying metal bodies, while faster and more deadly than their wood and fabric brethren, made possible the use of microwaves for detection, long before they came into view of even the most ardent watch-soldier. The use of microwaves in this manner was known as radar. In contrast to typical radio communication, where communication takes place between two active radio systems, radar utilizes the passive response of other objects. In the Battle of Britain, as the German Luftwaffe would cross the English Channel, British radar units effectively

received and interpreted this backscatter from German fighters and bombers to track and shoot down the enemy aircraft before they reached their targets [1]. The use of radar allowed the besieged country of Britain to prevail against the Germans and marked a turning point in the war.

Radar utilizes a transmitter and receiver pair. The receiver is tuned in order to pick up the reflections of the transmitted signal from other objects. In the beginning, however, this information only told radar operators that other aircraft or reflecting objects were present, not whether they were friend or foe. Soon, transponders were added to aircraft which relayed basic information about the aircraft including its own identification number and altitude [2]. This radar, aircraft and transponder setup represents the basis for current radio frequency identification (RFID) systems today.

## **1.2. RFID**

Most objects a person purchases today have printed on it a universal product code (UPC), better known as a barcode. When the customer reaches the checkout aisle at their local shop, the cashier scans the bar code with an optical reader. The reader scans the barcode and analyzes the light reflected back. Depending on the geometric properties of each bar, the reader interprets the data as a binary 1 or 0. This data then points to a database where the name, description, and price of the item is stored. This entire identification process, known as automated identification (auto-ID), attempts to bring the efficiency of a computer to the mundane task of product management. However, barcodes have disadvantages. While inexpensive, they require the reader to come within centimeters of the object. Additionally, the barcodes are easily damaged, rendering their data useless. The data that they do hold is limited and cannot be changed. RFID changes this. Instead of ink bars and an optical reader, the barcode is replaced with an RFID tag, which uses an antenna with an RFID integrated circuit (IC). The information an RFID IC holds is much



greater than a barcode, in addition to being re-writable. This allows the tag to store more information, including information tracking the tagged product throughout its product lifecycle. Additionally, certain RFID tags can be read from meters away, without the reader actually needing to visually see the tag; in other words, an item hidden in a box placed across a room from the reader can still be read. The tag itself is durable, only damaged when the tag is ripped or severely bent [2].

Even though an RFID IC is more complex than a barcode, it is still able to operate as a passive device, which does not need batteries. The RFID reader operates by sending out a signal. This signal powers up the RFID IC. A small amount of this signal is then reflected back from the RFID tag, which the tag modulates, or encodes information onto, in order to send information to the reader. Using this query signal and backscattered response, the reader and tag send information between each other. This allows for a two-way communication channel not possible with a barcode. This communications protocol requires no external power to be supplied to the tag. This is advantageous not only for RFID tags in auto-ID applications but also for other uses where the object on one end of a radio link needs to be low-power or entirely passive [2].

### **1.3. Wireless Sensors**

In the late 1990's, researchers demonstrated the feasibility of integrating advanced sensing electronics with a micro-controller and radio transceiver electronics package to implement a wireless sensor platform called "smart dust". The goal for this project was to create a long-term wireless sensor with a one cubic millimeter volume, which was inexpensive to manufacture and deploy in volume [3]. With these sensors, researchers planned on monitoring everything from bridge decks to volcanoes, where data collection by humans was too mundane or too dangerous [4]. However, the battery life for such devices was only one day [3]. The radio communications

protocol used to gather data placed too great of a burden on the energy reserves of the wireless sensors. Recently though, RFID protocols have been proposed in order to circumvent this issue [4], [5], [6]. Instead of the sensor transmitting data actively back to the measurement device, the sensor uses RFID protocol for data transmission. This offers a low-power method for data transmission by the wireless sensor versus the dedicated on-board radio electronics previously used. Additionally, the sensor is able to harvest power from the measurement device. The sensor then uses this harvested power to perform measurements as well as recharging any onboard energy storage devices. This type of sensor, when used en masse, is known as an RFID sensor network (RSN).

A prominent research project currently is the WISP project [4], [5]. WISP stands for wireless identification and sensing platform, and is an advanced form of an RSN. A WISP contains advanced computational electronics over a traditional RSN. In [4], the authors outline the feasibility of using RSNs for long-term sensing applications. Examples of these applications are temperature monitoring in health care products, activity monitoring for the elderly and body implantable sensors. The authors outline how, using an energy storage device, the RSN is able to continuously sense parameters even while not being read by the measurement device. This is important since this allows the RSN to complete its sensing capabilities without needing a replaceable battery. The energy storage device powers the electronics while not being read and it is recharged when transferring data to the measurement device.

#### **1.4. Project Motivation**

HR 658, a House Resolution passed in the year 2012 by the United States Congress, tasked the Federal Aviation Administration (FAA) with the creation of rules allowing for unmanned aerial vehicles (UAVs) to share airspace with other manned flights by the year 2015. Use of a UAV offers a powerful tool for corporations,

government organizations and individuals to increase the speed and efficiency of data collection [7]. A UAV also seems to be an excellent vehicle for the deployment of RSNs. Just as the original smart-dust project specified deploying sensors in a widespread, high-density pattern, a UAV could accomplish the same with a new wireless sensor platform tailored for the task. A UAV loaded with several wireless sensors would fly over a zone of interest and deploy them from an internal cargo bay. Upon landing, the sensors would begin collecting data at a set interval appropriate for the intended application. The UAV would then be programmed to fly over the RSN on a regular basis. On the underside of the UAV, a reader would query the sensors, gathering data as well as recharging any onboard energy storage devices.

This outlined scenario is the overarching objective for the work presented in this thesis work. The wireless sensor platform for such an RSN needs to achieve certain goals. It must be small and inexpensive in order to be deployed in sufficient numbers from a UAV. The sensor needs to be immune to orientation because orientation will not be controlled when the sensors are deployed from a UAV. In addition, there needs to be space for sensor electronics in the sensor platform design. Because the electronics for such a sensor are already developed, as shown by [4], [5] and [6], the focus of this project will be on the antenna design and sensor platform. The antenna will need to operate in the RFID spectrum for the United States. As mentioned previously, it needs to be immune to orientation. This ensures that every sensor deployed is able to communicate wirelessly. The sensor platform needs to be inexpensive but also rugged enough for long-term deployment by a UAV into a variety of harsh conditions. Wireless sensors exhibiting these attributes will greatly expand the current abilities to collect data autonomously.

## CHAPTER 2. THEORETICAL BACKGROUND

Before detailing the design of the new wireless sensor platform, a review of the relevant theory behind electromagnetic propagation, antennas and RFID protocol is necessary. While this review is nowhere near all-encompassing, the reader will benefit from knowing the terms and theory behind the creation of a wireless sensor utilizing RFID. It is assumed the reader has knowledge of vector calculus, familiarity with the general layout and function of radio transceivers, and communication protocols.

### 2.1. Electromagnetic Propagation

From the differential form of Maxwell's equations, a time-varying electric field induces a time-varying magnetic field and vice versa. One cannot exist in a time varying fashion without the other. These time-varying electromagnetic fields also contain energy and power. The amount and direction of this power is written as

$$\bar{\mathcal{S}} = \bar{\mathcal{E}} \times \bar{\mathcal{H}}, \quad (2.1)$$

where  $\bar{\mathcal{S}}$  is known as the Poynting vector and has units of power density (watts/square meter). Taking Equation 2.1 and integrating it over a closed surface results in

$$\mathcal{P}_e = \oiint_S (\bar{\mathcal{E}} \times \bar{\mathcal{H}}) \cdot d\mathbf{s} = \oiint_S \bar{\mathcal{S}} \cdot d\mathbf{s} \quad (2.2)$$

where  $\mathcal{P}_e$  is the total power exiting the closed surface, typically a sphere. The important result from Equation 2.2 is that a propagating wave is transporting energy. This means that when an electromagnetic wave is used to send information over long distances (in tele-communications for instance) it requires some amount of power.

This then segues into methods of propagation. The magnetic and electric fields do not simply travel in any orientation. There exist certain field configurations that support propagation. These configurations are known as modes [8]. For this thesis

work, the TEM mode, or transverse electromagnetic mode is applicable. This mode places the electric and magnetic field intensities orthogonal to each other. Both of these are then orthogonal to the direction of propagation. Figure 2.1, taken from [8], illustrates TEM mode propagation. In the figure, the complex spatial form of the electric and magnetic field vectors,  $\mathbf{E}$  and  $\mathbf{H}$  respectively, are orthogonal to each other. The three separate instances in the figure illustrate that at each position, the field vectors are also orthogonal to the propagation vector,  $\mathbf{v}$ , at that point, whose direction is given by  $\hat{\mathbf{n}}$ . Using the right-hand rule allows a person to determine the direction of propagation. Aligning the hand with the direction of  $\mathbf{E}$  and curling the fingers toward  $\mathbf{H}$ , the thumb will point in the direction of propagation. This method also gives a visual method of explaining Equation 2.1. The direction of propagation is synonymous with the direction of power.

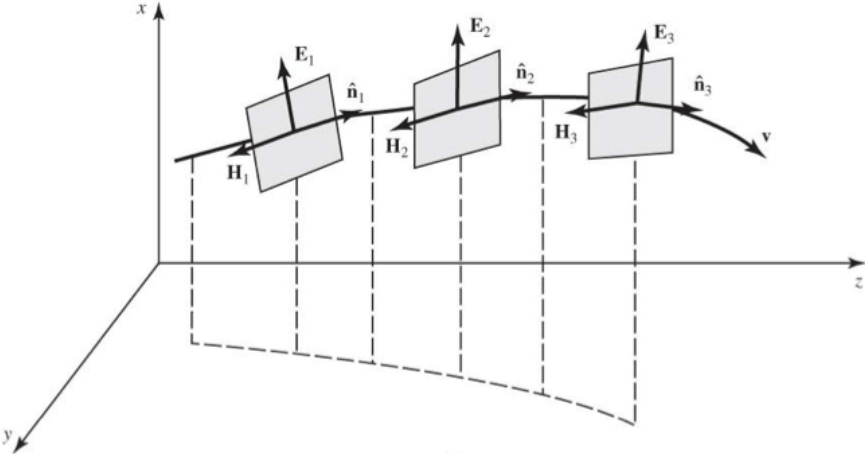


Figure 2.1. TEM wave propagation, as shown in [8].

Because the wave propagates through mediums other than a vacuum, it helps to characterize properties of the propagating wave according to the medium through

which it is propagating. Maxwell's equations state that both the electric and magnetic fields must be present. Depending on the medium, the magnitude of each in relation to the other is different. This is known as the wave impedance and is given as

$$Z_w = \eta = \frac{|\mathbf{E}|}{|\mathbf{H}|} = \sqrt{\frac{\mu}{\epsilon}} \quad (2.3)$$

where  $Z_w$  is synonymous with the *intrinsic impedance* of the medium,  $\eta$  [8]. In addition,  $\mu$  and  $\epsilon$  are known as the permeability and the permittivity of the medium in Equation 2.3.

Besides the medium dependent magnitude relation between electric and magnetic fields, the speed at which the wave propagates is also determined by the medium. The speed at which the wave propagates in an infinite medium is given as

$$v_e = \frac{1}{\sqrt{\mu\epsilon}} \quad (2.4)$$

where  $v_e$  is known as the energy (group) velocity [8]. In a more general form,  $v_e$  is given in [9] as

$$v_e = \left. \frac{\partial\omega}{\partial\beta} \right|_{\omega_0} \quad (2.5)$$

where  $\omega$  is the radian frequency and  $\omega_0$  is the frequency where the energy velocity is evaluated.  $\beta$  is known as the phase constant (wavenumber) and is given in [10] for a lossless medium as

$$\beta = \omega\sqrt{\mu\epsilon}. \quad (2.6)$$

Energy velocity should not be confused with phase velocity, despite the equation for phase velocity of a TEM mode being identical to Equation 2.4. Anyone familiar with the work of Einstein knows that the energy velocity cannot exceed that of light in a vacuum. However, phase velocity for an oblique wave (common in waveguides)

exceeds the speed of light, while energy velocity always is equal to or less than the speed of light in a vacuum. This is an important point to emphasize, since TEM mode propagation represents only one case of wave propagation.

When a wave passes from one medium to another, more than just magnitude ratios and velocity changes take place. Examining only the electric field, a wave propagating in a lossless medium in the  $z$  direction has an electric field intensity given as

$$E(z) = E_0^+ e^{-j\beta z} + E_0^- e^{j\beta z} \quad (2.7)$$

where the  $+$  superscript indicates a forward traveling wave and the  $-$  superscript indicates a backward traveling wave. When a wave impinges on a boundary between two different mediums, a reflection occurs. Since the goal of wave propagation is to maximize the magnitude of the wave at the receiving end, it is important to minimize the backward traveling wave. Using Equation 2.7, a good metric for analyzing reflections is given as

$$\Gamma = \frac{E_r}{E_i} \quad (2.8)$$

where the  $i$  subscript indicates an incident wave, the  $r$  subscript indicates a reflected wave, and  $\Gamma$  is the *reflection coefficient* at  $z = 0$  [8].

The magnitude of the reflection coefficient,  $|\Gamma|$ , ranges between 0 and 1, with 0 representing no reflection and 1 representing a total reflection at the boundary between the two mediums by the propagating wave. The presence of reflections in a medium results in a phenomenon called a *standing wave*. A standing wave is a product of the constructive and destructive interference between the forward and backward traveling waves. This product creates a wave where position is not a function of time. This then results in points where the total wave is greater than or less than the forward traveling wave alone [8], [9]. SWR, or standing wave ratio, is a metric

for standing waves. SWR is typically used because instruments can directly measure it. It is better known as VSWR, or voltage standing wave ratio, since it is typically easier to measure voltage rather than current. It is given in [8] as

$$SWR = \frac{1 + |\Gamma|}{1 - |\Gamma|}. \quad (2.9)$$

The final topic is that of *wave polarization*. While wave polarization is complex, a simple explanation will suffice for the work presented here. Previously, it was stated that the electric field vector and magnetic field vector for TEM mode propagation are perpendicular. While this is true, it does not mean they remain oriented in a fixed direction. Often, the vectors will rotate around the vector of propagation. This is known as the polarization of the wave. There exist different types of polarization for a propagating wave. The first is *linear polarization*. This means the electric and magnetic field vector directions remain fixed. The next is *elliptical polarization*. If a person traced the end of a single field vector (either electric or magnetic) over time, the subsequent trace would resemble an ellipse. A special case of this is *circular polarization*. This means the field trace over time resembles a circle [9].

The direction which these vectors rotate is also important. The rotational direction is defined by the vectors either rotating in a clockwise or counterclockwise direction. This is also known as right-hand and left-hand orientation. The hand nomenclature is based upon the direction of propagation of the wave. Placing the thumb in the direction of propagation, if the fingers of the right hand curl in the direction of rotation, it is right-hand polarized. The same is true for the left hand and left-hand polarization. Whether it is clockwise or counterclockwise is based on the observer viewing the wave propagating away from their viewpoint. With the thumb pointing away from the observer, right-hand polarized is the same as clockwise and left-hand polarized is the same as counterclockwise [11]. The reader can find more



information about polarization in [8], [9], and [11]. Polarization is important when considering what type of antenna to use in order to effectively transmit and receive a TEM mode, propagating wave.

## 2.2. Antenna Theory

While Section 2.1 described the importance of wave propagation for wireless communication, it is useless unless there is some way to harness it. This is the purpose of an antenna. Since the majority of research in this work is dedicated towards designing an antenna suitable for a wireless sensor platform, basic antenna theory and the applicable terms need to be understood by the reader. This section attempts to do this in as clear and as succinct a manner as possible.

The first term is the *radiation pattern* of the antenna. This is also an overarching topic, since many of the terms and metrics describing an antenna attempt to quantify the information contained in the radiation pattern. As its name suggests, a radiation pattern describes the radiation characteristics of an antenna. These characteristics are in the far-field of the antenna, inscribed upon an imaginary spherical surface. The far-field of an antenna is where TEM mode propagation is fully established, typically at a distance greater than  $2D^2/\lambda$  where  $D$  is the largest physical dimension of the antenna [11]. Typically, the pattern focuses on the field or power intensities of the antenna. The pattern often is given in a logarithmic scale versus linear, commonly using decibels (dB). The conversion from a linear to a decibel scale for field intensity is

$$|E_{dB}| = 20 \log_{10}(|E_{lin}|) \tag{2.10}$$

and the conversion for power intensity is

$$G_{dB} = 10 \log_{10}(G_{lin}). \tag{2.11}$$

The  $E$  in Equation 2.10 refers to electric field intensity. Any applicable field measurement can be substituted for  $E$ . The  $G$  in Equation 2.11 refers to gain, which will be covered further on in this section.

Typically, three principal plane cuts are given, or even a full 3D pattern. These plots describe the manner in which the antenna radiates. Some antennas, such as a dipole, radiate almost equally except along the poles or tips of the antenna. Figure 2.2a displays a typical dipole antenna and Figure 2.2b displays a radiation pattern typical for dipoles. A horn antenna, however, radiates well in only a small area, much like a spotlight. Figure 2.3a shows a horn antenna and Figure 2.3b displays a typical radiation pattern for a horn antenna. Determining which antenna to use depends on the intended application for the antenna. Just as a person uses a camera to take a picture of a broad landscape versus a telescope, an antenna must also be chosen with an appropriate radiation characteristic for the application.

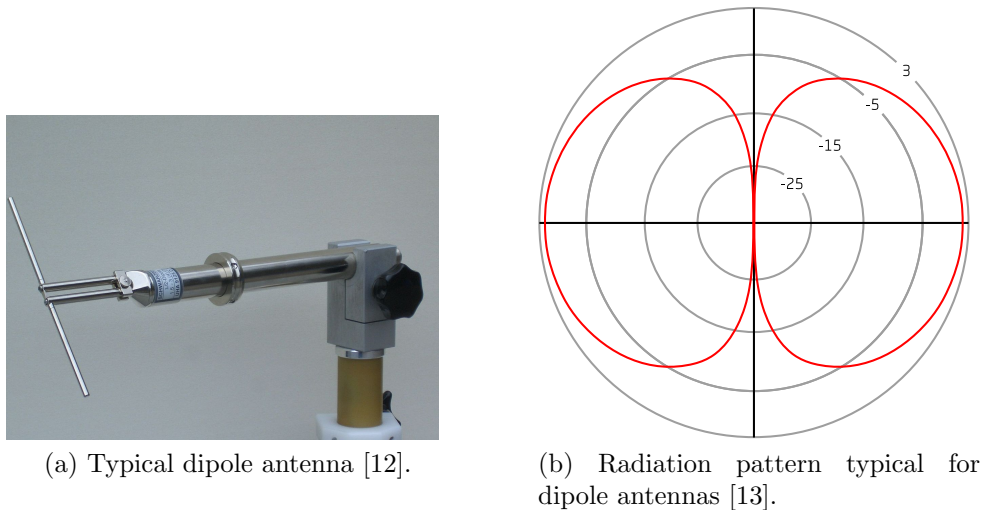
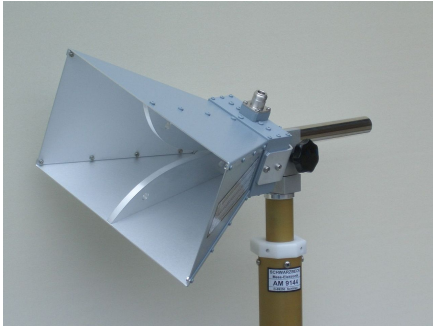
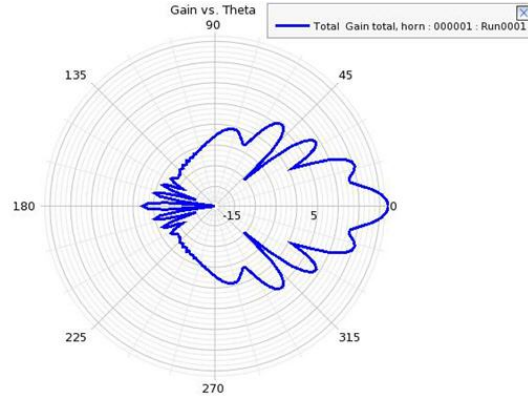


Figure 2.2. A typical dipole antenna and a radiation pattern typical of the antenna type.



(a) Typical horn antenna [14].



(b) Radiation pattern typical for horn antennas [15].

Figure 2.3. A typical horn antenna and a radiation pattern typical of the antenna type.

An important figure of merit describing a radiation pattern is *gain*. Gain, referenced by Equation 2.11, is typically what is plotted on a radiation pattern. Expressed in equation form, gain is defined in [11] as

$$Gain = 4\pi \frac{\text{radiation intensity}}{\text{total input (accepted) power}} = 4\pi \frac{U(\theta, \phi)}{P_{in}}. \quad (2.12)$$

Since radiation intensity,  $U(\theta, \phi)$ , is given at every point on the spherical radiation boundary of the antenna, gain is also able to be calculated at any point. The values of  $\theta$  and  $\phi$ , used as arguments in determining the radiation intensity, are defined by the spherical coordinate system. The relation of  $\theta$  and  $\phi$  to a typical three axes coordinate system is shown in Figure 2.4. In the figure,  $\theta$  is defined as the angle from the positive  $z$ -axis and  $\phi$  is defined as the angle from the positive  $x$ -axis. Another important item to note about Equation 2.12 is the use of the total input power in the denominator. This takes into account the efficiency of the antenna as a radiator as well.

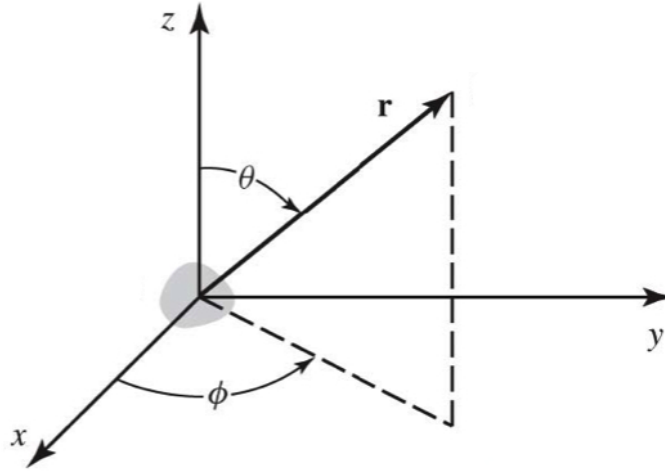


Figure 2.4. Spherical coordinate system [8].

While figures of merit are important in describing the operation of an antenna, knowing the distance of a wireless link possible with a certain antenna is crucial. With information regarding both the transmitting and receiving antennas in a wireless link, it is possible to determine the power received based upon the power transmitted. This is known as the *Friis Transmission Equation* and is given as

$$\frac{P_r}{P_t} = \left( \frac{\lambda}{4\pi R} \right)^2 G_{0t} G_{0r} \quad (2.13)$$

where  $P_r$  is the power received and  $P_t$  is the power transmitted [11]. The term  $\left( \frac{\lambda}{4\pi R} \right)^2$  is called the *free-space loss factor*. It represents the power lost because of the spherical spreading of the propagating wave. This is best thought of as dropping a pebble into water. As the pebble strikes the surface, the waves spread equally away in all directions and only a small portion strikes the observation point, a distance  $R$  away. However, the gain of the antenna influences this spreading. Instead of spreading in all directions, the higher the gain value of the antenna, the more directive the propagating wave. While it does not spread out as much, a wave from a high-gain

antenna will reach its target and deliver more power than a comparable wave from a low-gain antenna. The values  $G_{0t}$  and  $G_{0r}$  represent the gain of the transmitting and receiving antenna, respectively, assuming perfect orientation towards each other. A load impedance perfectly matching the antenna is also assumed.

As mentioned previously, orientation determines antenna performance. While a high-gain antenna does deliver more power to the receiving antenna, the antenna only has high gain in a small region of its radiation pattern. While a low-gain antenna will not deliver power as concentrated, it does so over a much larger extent of its radiation surface. This can be seen visually by contrasting the radiation patterns shown in Figures 2.2b and 2.3b. The choice between low-gain and high-gain antennas is based upon the distance of the wireless link, the power needed at the receiver, the spatial coverage required, and the orientation of the antennas. If orientation cannot be tightly controlled, a low-gain antenna must be used in order to ensure enough power reaches the other antenna in the wireless link.

While antenna design is a major factor in determining the performance of wireless communication, impedance matching plays an equally important role in determining the distance of a wireless link. This will be further explored in the next section.

### **2.3. Impedance Matching**

Much of the theory presented so far only focuses on antennas and wave propagation. However, an antenna is worthless without a source system either driving the antenna or receiving what the antenna is picking up. The manner in which the source and antenna are connected is not a trivial manner. From basic circuit theory, the output resistance of a circuit must match the resistance of the load connected in order for maximum power transfer to occur. The same is true for antennas with complex load impedances. The impedance of the antenna must be the complex conjugate

of the source impedance. This ensures not only maximum power transfer but that reflections between the two are also minimized. This is important since reflections can cause damage to transceivers, lower receiver sensitivity and increase amplitude and phase errors in power distribution networks [10].

Besides the impedance of the source and antenna, the characteristic impedance,  $Z_0$ , of the transmission line connecting both together must be considered. Typically, the source is chosen to match  $Z_0$ . The antenna is then matched to  $Z_0$  via an impedance matching network. The goal of the impedance matching network is to transform the impedance of the antenna to the complex conjugate of  $Z_0$ . The matching network must do this with minimal losses.

Many different types of matching networks exist. The simplest are those utilizing discrete components. While not an exhaustive list, components are typically configured as an *L-network*, a  *$\pi$ -network*, or a *T-network*. Figure 2.5 displays an example of each. The names of the different networks describe the layout, or configuration, of the circuit components. Almost always, the discrete components are reactive (capacitors and inductors) components only. If a resistive component was used, high losses would be incurred and the efficiency of the network would decrease greatly.

Besides discrete components, which are often plagued with large tolerances, there exist different types of matching networks using lengths of transmission line. While not as simple as discrete components, these matching networks do not suffer from large tolerances. Two typical matching network designs using lengths of transmission line are *stub matching* and *quarter-wave transformers*. These two designs are shown in Figure 2.6. A stub match uses either short-circuited or open-circuited stubs of transmission line in either series or parallel connection. Figure 2.6a displays a parallel stub match. Design variables are the length of the stub,  $\mathbf{L}$ , and the distance

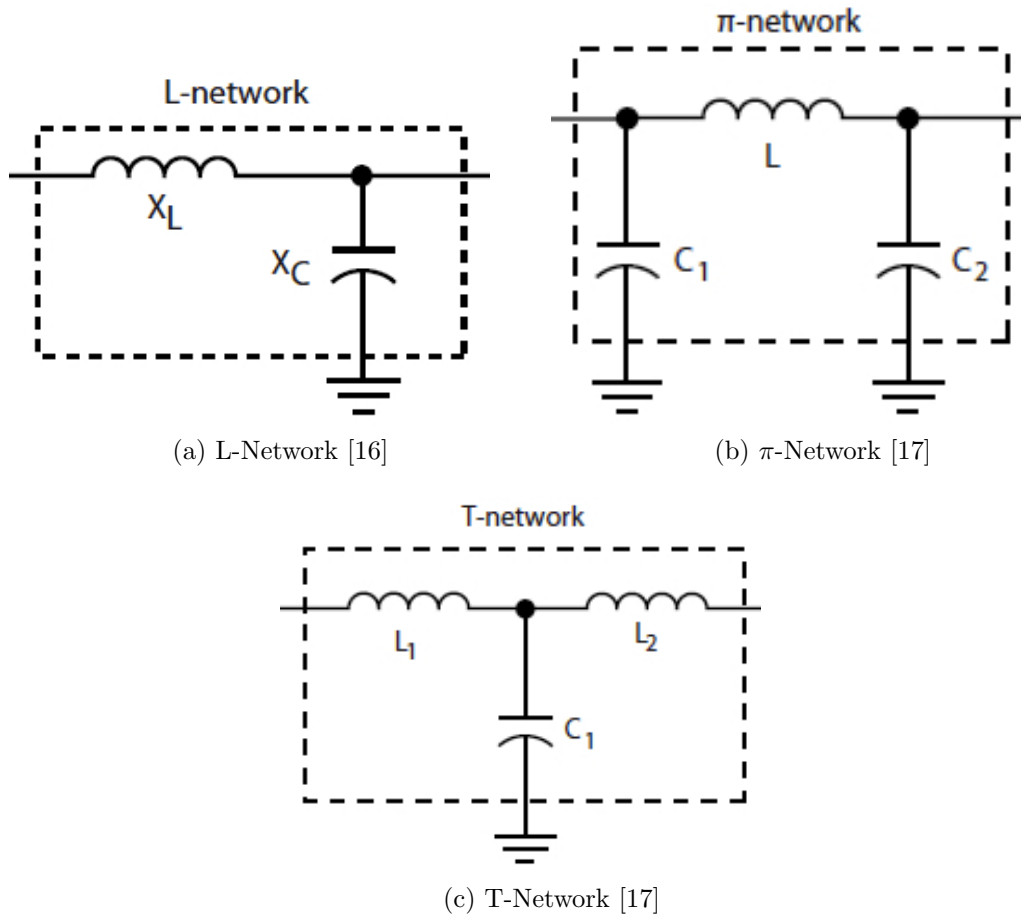
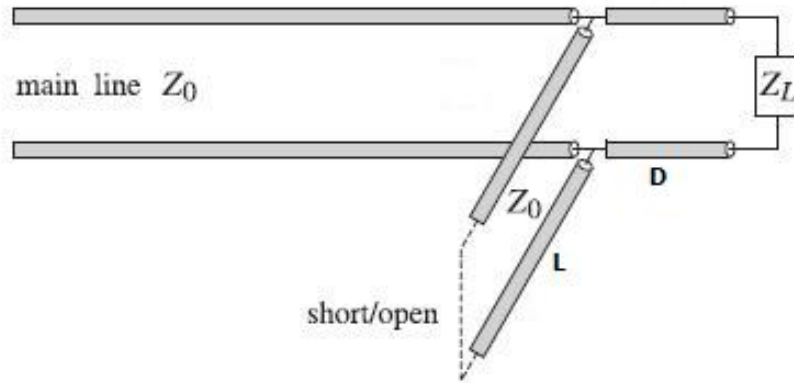


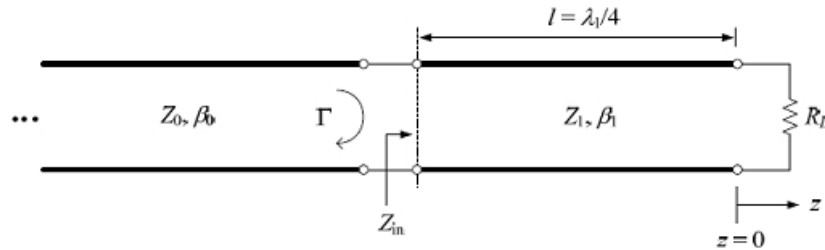
Figure 2.5. Typical matching circuits.

away from the antenna, **D**. A quarter-wave transformer, shown in Figure 2.6b, uses a quarter-wavelength long piece of transmission line connected in series with the antenna. The quarter-wavelength section has a characteristic impedance,  $Z_1$ , so that the impedance,  $Z_{in}$ , seen at the source-facing end of the matching network is the conjugate of  $Z_0$ . While both of these matching networks are low tolerance designs, they are difficult to manufacture and take up a significant amount of space on printed circuit boards at lower frequencies ( $< 10$  GHz). For higher frequencies, these types of matching networks are preferred because of the tolerances and parasitics of discrete

components. For design equations for these, discrete component matching networks, and additional matching techniques, see [10] and [11].



(a) Parallel Stub Match [18]



(b) Quarter-Wave Transformer [19]

Figure 2.6. Examples of a parallel stub match and a quarter-wave transformer.

As mentioned with stub matching networks, the placement of a load along a transmission line affects the impedance realized at the antenna (or source). This happens when the impedance added does not equal  $Z_0$ . This is because of the reflections induced on the line because of the impedance mismatch between  $Z_0$  and the added component. Concerning the reflection equations (Equations 2.8 and 2.9) mentioned in Section 2.1, these only reference the magnitude of the forward and



backward propagating waves. A more useful equation for the reflection coefficient for impedance matching is given in [10] as

$$\Gamma = \frac{Z_L - Z_0}{Z_L + Z_0}. \quad (2.14)$$

Equation 2.14 results in the reflection coefficient on a transmission line with characteristic impedance,  $Z_0$ , connected to a load impedance,  $Z_L$ . When  $Z_L$  equals  $Z_0$ ,  $\Gamma$  goes to zero and reflections do not exist on the transmission line. If reflections do exist, adding a matching network, such as a stub, the mismatched impedance of the load is combined with the mismatched impedance of the stub to create an equivalent impedance that is matched to  $Z_0$ . This is one circumstance where two wrongs do make a right! However, this is only true over a finite bandwidth, since impedance is frequency dependent [10]. This bandwidth where the matching network operates correctly is a metric to determine performance. It is typically defined where  $|\Gamma| \leq 0.1$ . Normalizing the bandwidth allows the metric to be compared with networks operating at different frequencies. This normalized bandwidth is known as the *fractional bandwidth*. It is defined as

$$fractional\ bandwidth = \frac{\Delta f}{f_0} \quad (2.15)$$

where  $\Delta f$  is the bandwidth and  $f_0$  is the center frequency or *operating frequency* [11]. While the center frequency is the frequency in the middle of the bandwidth, the operating frequency is the frequency in the bandwidth where the system is operating the most effectively (typically with respect to the reflection coefficient). Besides matching circuits, fractional bandwidth is also applicable to antenna performance over frequency.

In order to determine the distance needed from the antenna to place a stub or any other reactive component, an equation is needed which relates the position on the transmission line to the effective impedance realized. This is given in [10] as

$$Z_{in,eff} = \frac{Z_L + jZ_0 \tan \beta l}{Z_0 + jZ_L \tan \beta l} \quad (2.16)$$

where  $Z_L$  is the load impedance,  $\beta$  is as defined by Equation 2.6,  $Z_0$  is the characteristic impedance of the transmission line, and  $l$  is the distance between  $Z_L$  and the observation point along the transmission line where  $Z_{in,eff}$  is inferred. The transmission line is assumed to be lossless in this equation.

#### 2.4. RFID

Segueing from the rigor of wave propagation and antenna theory, this section will explain the basics of RFID. This includes the infrastructure in an RFID system, the basic function of the RFID protocol, and a brief explanation of the electrical systems involved. For a more rigorous overview of each subject, see the information provided in [2].

The infrastructure needed for an RFID system is simple. A complete system is comprised of a *reader (interrogator)*, an *antenna*, and a *tag*. The reader is a full radio transceiver. The reader is tasked with *querying*, or requesting information from all RFID tags within its range. The information that is received is then decoded by the reader and either displayed locally, if the reader is a complete system, or transferred to a connected computer. As mentioned in Section 1.2, RFID tags are typically fully passive devices, meaning they harvest the power needed to operate from the transmitter, the reader. This means the reader must contain amplifiers in order to provide enough transmit power to turn-on and operate the RFID tags. In addition to providing a large amount of power, they need to remain sensitive enough in order to detect the low-powered backscattered signal from the tags [2].

The antenna is an important part of the reader. It allows the reader to communicate with the RFID tags. Depending on the application, a reader can use many different types of antennas. The antennas used vary based on the gain, radiation pattern or polarization needed. One of the most common antenna designs in use is the patch antenna, used for UHF RFID [2]. More information about reader antennas can be found in [11].

The last piece in an RFID system is the tag. The tag is comprised of an antenna and an RFID IC. The antenna is usually planar and designed for the object on which it will be used. Typically the gain of the antenna is maximized while maintaining a near omni-directional radiation pattern. Because the object where the RFID tag is located is typically in an unknown orientation, it is important that the reader is still able to communicate with the tag. The antenna must also contain impedance matching circuitry to match to the impedance of the RFID IC [2]. For UHF RFID, one such method is the T-match, similar to a shunt, short-circuit stub. More information about the T-match and other matching techniques can be found in [20]. Usually, the matching circuit will avoid using discrete components for cost savings and size restrictions. The RFID IC typically contains power supply circuitry, a demodulator, a modulator, logic circuitry, and non-volatile memory. The demodulator decodes information sent from the reader and sends it to the logic circuitry. Typically consisting of a state machine, the logic circuitry then decides whether to write new data to the memory or send information from the memory to the reader. To communicate with the reader, the modulation circuitry is used to modulate information onto the backscattered radiation [2].

RFID tags come in three different types, *active*, *semi-passive* and *passive*. An active tag uses a battery for power and features a full radio transceiver. This allows the active tag to be read from a large distance, even those not in line-of-sight.

Additionally, the transceiver allows faster data rates to be achieved between the tag and reader. While giving the best performance of the three tag designs, the active tag is also the most expensive.

The semi-passive tag still uses a battery but only contains radio hardware similar to a passive tag. This radio hardware consists of a demodulator and some sort of modulator, typically a transistor switch. The demodulator feeds information from the reader into the logic circuitry of the RFID IC. Using this information, the IC then operates the modulation circuitry. This modulates the backscattered radiation, which allows the tag to communicate with the reader.

The passive tag, in comparison to the semi-passive tag, does not have a battery. The passive tag is powered by harvesting power received from the reader. Additional circuitry is needed in order to harvest this power. Typically, this requires a diode for rectification and a charge pump in order to supply the RFID IC with the correct voltage for operation. While the passive tag requires additional circuitry, it is still less expensive than a semi-passive tag. However, without a battery for power, a passive tag exhibits a shorter read range than both the semi-passive and active tags [2].

As with RFID tags, RFID itself has three different types: low frequency (LF), high frequency (HF) and ultra-high frequency (UHF). In the United States, these utilize spectrum near 125 kHz for LF, 13.56 MHz for HF and both 900 MHz and 2.4 GHz for UHF. Both LF and HF utilize inductive coupling for communication, therefore, tag antenna designs are typically loops with multiple turns. For the RFID wireless sensor in this work, only UHF RFID will be used, specifically near 900 MHz. This uses radiative coupling for communication, allowing for much greater read ranges.

In addition, many different RFID protocols exist. The most popular for UHF RFID, however, is the EPCglobal Class 1 Generation 2 (EPC Gen 2). The EPC

(electronic product code) Gen 2 protocol allows for reading and writing to the RFID IC memory, killing of the tag by the reader, schemes to eliminate interference, and methods that avoid communication collisions in environments where numerous tags exist. The EPC Gen 2 protocol also supports a number of different commands in order to select a tag in a multiple tag environment in order to get information from or modify the tag. One of the most important of these commands is the *query* command. The query is the first command that requires a response from the tag. Once the reader sends a query command, the reader continues to output a carrier wave in order to power the tag and for the tag to backscatter information [2]. The query command, while only one of many, is especially important for testing the performance of a tag [21]. For a more in-depth review of UHF RFID protocols, including EPC Gen 2, see the information in [2].

The theory presented in this chapter is only a fraction of what is needed to fully understand antennas, wave propagation, RFID infrastructure and the RFID protocol. While understanding the theory and equations presented here will help in understanding the research presented in this work, many other resources are available. For a more comprehensive and complete overview of theory, see [2], [8], [9], [10], and [11]. While this is not an all-encompassing list, the information provided will help fill most holes the reader may have in the background theory.

## CHAPTER 3. PREVIOUS WORK

Research and development of wireless sensors is currently an important aspect in industry and defense-related fields. The ability to monitor certain parameters in an area, structure or device for an extended period is the primary use for wireless sensors. Since energy efficiency is paramount for most wireless devices, the use of a low-power communications protocol such as RFID can be extremely advantageous. Besides energy efficiency, the antenna design and resulting radiation pattern dictates the use and deployment of the wireless sensor. While offering greater read ranges in some orientations, a directional antenna limits the deployment methods. If the sensor is in the wrong orientation, such that a null in the radiation pattern is facing the measurement antenna, the sensor will perform poorly. A near-isotropic radiation pattern eliminates the orientation constraint at the cost of read range.

This chapter summarizes previous research completed on different types of wireless sensors and applicable antenna designs. These works are separated into two distinct sections: one for different wireless sensor designs and one for antenna designs exhibiting near-isotropic radiation patterns.

### 3.1. Wireless Sensor Designs

The wireless sensor designs presented here represent only a fraction of the previous research completed on the subject. While there exist many different designs and methodologies to accomplish wireless sensing, one attribute is shared among many designs: RFID. RFID allows a wireless sensor to communicate with low power requirements from the sensor itself to none at all. In fact, some wireless sensor designs simply modify the structure of common RFID tags in order to sense environmental parameters, relying on the reader to analyze and determine the current conditions experienced by the sensor. Just as RFID tags utilize three different power sources (active, semi-passive, passive) so do most wireless sensors.

The first of such wireless sensor power sources is the fully active design. In this design, a battery provides all of the power to the sensor. This gives an active sensor long read range, even when obstructed by other objects [2]. Additionally, the active sensor contains a full radio transceiver. This allows the active sensor to communicate with better modulation schemes, enabling higher data rates [2]. While these benefits are necessary for some sensor applications, the cost for an active sensor is prohibitive. Additionally, the increased complexity of the design and limited life of the sensor (dictated by battery life) makes this the least popular wireless sensor design.

One such use for an active, RFID based sensor is for location tracking. The design in [22] utilizes active RFID tags for the objects being tracked as well as a reference matrix of tags. The location of these reference tags is already known and each tag has its own unique identification code. Depending on the reference tags near the sensor being tracked, the location is then derived from these reference points. Because other objects or people may shield the sensors from the reader, the authors of [22] found it necessary to utilize the longer range active sensor design. The location algorithm created in [23] also is compatible with active RFID tags for location tracking.

The second type of RFID wireless sensors are those utilizing a semi-passive design. While the sensor does contain an energy storage device, such as a battery or super-capacitor, the semi-passive sensor does not have a radio transceiver. This allows the sensor to achieve much greater range than a passive design, but not as great a range or high a data-rate as active sensors. Using the energy storage device, the sensor is able to run onboard electronics that may exceed the power available during interrogation by the reader. In addition, the sensor is able to take measurements while not being interrogated. The sensor then stores this information and then sends it to the reader during interrogation. While this design is significantly cheaper than

an active design, it is still more expensive than a passive design. Also, if it uses a non-rechargeable battery, the sensor has a finite lifetime. If, however, the sensor uses a super-capacitor, it can be recharged during interrogation, eliminating the lifetime due to battery life constraints.

With the advantages listed above, the semi-passive design is understandably more popular currently than the active design for wireless sensors. The Intel WISP, mentioned previously in Section 1.3, is a good example of this design. In [4], the authors overview the sensor and stress the importance of the onboard super-capacitor. The authors explain how the super-capacitor allows the sensor to take measurements while not being interrogated and then simultaneously sends data and recharges during interrogation. They then state how important this functionality is when monitoring temperature over time. Additional uses for this sensor are given in [24] and [25]. Some of these uses are in the medical field and in behavioral tracking. There are also other designs detailed in literature besides the Intel WISP. Instead of using a super-capacitor, the design in [26] uses a battery. While this isn't rechargeable, it offers a more cost effective option. This sensor design is used for tracking the temperature in food as it is shipped.

The last RFID wireless sensor type is the passive design. This design does not have any energy storage device and operates only off the power available during interrogation. No energy storage device means there is no way to continuously log data when the sensor is not being interrogated. While this is a disadvantage for the passive design, it also means the sensor is inexpensive and typically simpler to manufacture. Additionally, the sensor is not limited by the lifetime of a battery.

Several designs currently exist in literature utilizing a passive sensor for several different applications. The first of these applications is temperature monitoring. While a passive design cannot monitor the temperature while not being interrogated,



it is possible to record a temperature threshold violation or the temperature of the sensor during interrogation. Temperature thresholds are important in both the food industry and the medical industry. The first design is the sensor in [27]. The sensor uses two RFID tags placed near each other. A shape memory polymer, which responds to temperature, holds a piece of metal behind one RFID tag, detuning it so it is not read by the reader. If the temperature threshold is exceeded, the shape memory polymer moves the metal to the other tag permanently. A threshold violation is then determined by the reader depending on which RFID tag is able to be read. The sensor design presented in [28] is similar to the design in [27]. The sensor in [28] uses a Nitinol wire shorted across one RFID IC in a two RFID IC sensor design. If the temperature threshold is exceeded, the Nitinol wire short breaks, allowing both RFID ICs to be read during interrogation. If both RFID ICs can be read, this means the sensor experienced a temperature above the set threshold. The sensor in [29] uses a different method, instead utilizing only a single RFID tag for current temperature sensing. The sensor uses a temperature sensitive material underneath the antenna. When the temperature changes, the material alters the antenna and changes the frequency response of the antenna. This results in a frequency based measurement, where the shift in the operating frequency of the tag correlates to the current temperature.

A second application for a passive sensor is in structural health monitoring. Roads, bridges and buildings experience extreme loads and stresses. By being able to monitor these, critical failures can be preempted by timely and appropriate maintenance. Passive sensors allow an inexpensive method for this needed monitoring. The sensor in [30] utilizes two separate RFID tags to measure internal loading. The design dedicates one tag for harvesting power for the sensing circuitry while the other tag is for typical RFID communication and transmitting the current load data to the measurement device. The sensor in [31] utilizes deformation of the antenna as in [29]

except it is used for strain measurements. As the antenna is deformed, this changes the backscattered power. By measuring backscattered power from the tag, the sensor in [31] is able to determine the strain in a structure. The sensor in [32] measures the strain or deformation in a structure by analyzing the frequency response of the RFID tag. Again this is similar to the method presented in [29]. As the strain on the structure increases, the operating frequency of the RFID tag shifts downward. This is measured and correlated to strain by the reader. Lastly, the sensor in [33] measures the deflection of a structure by measuring the backscattered power from an RFID tag. As the structure deflects, it displaces a metal plate closer to the RFID tag. This loads the antenna and then alters its performance.

While temperature and structural health monitoring are popular areas for wireless sensors, other applications of equal importance exist. The sensor in [34] measures the presence of ammonia. The dielectric used as a support for the antenna is based on carbon nanotubes. In the presence of ammonia, the electrical characteristics of the dielectric are altered, reducing the required turn-on power for the RFID tag. When the ammonia dissipates, the dielectric gradually returns to its normal state. In [35], the authors summarize a design which uses MEMS (microelectromechanical systems) in order to measure multiple environmental parameters, such as pH, relative humidity, and CO<sub>2</sub> concentration. A specialized RFID IC, when interrogated, reports these parameters back to the reader. A sensor design outlined in [5] uses two RFID ICs and a mercury switch to create a simple one bit accelerometer. If the object is under positive acceleration, one RFID IC can be read by the reader. If the object is instead under negative acceleration, only the other RFID IC can be read.

Each RFID wireless sensor design exhibits compelling advantages for the eventual design in this work. However, an active design is too expensive for the goal of a high-density wireless sensor network. In addition, while the passive designs are

inexpensive and can measure a variety of environmental parameters, they remain unproven. Furthermore, the passive designs that rely on frequency sweeps violate the rules placed on the RFID protocol. When reading an RFID tag, a reader must randomly adjust its read frequency; it cannot sweep the entire RFID frequency band [2]. Therefore, the wireless sensor platform that will be presented in this work focuses on a semi-passive RFID design. The platform will need to make accommodations for additional sensor electronics as well as an energy storage device.

The antenna serves as the foundation for any wireless sensor design. The antenna is therefore the focus of the research performed in this work. The next section details previous antenna designs found in literature.

### **3.2. Previous Antenna Designs for Wireless Sensors**

For any wireless system, the antenna is a critical aspect. As mentioned in the beginning of Chapter 3, several design aspects must be considered. These include the frequency of operation, bandwidth, radiation pattern, physical size, and gain. For a wireless sensor utilizing a semi-passive design, the antenna design needs to contain space for the sensor electronics as well as an energy storage device. Additionally, the design needs to take into account how these electronics will affect the performance of the antenna. If the wireless sensor is going to have an uncontrolled orientation when deployed, the radiation pattern needs to be near-isotropic. The following antenna designs are those found in previous literature that most closely match these requirements.

The first design is a cube shaped antenna found in [36]. The antenna itself consists of two elements. The first is a folded dipole where the feed is located. The second is a duplicate folded dipole with the feed shorted. This second element acts as a parasitic element. The parasitic element produces a more isotropic radiation pattern. The authors manufactured the antenna using photolithography on LCP (liquid crystal

polymer) substrate. The design was then folded onto a cube of Styrofoam. In total, the cube had a side length of 30 mm, which results in a diagonal length of 42 mm. This equates to an electrical length of  $0.128 \lambda$  for the diagonal length at 915 MHz. The antenna exhibits 13 MHz of bandwidth or 1.4% fractional bandwidth at 915 MHz. The maximum gain for the antenna is 0.53 dBi.

The design in [37] is another cube shaped antenna that operates at 2.4 GHz. The antenna is a meandered dipole antenna constructed on a substrate with a relative permittivity ( $\epsilon_r$ ) of 10.2. The substrate and antenna are then folded into thirds to create a cube. The resultant cube has a diagonal of 22 mm, or  $0.176 \lambda$  at 2.4 GHz. The design exhibits a bandwidth of 48 MHz or a 2% fractional bandwidth at 2.4 GHz. The antenna exhibits a maximum gain of 1.69 dBi.

The design presented in [38] is able to be used on a cube shaped sensor platform as well. The antenna has two legs, which are bent over the corner of the cube. Bending the legs over the corner of the cube gives the antenna a near-isotropic radiation pattern. The cube itself has a diagonal length of at least 65 mm, and is made out of paper. This equates to an electrical length of  $0.188 \lambda$  at 865 MHz. The antenna is designed to operate at 865 MHz versus 915 MHz since it is designed for the European UHF RFID frequency band. It exhibits 3 MHz of bandwidth or 0.35% fractional bandwidth at 867.5 MHz, its operating frequency.

The design of the antenna in [39] is similar to the design in [38]. The antenna is a two-legged design targeted for use on luggage. The antenna is meant to reside on the corner of a piece of luggage, giving it a near-isotropic radiation pattern. The bandwidth for the design is unknown but it is a cube with a diagonal near 100 mm, or  $0.289 \lambda$  at 865 MHz. Bandwidth and gain performance were not given for this design.

The antenna design in [40] is a spherical design. The antenna is a dipole, meandered around the surface of the sphere to give it a near-isotropic radiation pattern. The sphere itself is made of Styrofoam and has a diameter of 25 mm, or  $0.076 \lambda$  at 911 MHz, the center of the Korean UHF RFID band. The antenna exhibits a bandwidth of 7 MHz, or 0.77% fractional bandwidth at 911 MHz, its operating frequency. It exhibits a maximum gain of 0.75 dBi. The work in [41] states that this spherical antenna design is meant for use in intravenous (IV) bags in order to improve management of supplies in a hospital.

The antenna designs overviewed all use a 3D design in order to achieve a near-isotropic pattern. A summary of relevant information for all of the reviewed designs is given in Table 3.1. An advantage of a 3D design is that the sensor electronics can utilize the internal volume. However, none of the previous designs accounted for internal electronics or printed circuit boards (PCBs) in simulation or the resulting prototypes. Furthermore, none of the designs presented a feasible method for internal electronics to feed the antenna. These antenna designs also exhibited properties that will significantly impact sensor performance such as low bandwidth and non-optimal radiation patterns. The designs were constructed of non-robust materials such as Styrofoam or cardboard, which will fare poorly in the conditions likely encountered by a wireless sensor.

Table 3.1. Comparison of previous antenna designs.

<b>Antenna</b>	<b>Size (<math>\lambda</math>)</b>	<b><math>f_0</math> (MHz)</b>	<b>Fractional BW (%)</b>	<b>Max Gain (dBi)</b>
[36]	0.128	915	1.4	0.53
[37]	0.176	2400	2	1.69
[38]	0.188	865	0.35	–
[39]	0.289	865	–	–
[40]	0.076	911	0.77	0.75

Therefore, the research presented in this work results in an antenna optimized for use as a wireless sensor. The effect of adding a circuit board and sensor electronics is explored. The antenna is optimized for sensor use, where the orientation will be uncontrolled. The design features a near-isotropic radiation pattern and utilizes a rugged material in order to survive long-term in the conditions likely to be encountered by a wireless sensor.

## CHAPTER 4. SIMULATION SETUP AND VALIDATION

### 4.1. Model Setup

The antenna design presented in [40] served as a starting point for this work. The antenna in [40] is a spherical antenna with a radius of 12.5 mm. It is shown in Figure 4.1. A spherical antenna design is optimal since it does not have a preferred physical orientation, assuming equal volumetric mass distribution, and it offers the best use of the physical volume of the antenna [42]. This is especially important since size is a critical design criterion for wireless sensors. For instance, if the sensors are deployed using an aircraft with limited cargo space, such as a UAV, using smaller sensors means more sensors can be deployed during a single flight.

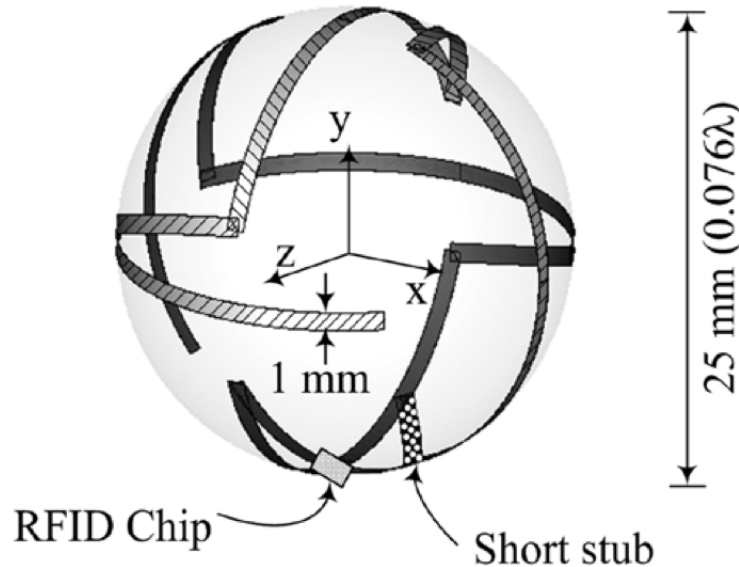


Figure 4.1. The antenna design presented in [40].

Before a prototype antenna is built however, it must first be simulated and optimized for use with a wireless sensor. Since the antenna will be spherical in shape,

a planar-based simulation package will not be suitable for the design. Instead, a full-wave 3D solver must be used. For this work, HFSS (high frequency structure simulator) by ANSYS will be used [43]. HFSS is a full-wave 3D solver utilizing the Finite-Element method in order to solve the partial differential equations associated with wave propagation. For more information on how the Finite-Element method solves electromagnetic problems, see [44].

As with any simulation package, the results are only as accurate as the model used. In order to test the accuracy of the general model for a spherical antenna structure, the antenna design in [40] was simulated in HFSS. By comparing the results of the simulation to those given in the paper, the general simulation setup and model used for further research would be validated.

For the HFSS model of the design in [40], a Styrofoam ball was first added with a radius of 12.5 mm. In HFSS, Styrofoam is assigned a relative permittivity ( $\epsilon_r$ ) of 1.06. The antenna structure was then added following the design outline in [40]. The antenna traces were defined as copper with a conductivity of  $5.8 \times 10^7$  siemens/m. The traces were 1 mm wide as specified in [40] and shown in Figure 4.1. The thickness of the copper used was not specified in [40]. A thickness of 150  $\mu\text{m}$  was assumed, based on the thickness of some types of copper tape. The size of the port used was also not specified. A port size matching the width of the conductor and a length of 2 mm was assumed. The port type used in HFSS was a lumped port with the results normalized to the port impedance of 50  $\Omega$ . The antenna was simulated in air versus a vacuum in order to more closely match the conditions encountered in measuring a prototype antenna. The air box surrounding the antenna was at a minimum of one half of a wavelength ( $\lambda$ ) away from the antenna at the lowest simulation frequency. The model used in HFSS for the antenna in [40] is shown in Figure 4.2.



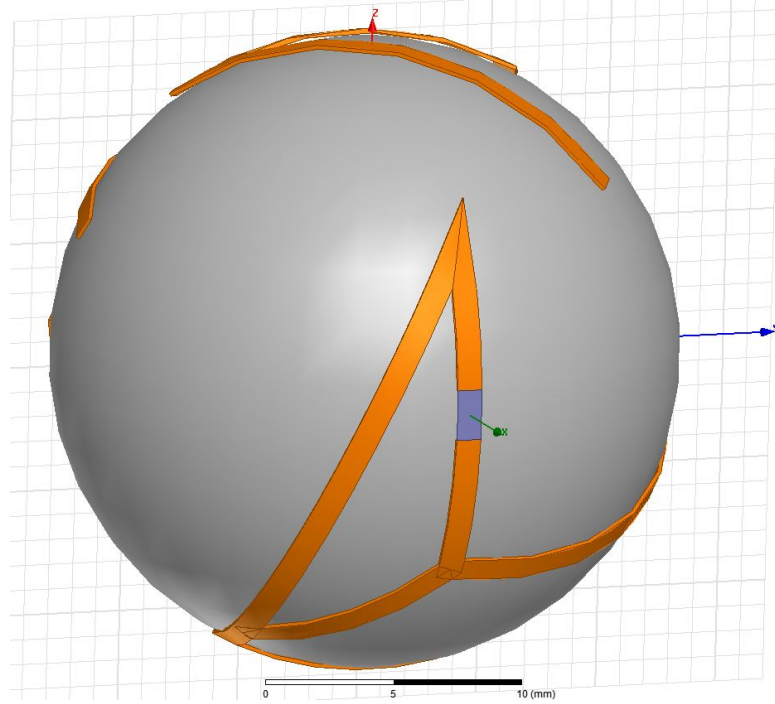


Figure 4.2. The antenna design presented in [40] as modeled in HFSS.

The Finite-Element method is a numerical method for solving difficult and complex partial differential equations. This means the solution is not an exact solution. An approximation is made depending on the model resolution. HFSS breaks down the model into a number of tetrahedrons and solves a set of equations taking into account the boundary conditions present between each tetrahedron as well as the partial differential equations describing wave propagation. The size of these tetrahedrons determines the accuracy of the model. HFSS uses an adaptive meshing method, where the size of the tetrahedron are decreased until the deviation in results between subsequent simulation runs is smaller than the amount specified by the user. For this and subsequent simulations in this work, this deviation is specified as 0.5 % for two consecutive runs, where the mesh density is increased after every run.

## 4.2. Simulation Results

As mentioned previously, the port impedance used by HFSS was specified as  $50 \Omega$ . This refers to the load seen by the antenna. The results given will be in reference to this  $50 \Omega$  load. However, as outlined in Section 2.3, the antenna impedance needs to be the conjugate of the load connected to it. The load in [40] is a UHF RFID IC with an impedance of  $14-j145 \Omega$ , not the  $50 \Omega$  of the specified port. Therefore, this impedance difference must first be accounted for in order to obtain valid data. While the impedance of the antenna reported by HFSS will be correct, the *return loss* data, as shown in [40], needs to be corrected from HFSS. Using Equation 2.14 with  $Z_0$  equal to the antenna impedance obtained by HFSS and  $Z_L$  equal to the impedance of the RFID IC,  $14-j145 \Omega$ , the correct reflection coefficient is obtained. The method of defining  $Z_L$ , however, is not entirely correct. Typically, the impedance of an RFID IC is given as an equivalent circuit model, such as the parallel RC circuit given in [45]. This means the impedance of the RFID IC is not constant but rather dependent on frequency. While this will skew the results, the points of interest near the 911 MHz operating frequency of the antenna in [40], will exhibit little error since the impedance given,  $14-j145 \Omega$ , is defined at 911 MHz.

With the reflection coefficient for the design used in [40] found, return loss can be calculated. Return loss is defined as

$$\text{Return Loss (dB)} = -20 \log_{10} |\Gamma|. \quad (4.1)$$

An item of importance regarding Equation 4.1 is the negative sign. Ignoring the negative sign is a common error found in literature [46]. When return loss is plotted in decibels, it should always be positive. Ignoring the negative sign results in a decibel plot of return loss that is always negative, versus always positive. This mistake was made in Figure 2a labeled “return loss” in [40]. In order to accurately compare

the simulation results from HFSS to the results in [40], *negative return loss* will be presented.

The results for the antenna presented by the authors in [40] are shown in Figure 4.3. From [40], the simulated results indicated an operating frequency of 912 MHz with a negative return loss of -15.9 dB. The measured results exhibited an operating frequency of 911.25 MHz with a negative return loss of -34.8 dB. The plot shown in Figure 4.4 gives the results for the antenna simulated in HFSS (shown in Figure 4.2). While the magnitude of the return loss between the results presented here and those in [40] deviate by about 11 dB, the operating frequencies match. Two possible sources of error in the HFSS simulation are incorrect copper trace thickness and incorrect port size.

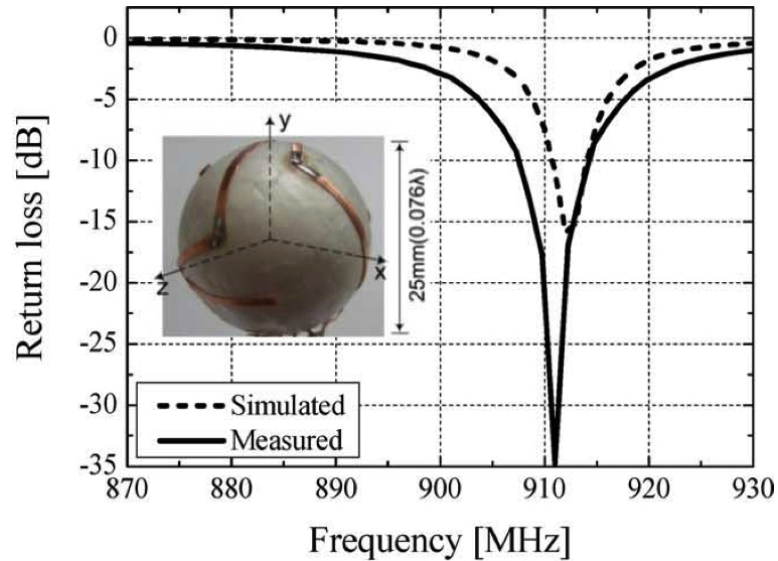


Figure 4.3. Negative return loss plot for the antenna design, as shown in Figure 2a of [40].

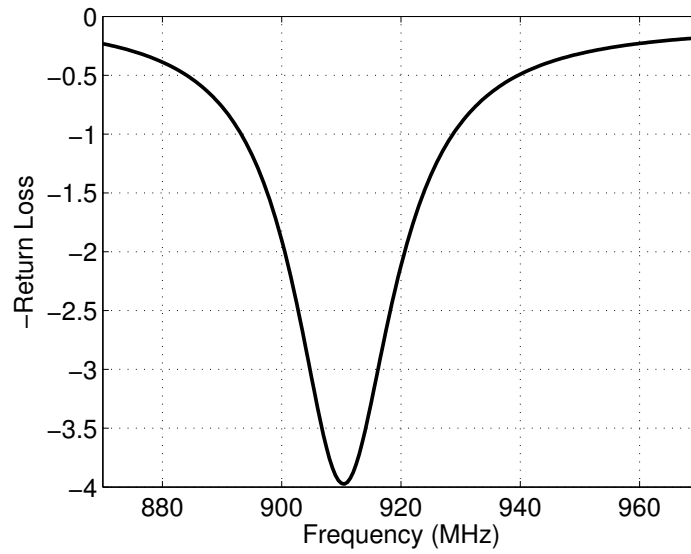


Figure 4.4. Negative return loss plot for the antenna design in [40], simulated in HFSS and shown modeled in Figure 4.2.

By further modifying the antenna design modeled in HFSS, better correlated results may have been obtained. However, the overall simulation accuracy was proven by the operating frequency matching between the two simulations. This validates the setup method for simulating antenna designs in future research. The results obtained from future simulations can now be trusted in predicting the performance of the eventual prototyped antenna design.

## CHAPTER 5. ANTENNA DESIGN AND SIMULATION

With the results from Section 4.2 validating the simulation setup used in HFSS, work designing a new wireless sensor antenna can begin. Before starting on a new design though, certain design goals need to be established. The first of these is the physical size of the wireless sensor platform. The sensor needs to be big enough in order to fit the necessary electronics and exhibit good efficiency as a radiator. However, the antenna needs to be small enough in order to allow for the deployment of a high-density sensor network. The radiation characteristics of the antenna also need to be addressed. These include the radiation pattern necessary and the gain of the antenna. Lastly, the sensor electronics and their platform need to be included in the simulation in order to determine their effects on the performance of the antenna. As outlined in Section 3.2, antenna designs previously presented did not account for the effects of added sensor electronics. For a wireless sensor design, it is critical these effects be taken into account.

### 5.1. Design Goals

As outlined in the introduction for this chapter, the antenna design resulting from this work needs to meet certain goals. These goals ensure the antenna will create a viable wireless sensor platform. Section 1.4 provides an explanation for these goals. The first is that the antenna needs to be small and inexpensive. The second is that the antenna must be a near-isotropic radiator. The third is that the antenna must operate in and span the UHF RFID spectrum for the United States. The fourth is that the antenna must integrate successfully with sensor electronics. The fifth and last goal is that the antenna must be rugged enough to survive its deployment and long-term exposure to the elements.

As stated in Section 4.1, the antenna design presented in [40] served as a starting point for the antenna design in this work. In [42], the author stated that a spherical

shaped antenna offers the best use of the physical volume of the antenna. This means that the total volume of the antenna is minimized while maintaining acceptable radiation performance. However, a small antenna results in reduced performance, caused by a smaller effective aperture. This leads to less gain, less radiation efficiency, higher impedance mismatch, and a high quality factor ( $Q$ ). Because bandwidth is inversely related to  $Q$ , this results in a narrow operating bandwidth. The high  $Q$  and reduced performance overall results from the antenna being electrically small [42]. From [42], an antenna is electrically small when  $ka \leq 0.5$  where  $k$  is the wave number in free-space given by  $2\pi/\lambda$  and  $a$  is the maximum radius of the antenna volume. For the antenna in this work, the radius is derived from a value where  $ka = 0.5$  based on the recommendation given in [47], putting the size of the antenna on the threshold of being electrically small. This resulted in  $a = 26.05$  mm for a free-space  $\lambda$  (wavelength) at 915 MHz. This small size partially fulfills the first goal in Section 5.1.

While the antenna design used in [40] and shown in Figure 4.1 did display near-isotropic radiation patterns, the design is not suitable for a wireless sensor. For a wireless sensor, the feed port needs to be accessible by the sensor electronics inside the sphere. The feed for the antenna in [40] is on the outside. In contrast, a dipole will allow the feed to be in the center of the sphere. Therefore, an antenna design derived from a dipole will be more suitable for a wireless sensor in regards to sensor electronics integration.

In addition to size and feeding, the other design goals must influence the design of the antenna. The bandwidth must be sufficient to cover the frequency band of interest. For the UHF RFID spectrum in the United States, this is 26 MHz for a fractional bandwidth of 2.8 % [2]. A dipole exhibits sufficient bandwidth to cover this frequency band. The bandwidth of a cylindrical dipole typically varies between a fractional bandwidth of 3 % to 30 %, depending on the cylinder length to diameter

ratio [11]. Therefore, an antenna derived from a dipole design should exhibit the necessary bandwidth. However, in order to create a wireless sensor which is not affected by orientation, the radiation pattern needs to be near-isotropic as mandated by the second design goal. A dipole does not provide this characteristic. A modified dipole antenna design will need to be explored in order to exhibit this characteristic.

Lastly, the overall antenna design must be rugged and simple to manufacture. The sensor will likely be exposed to an outdoor environment and must survive long-term. The sensor electronics will need to be protected from the environment. In addition, the antenna design must survive deployment, which may include a large fall if deployed from a UAV. Manufacturability is also important since the sensor must be reliably prototyped. A simple to manufacture sensor utilizing inexpensive electronics will allow for high-density sensor network deployments.

## 5.2. Initial Spherical-Cap Single Dipole Design

For a dipole to operate at a specified frequency, it needs to be near a half-wavelength in length [11]. At 915 MHz, a half-wavelength is greater than 160 mm in free-space. This is much greater than the 52.1 mm diameter sphere resulting from the calculations in Section 5.1. If left unmodified, the dipole will not operate at 915 MHz at the specified length of 52.1 mm. A short dipole with end caps, however, offers a solution. The end caps add shunt capacitance to the antenna. This emulates a longer antenna; however, it will exhibit electrically small effects. In [48], Wheeler stated that a spherical-cap best utilized the volume available in a spherical antenna. Following the suggestions given in [47] for spherical-cap dipole antennas, a single dipole antenna with caps was first designed with a maximum volume diameter  $d$ , as shown in Figure 5.1, of 52.1 mm. The dimensions shown in Figure 5.1 will be referred to in the current and future design iterations throughout this work.

The antenna was built around a 1mm thick shell of acrylonitrile butadiene styrene (ABS) plastic. The ABS antenna shell was assumed to have a relative permittivity ( $\epsilon_r$ ) of 2.8 and a loss tangent ( $\tan \delta$ ) of 0.01. The caps were modeled assuming construction with copper tape, which has a thickness of 100  $\mu\text{m}$ . The wires connecting the caps to the center of the spherical volume were modeled after 28 American wire gauge (AWG) wire, with a diameter, as indicated by  $w$ , of 0.321 mm. The single dipole antenna as modeled in HFSS is shown in Figure 5.2.

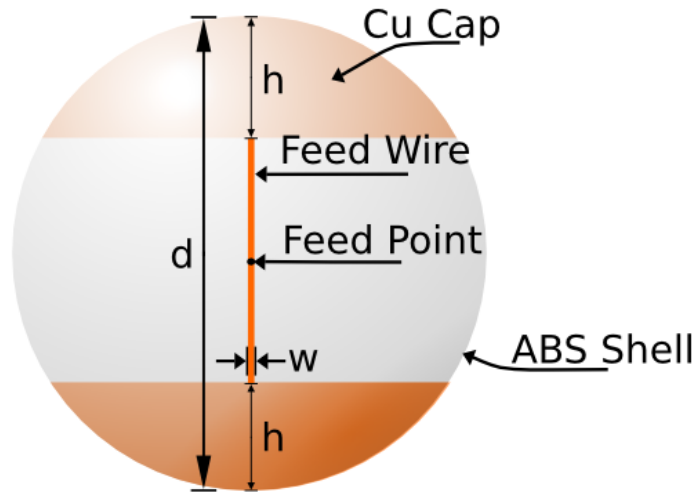


Figure 5.1. Drawing of the single dipole, spherical-cap design. The Feed Wire connects to the inside, center of the spherical-cap.

The ABS shell shown modeled in Figure 5.2 differentiates the design in this work with the previous antenna designs reviewed in Section 3.2. The ABS shell gives the antenna structural rigidity as well as the ability to protect the inner volume from the external environment. This allows the design to meet the durability goal set in Section 5.1. The shell is included in the simulation model in order to determine the effects of the shell on the performance of the antenna.



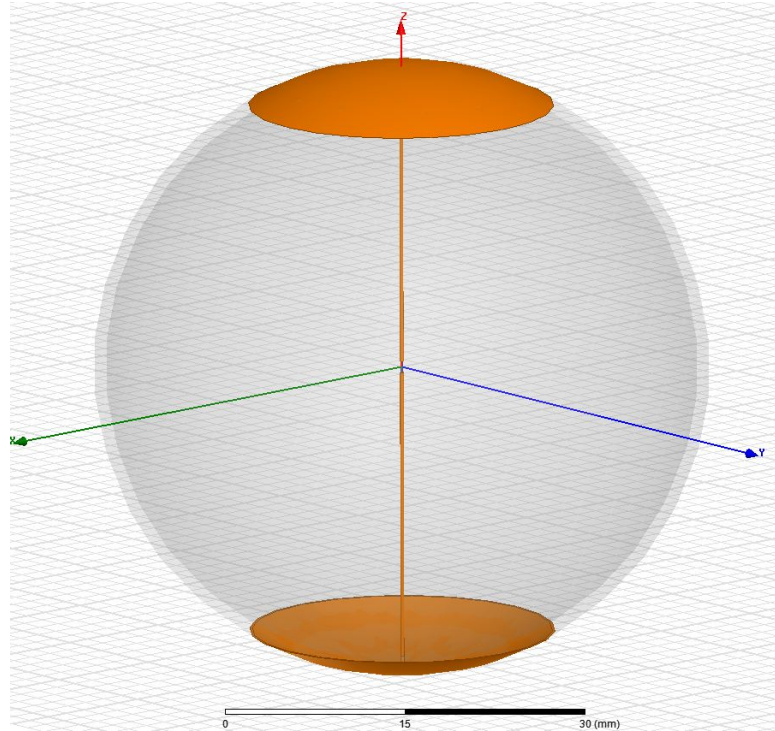


Figure 5.2. HFSS model of the spherical-cap, single dipole antenna with a 1 mm thick ABS shell.

In designing the antenna, the test method must be taken into consideration. As mentioned in Section 2.3, the antenna input impedance must be the complex conjugate of the source impedance driving it. While most test equipment has an impedance of  $50 \Omega$ , this method of testing an electrically small antenna is difficult and disruptive. Test equipment typically requires a direct connection to the antenna using a metal, shielded coax cable. The cable tends to distort the radiation pattern and overall performance of an electrically small antenna. Instead, a relative method for testing an electrically small antenna avoids this disruption. Using an RFID reader and combining the antenna with a UHF RFID IC, a relative radiation pattern can be obtained by analyzing the difference in turn-on power needed as the antenna is swept through different orientation angles, with respect to the reader antenna. While

this means absolute numbers cannot be directly compared between simulated and measured results, normalizing the data allows a relative comparison to be made.

In order to use this relative method of testing, the antenna must be matched to the chosen RFID IC. For the antenna design resulting from this research, the Alien Higgs 3, a UHF RFID IC, was chosen for testing. It has a parallel RC circuit equivalent of a 1500  $\Omega$  parallel resistance and a 0.85 pF parallel capacitance [45]. This gives the Higgs 3 an impedance of 27-j200  $\Omega$  at 915 MHz. For an impedance match, the antenna design needs a radiative resistance near 27  $\Omega$  and an inductive reactance of +j200  $\Omega$  at 915 MHz. In [40] and shown in Section 4.2, return loss was used as a metric for the impedance match between the IC and antenna. However, [49] gives a better metric. This metric, known as the *power reflection coefficient* (PRC), is given in [49] as

$$|s|^2 = \left| \frac{Z_L - Z_S^*}{Z_L + Z_S} \right|^2. \quad (5.1)$$

Equation 5.1 is similar to Equation 2.14, with  $Z_L$  representing the load impedance, and  $Z_S$  representing the source impedance. The range for PRC is  $0 < |s|^2 \leq 1$ . The load can be either the antenna impedance or the UHF RFID IC impedance. The range of frequencies where return loss is greater than or equal to 10 dB is considered the operating bandwidth of the antenna. An equivalent value for PRC is less than or equal to 0.1 [10]. The *operating frequency*, defined in Section 2.3, is best redefined here with respect to PRC. When referred to, the operating frequency is the point in the bandwidth of the antenna where the PRC is minimum.

The first iteration of the single dipole antenna, shown in Figure 5.2, has a hat height  $h$  equal to 6 mm. Viewing the PRC plot shown in Figure 5.3a, this iteration exhibited an operating frequency of 1.05 GHz with a bandwidth of 36.2 MHz. Since 1.05 GHz is greater than the 915 MHz spectrum center for RFID, changes needed to be made to the single dipole design. A simple way to do this is to increase

the shunt capacitance. This is accomplished by increasing the size of the spherical-caps. The impedance of the antenna at 1.05 GHz is  $20.1+j177.3 \Omega$  (see Figure 5.3b). By increasing the size of the spherical-cap, the negative reactance inherent to an electrically small antenna is reduced. However, this also has the effect of reducing the radiation resistance, leading to a higher Q [42], [47]. Consequently, a higher Q results in poorer performance in terms of bandwidth. By increasing  $h$  to 15 mm, the single dipole antenna was made to operate at 910 MHz. However, the value of the PRC at 910 MHz was 0.3, as shown in Figure 5.3a. The reason for this reduced performance results because of the changes in the impedance of the antenna. The impedance of the antenna at 910 MHz is  $8.19+j203 \Omega$  (see Figure 5.3b). While the reactance is near the necessary  $+j200 \Omega$  in order to be a conjugate match with the Higgs 3 IC, the resistance is too low, as predicted by having a higher Q.

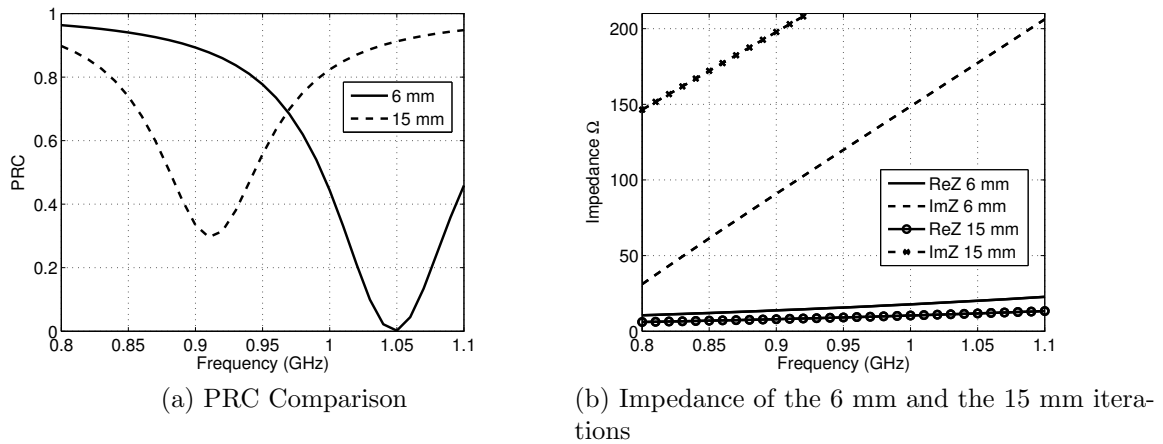


Figure 5.3. PRC and impedance plots comparing the performance of two iterations of the single dipole design shown in Figure 5.2.

Instead of increasing the spherical-cap size, another method to decrease the reactance of the antenna suggested in [47] and [48] is to spiral the feed wires. This

adds a distributed inductor to the design, providing a positive reactance contribution to the impedance of the antenna. Using this, the single dipole model was modified, incorporating helically coiled feed wires in order to allow for operation near 915 MHz. Figure 5.4 displays the results of these modifications to the HFSS model.

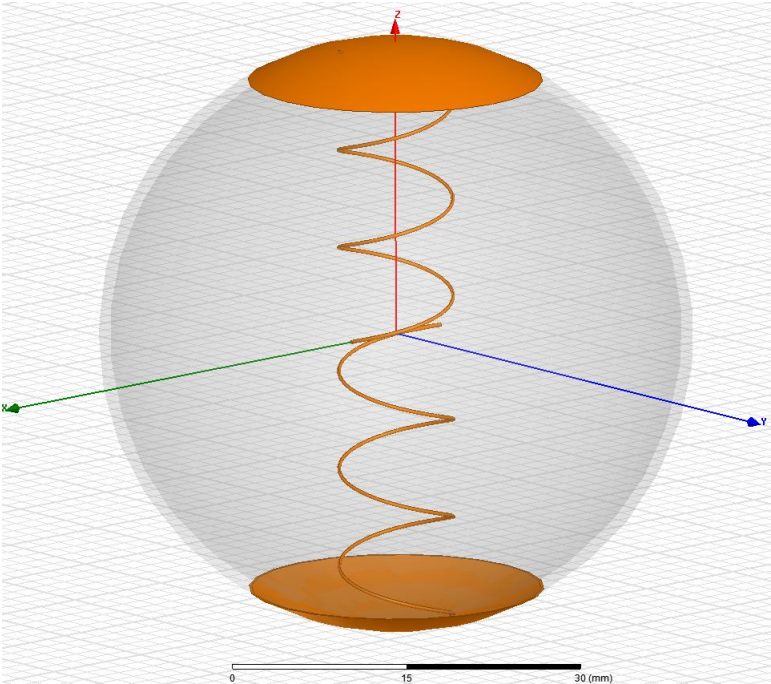


Figure 5.4. HFSS model of the helical-coil, spherical-cap, single dipole antenna with a 1 mm thick ABS shell.

The antenna shown in Figure 5.4 was simulated and modified until it operated near 915 MHz. This final design used a helical-coil radius of 2.6 mm with three turns in each feed wire. The cap height,  $h$ , used was 3 mm. The PRC and impedance plots are shown in Figure 5.5. The PRC plot in Figure 5.5a shows that the operating frequency for the antenna is 910 MHz and it exhibits a bandwidth of 21.8 MHz.

With the antenna now matched to the impedance of the Higgs 3 IC and operating in the desired RFID frequency band, the radiation pattern of the antenna needs to be addressed. As mentioned previously, the wireless sensor will not have a controlled orientation when deployed. This means the radiation pattern needs to be near-isotropic, in order to allow the measurement antenna to successfully interrogate the sensor no matter the orientation. Figure 5.6 displays the radiation pattern in the three principal planes for the helical-coil, spherical-cap single dipole antenna.

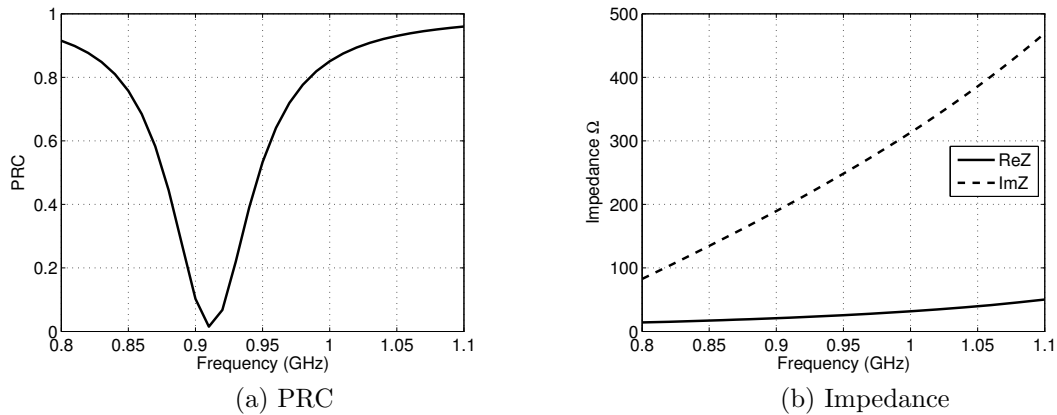


Figure 5.5. PRC and impedance plots for the helical-coil, spherical-cap single dipole design shown in Figure 5.4.

The XY-plane plot in Figure 5.6a shows that the antenna exhibits an omnidirectional pattern. The XZ and YZ-plane plots in Figures 5.6b and 5.6c, respectively, go on to show that the antenna exhibits a typical dipole radiation pattern, with distinct nulls at the poles of the radiation sphere. This would make the antenna unusable for a wireless sensor application where orientation is uncontrolled. A different antenna design is needed in order to exhibit a near-isotropic radiation pattern.

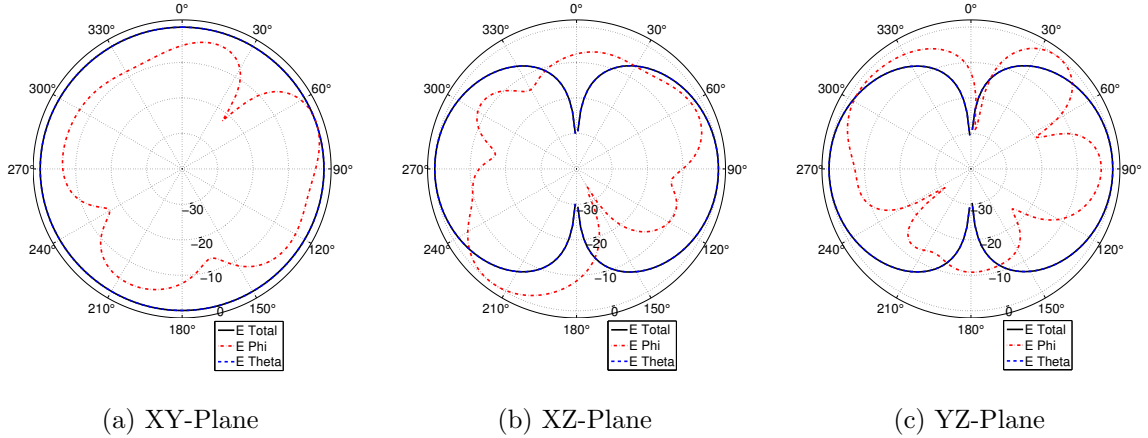


Figure 5.6. Radiation pattern plots (E-field) for the three principal planes for the antenna shown in Figure 5.4 at 915 MHz.

### 5.3. Spherical-Cap Double Dipole Design

Obtaining this near-isotropic pattern required a more complex antenna design than the single dipole. An additional dipole was added perpendicular to the original in a crossed-dipole configuration in order to provide a more isotropic pattern. This method is similar to the approach the authors took in [50]. The result is the antenna design shown in Figure 5.7.

One flaw with this design is that it is difficult to manufacture. The center of the antenna contains wires placed close together. With the wires so close, the possibility for shorts exist. While this is possibly circumvented using insulated wire, such as magnet wire used for winding transformers and inductors, the ability to reliably construct the helical-coil is still in doubt. In addition, the PCB has yet to be added to the antenna design. The PCB will eventually lie in the XY-plane of the sensor, interfering with the coil structure of two of the feeds. A different method to add series inductance to the antenna is needed, which does not consume a large portion of the internal volume of the antenna.

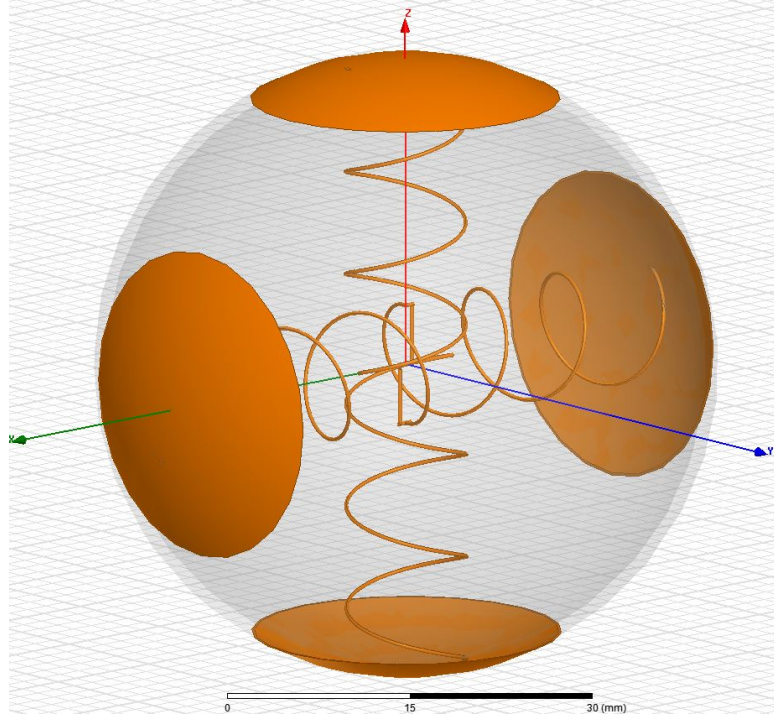


Figure 5.7. HFSS model of the helical-coil, spherical-cap, double dipole antenna with a 1 mm thick ABS shell.

Because a PCB is eventually needed to provide a platform for sensor electronics, a PCB was added in the XY-plane of the spherical volume. In addition to sensor electronics, the PCB can also be used for matching components. Instead of using a helical-coil, a single series inductor was placed onto the PCB. The resultant antenna design is shown in Figure 5.8. The PCB uses FR4 as a substrate with a thickness of 0.79 mm,  $\epsilon_r = 4.4$  and  $\tan \delta = 0.02$ . The cladding on the PCB is 1 oz. copper, which equates to a thickness of 35  $\mu\text{m}$ . The PCB offers a simple method for feeding the antenna as well. Adding single pin headers to the board allows mating connectors on each dipole leg wire to connect the antenna elements to the board. Since the ABS shell is designed to separate into upper and lower hemispheres, the design can be taken apart and modified during prototyping. The relative manufacturing simplicity

means the antenna can be produced inexpensively. This helps to satisfy the first goal set in Section 5.1. Figure 5.9 displays different views for the included PCB.

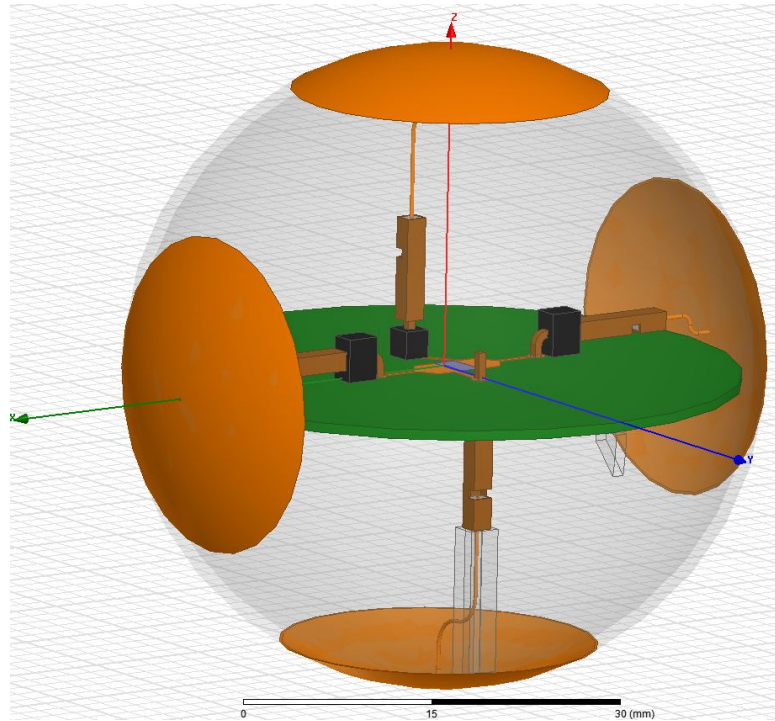


Figure 5.8. HFSS model of the spherical-cap double dipole antenna with PCB and a 1 mm thick ABS shell.

In order to test different configurations of the new double dipole design, three separate designs were created and simulated. The first was the initial design shown in Figure 5.8 with each leg of the dipole perpendicular to the other and lying in the same plane. The next design iteration rotated one leg and cap by 90 degrees. This resulted in one dipole leg orthogonal to the plane of the other three legs. This design is shown in Figure 5.10. The third and final iteration rotated the leg of the other dipole in addition to that in the previous design, creating an antenna where all four, wire legs resided in the upper hemisphere of the antenna. This design is shown in Figure 5.11.



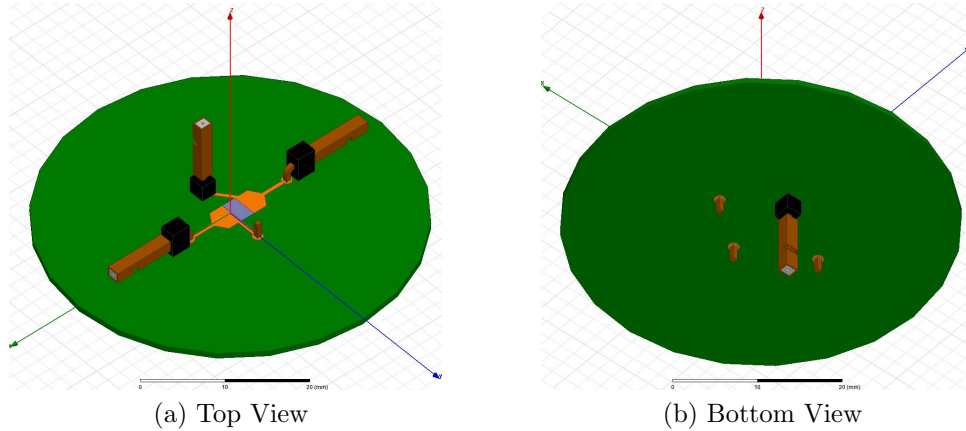


Figure 5.9. The PCB design used for sensor electronics and matching components in the double dipole antenna.

Other than a different orientation of the PCB, the second and third antenna designs shown in Figures 5.10 and 5.11 are identical. This will give these two designs similar radiation patterns. Differences in the radiation patterns, operating frequencies and bandwidths between the two designs result from the different orientation of the PCB and the consequently altered feeding schemes.

The first step in simulating the three new double dipole designs is to determine the impedance match of the antenna to the Higgs 3 IC, again by looking at the PRC. However, for the double dipole design, the included discrete, series inductor adds a complication to the analysis. HFSS does not easily allow for the simulation and modification of included discrete components. It is possible using impedance surfaces, however, this requires a full simulation every time the inductance value is changed. A better method must be used in order to facilitate fast and easy analysis through simulation.

A better way exists using the effective transmission line input impedance (see Equation 2.16). Using this, however, requires certain assumptions about the operation of the antenna to be made. The first of these is that the antenna impedance is

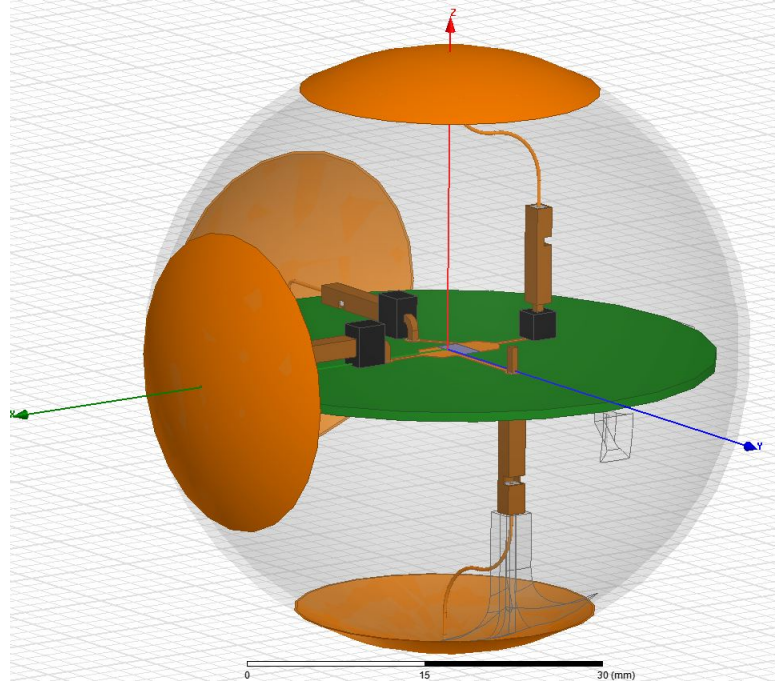


Figure 5.10. HFSS model of the second double dipole design option, with one antenna leg skewed by 90 degrees.

referenced where the RFID IC is connected, as it is for the simulations in this work. The second is that the feed lines shown emanating from the port to the header posts act as a transmission line. This allows the series inductor, placed a distance  $l$  away from the port on a transmission line with a characteristic impedance of  $Z_0$ , to be translated to the port with the correct impedance. Without the distance between the actual placement of the inductor and the port accounted for, the impedance seen by the port because of the inductor will be incorrect. With the correct impedance contribution of the inductor obtained using Equation 2.16, the antenna impedance and the effective inductor impedance are added together. This total impedance of the antenna is then applied to Equation 5.1 to obtain the PRC for the simulated antenna design and inductance value. Since this method is a post-process method, the antenna only needs to be simulated once.

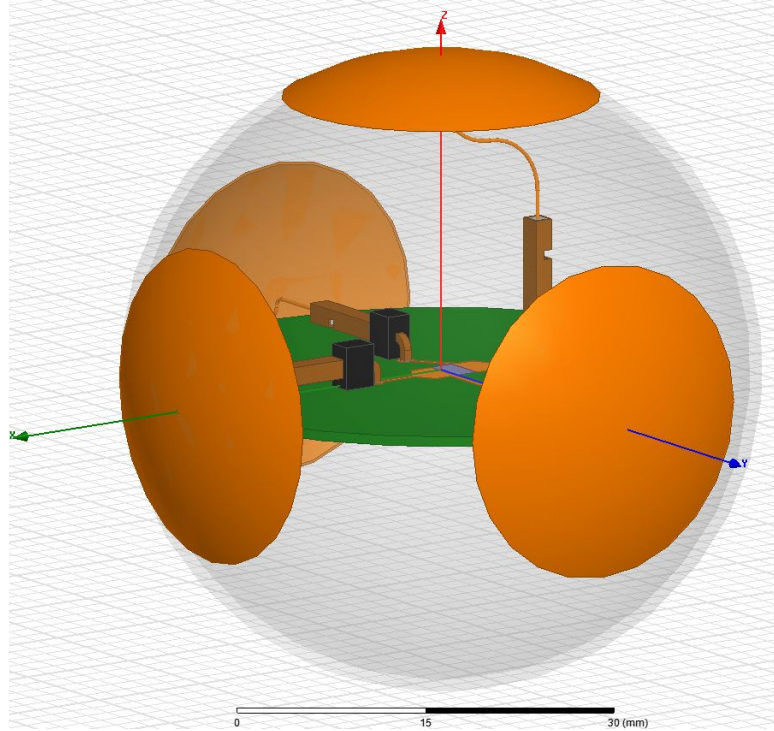


Figure 5.11. HFSS model of the third double dipole design option, with two legs skewed by 90 degrees. Note how the legs all reside in the upper hemisphere of the spherical volume.

One problem with this method, however, is determining the characteristic impedance of the assumed transmission line. While it may be possible to determine the characteristic impedance by using a two-wire transmission line model, as outlined in [11], a simpler and more accurate method is to simulate the transmission line layout separately from the antenna. Since the PCB is planar, a Method of Moments solver is a good choice for simulation. For this simulation, Advanced Design System (ADS) was used [51].

Because this method is unproven, a simple test was proposed. A microstrip transmission line on FR4 with a characteristic impedance known to be  $50 \Omega$  was first simulated. The layout of the test transmission line in ADS is shown in Figure 5.12. Looking at the figure, the ports were located on the ends of the transmission line.

Once simulated, the layout design was added to a schematic (see Figure 5.13). In the schematic, the ports from the layout were terminated with a variable impedance. The impedance of each of these terminations was defined by the same variable value. An optimization sweep was then run in order to maximize S21, which correlates to the transmission coefficient. By varying the impedance of the terminations until S21 was maximized, the final impedance of the terminations would match the characteristic impedance of the transmission line. This means that the reflections on the transmission line are minimized, as confirmed by Equation 2.14. Using the optimization tool in ADS, the characteristic impedance was found to be  $50.9 \Omega$ .



Figure 5.12. ADS layout for the test microstrip transmission line with a characteristic impedance of  $50 \Omega$ .

With the method for determining characteristic impedance using ADS validated, the feed design used for the double dipole was simulated in ADS. Using the same method, the PCB design was imported into an ADS layout from HFSS. This is shown in Figure 5.14. The design needed four ports, similar to a differential pair used for a two-wire transmission line. Once simulated, the layout was placed into a schematic where two terminations were connected in a differential setup. This is shown in Figure 5.15. The termination impedance was then optimized in order to maximize S21. The resultant characteristic impedance for the feed lines of the double dipole antenna was found to be  $188.9 \Omega$ . This result was then applied to Equation 2.16. For the  $Z_L$  term

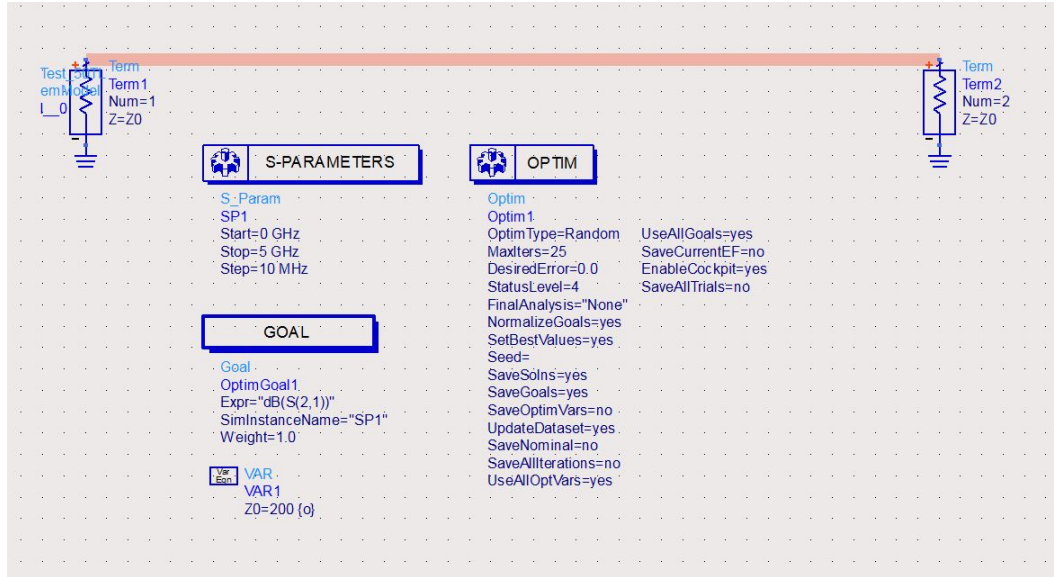


Figure 5.13. ADS schematic for the test microstrip transmission line with a characteristic impedance of  $50 \Omega$ .

in the equation, the impedance of the discrete inductor was used. For the placement of the discrete inductor, a position 1.5 mm away from the port was chosen in order to ensure enough space existed between the header post and the RFID IC.

All three designs shown in Figures 5.8, 5.10 and 5.11 were simulated using HFSS. The PRC for each was then determined using the method outlined previously. In order to match the antenna to the Higgs 3 RFID IC in the appropriate RFID band, the antenna cap height,  $h$ , and the value of the series inductor were changed. The required  $h$ , inductance value, resultant operating frequency, and bandwidth are shown for the three designs in Table 5.1. A comparison plot of the PRC for each design is also shown in Figure 5.16.

The results in Table 5.1 establish that the double dipole design shown in Figure 5.8 exhibits the most usable bandwidth. In addition, the PRC comparison (see Figure 5.16) shows that the double dipole design of Figure 5.8 exhibits the least “ripple” in the RFID band. The UHF RFID protocol in the United States is allocated 26 MHz

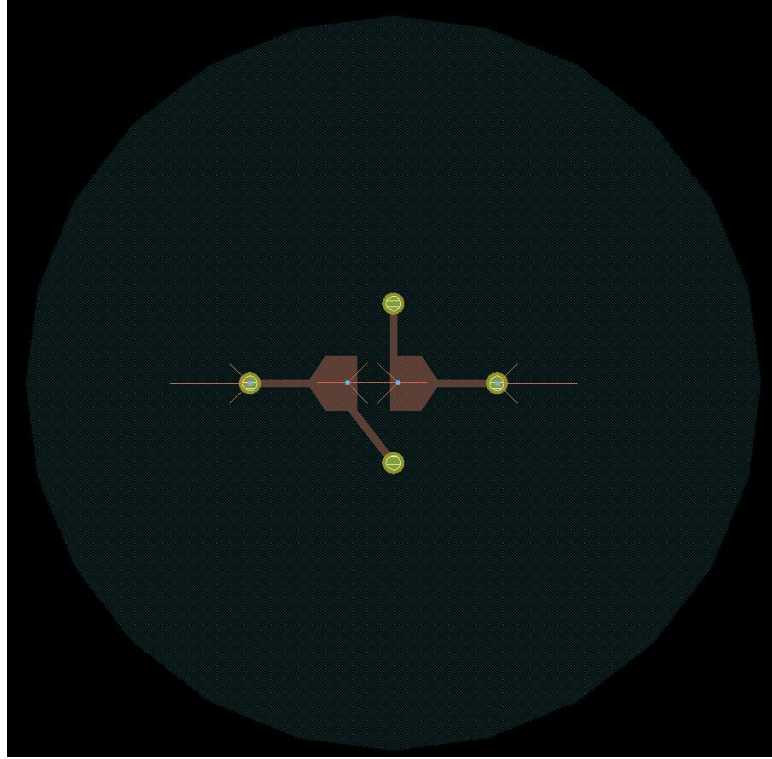


Figure 5.14. ADS layout to determine the characteristic impedance of the antenna traces used in the spherical-cap, double dipole antenna design.

of spectrum centered at 915 MHz with 500 kHz channels [2]. With electrically small antennas exhibiting limited bandwidth, covering 26 MHz of spectrum leaves a small margin of error for de-tuning of the antenna and manufacturing tolerances. The designs were purposely tuned high in order to compensate for detuning by dielectric loading, from the ground as one possible example.

With the three antenna designs matched to the Higgs 3 RFID IC impedance and with an operating frequency optimized for the desired RFID frequency band, the radiation pattern is the next design goal to compare between the different antenna designs. As mentioned in Section 5.2 for the single dipole antenna design, the nulls in the radiation pattern, as shown in Figure 5.6, will result in a wireless sensor performing poorly when the orientation is uncontrolled upon deployment. The radiation

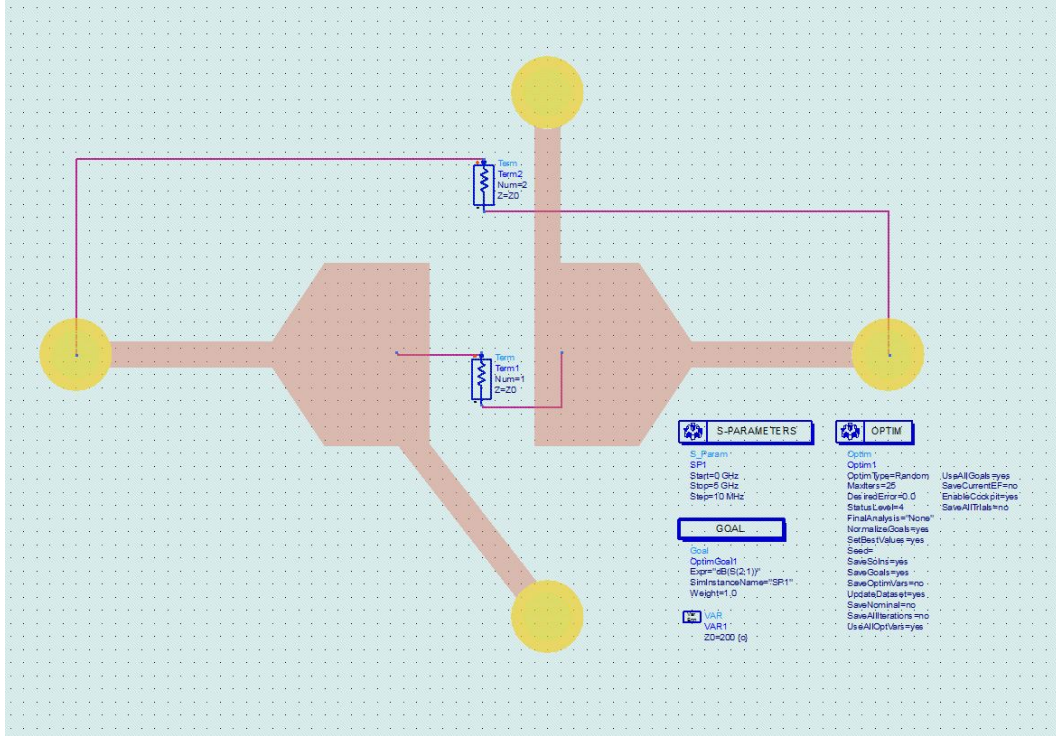


Figure 5.15. ADS schematic to determine the characteristic impedance of the antenna traces used in the spherical-cap, double dipole antenna design.

patterns for each double dipole design needs to be compared in order to determine the design with the most isotropic radiation pattern.

Instead of only analyzing the electric field intensity in each principal plane, as was done in [40], the *mean effective gain* (MEG) over the entire radiating surface of the antenna was calculated. MEG is a common metric used by the cellular industry to evaluate antennas. Because the principal planes may not always contain a null, calculating MEG ensures an accurate analysis of the entire radiation pattern and provides a figure of merit that can be used to compare dissimilar patterns. The MEG for each antenna was calculated using an isotropic power density model as outlined in [52]. This results in a MEG calculation that is equivalent except for a scaling factor to the Total Radiated Power (TRP) / Total Isotropic Sensitivity (TIS) values

Table 5.1. Bandwidth and operating frequency comparison between double dipole antenna designs. Included are the cap heights,  $h$ , and the series inductor value used for each design.

Antenna	$f_0$ (MHz)	Bandwidth (MHz)	$h$ (mm)	Inductor (nH)
None Skewed	930	55.5	3.4	33
One Skewed	$\begin{pmatrix} 866 \\ 912 \\ 982 \end{pmatrix}$	$\begin{pmatrix} 16.3 \\ 16.9 \\ 20.1 \end{pmatrix}$	3.4	33
Both Skewed	921	23	3.0	37

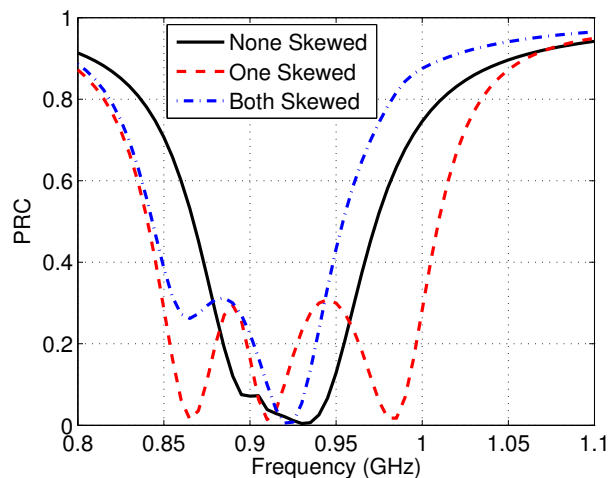


Figure 5.16. PRC comparison between the three double dipole designs.

defined in [53]. In this work, we used these scaled TRP values as defined in the CTIA standard, and mark them as MEG, where MEG is defined as

$$MEG = \frac{1}{M(N-1)} \sum_{i=1}^{N-1} \sum_{j=0}^{M-1} G(\theta_i, \phi_j) \sin(\theta_i). \quad (5.2)$$

Equation 5.2 sums all of the gain sample points, defined by  $G(\theta_i, \phi_j)$ , on the surface of the radiation sphere.  $\theta$  is the angle referenced from the positive  $z$  axis



and  $\phi$  is the angle referenced from the positive  $x$  axis (see Figure 2.4). The axes definitions are shown in each figure for the different antenna designs. The range for  $\theta$  is  $0 < \theta < 180$  degrees and the range for  $\phi$  is  $0 \leq \phi < 360$  degrees. With a two degree step size used for both  $\theta$  and  $\phi$ , this resulted in  $M$  equaling 180 and  $N$  equaling 90. The reason for the  $\sin(\theta_i)$  term in Equation 5.2 is to compensate for the non-constant sample point density throughout the surface of the radiation sphere. Since the sample points are at a constant step in both  $\theta$  and  $\phi$ , the point density trends toward infinity at the poles of the radiation sphere.

Table 5.2 displays the results for the three single dipole designs in Section 5.2 as well as the three double dipole designs. The single dipole designs were used as a baseline comparison. The results establish that the double dipole configuration with none of the dipole legs skewed (shown in Figure 5.8) displayed the most isotropic pattern. Figure 5.17 displays the simulated electric field intensity plots for the three principal planes of the chosen design.

Table 5.2. Gain comparison between antenna designs.

<b>Antenna</b>	<b>MEG (dBi)</b>	<b>Max Gain (dBi)</b>	<b>Min Gain (dBi)</b>
Single Dipole 6 mm	-0.63	2.09	-53.70
Single Dipole 15 mm	-0.67	2.05	-40.41
Single Dipole Spiral	-0.79	1.75	-47.29
Double None Skewed	-0.45	1.81	-8.07
Double One Skewed	-0.64	1.77	-16.06
Double Both Skewed	-0.66	1.53	-14.70

Using the results of simulation data, shown in Tables 5.1 and 5.2 and Figures 5.16 and 5.17, the antenna pictured in Figure 5.8 was determined as the best candidate for prototyping. For a wireless sensor, the most important aspects are gain, radiation

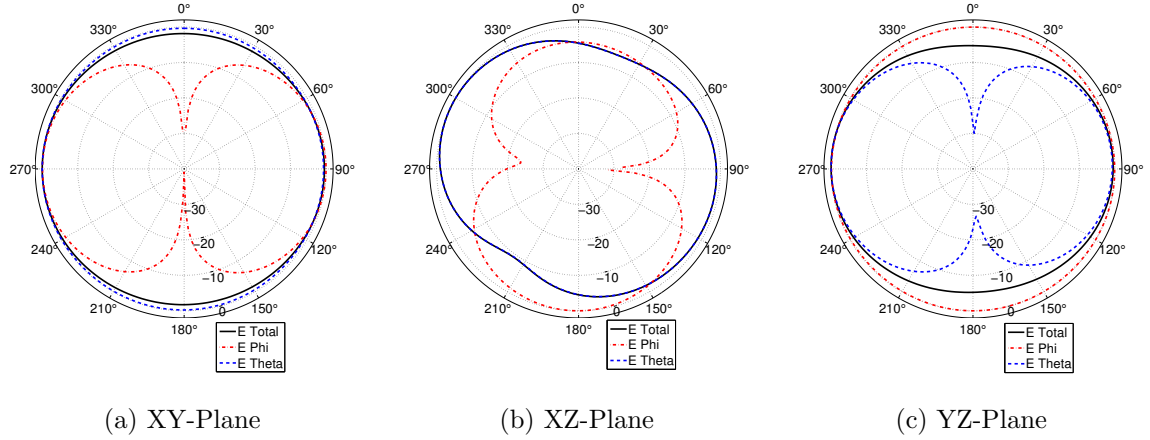


Figure 5.17. Simulated, normalized, electric field intensity patterns for the prototype antenna shown in Figure 5.8 at 915 MHz.

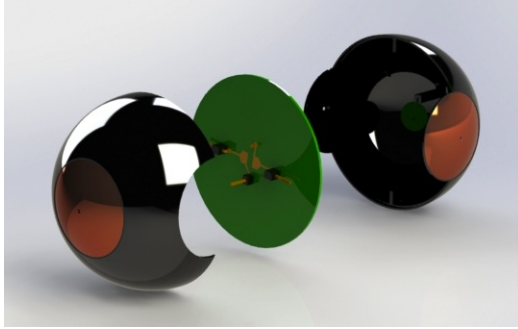
pattern and bandwidth. In this case, since we are comparing low-directivity antennas, MEG may be used in place of gain and radiation patterns to compare performance. Out of all of the antenna designs simulated, the design in Figure 5.8 exhibited the highest MEG of  $-0.45$  dBi, as shown in Table 5.2. This will be extremely advantageous in situations where the sensor orientation during deployment is uncontrolled. A radiation pattern with a large null will cause a large number of sensors to perform poorly. A near-isotropic radiation pattern ensures the sensor will work regardless of orientation. Additionally, the antenna of Figure 5.8 displayed the smallest magnitude null and smallest range of gain, as shown in Table 5.2.

## CHAPTER 6. ANTENNA PROTOTYPING AND MEASUREMENT

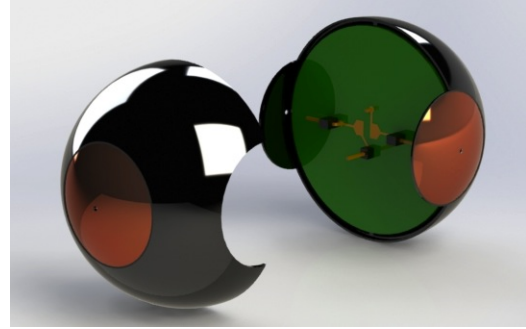
Through the simulation work performed in Chapter 5, an antenna design was chosen to be prototyped and tested. The prototype antenna design is shown in Figure 5.8. This chapter summarizes how the antenna was made, details the measurement setup, and outlines the test procedure used. In addition, the measured results are compared to the simulated results of Chapter 5. Lastly, the performance of this antenna design is compared to similar designs.

### 6.1. Constructing the Prototype

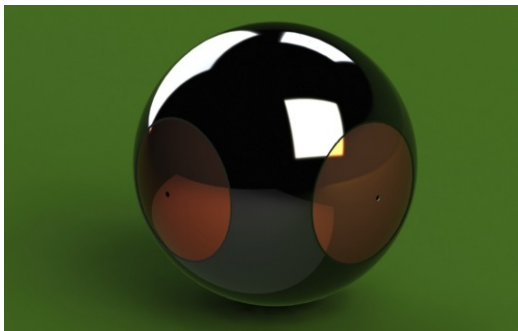
The first step toward prototyping the antenna was designing the ABS shell. Using a 3D CAD modeling tool, the shell was modeled in order to accommodate the antenna design and the internal PCB. Supports were also added in order to hold the PCB in place as well as support the antenna wires. The antenna wire supports hold the connectors in place in order to facilitate assembly. The entire assembly process is shown in Figure 6.1. The shell is designed to separate into upper and lower hemispheres. This allows the PCB to be placed inside of the bottom hemisphere. The upper hemisphere is then placed on top, sealing the interior of the sensor volume. If needed, it is then possible to disassemble the sphere if a modification needs to be made or maintenance needs to be performed on the sensor electronics. Figure 6.1a shows the three components of the sensor. While the spherical-caps are shown, the feed wires and the connectors are not shown. However, the headers on the PCB for connecting the antenna elements are shown. Figure 6.1b demonstrates how the PCB is first inserted into the bottom hemisphere. The two side spherical-caps are connected at this time. Figure 6.1c then shows the completed model, with Figure 6.1d showing a view of the internal volume of the wireless sensor.



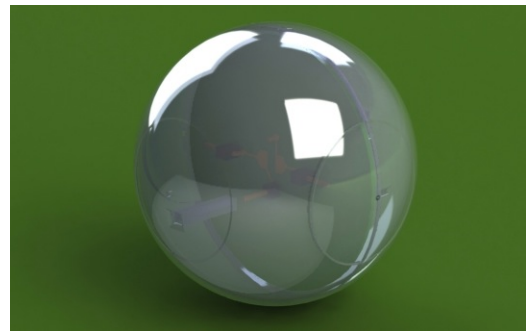
(a) Model of the upper antenna hemisphere, PCB, and bottom antenna hemisphere before assembly.



(b) Model of the assembled bottom antenna hemisphere and PCB, along with the top antenna hemisphere.



(c) Model of the fully assembled antenna.



(d) Model of the fully assembled antenna with the inner sensor volume shown.

Figure 6.1. Assembly of the antenna.

With the antenna modeled, the first step was to produce the ABS shell. A 3D printer was used to manufacture the two 1 mm thick hemispheres. Next, the PCB was manufactured using a rapid prototyping circuit board plotter. With the PCB produced, the UHF RFID IC was attached to each board. The IC was contained in a strap, which was glued onto the PCB using a conductive epoxy. Then, the series inductor was placed onto the feed traces of the PCB and the header posts were soldered on. Figure 6.2 shows the completed PCB.

With the PCB finished, the antenna structure was assembled. Each spherical-cap was made out of 100 um thick, adhesive-backed copper tape, which allows it to adhere to the surface of the ABS shell. In order to get the exact size of spherical-

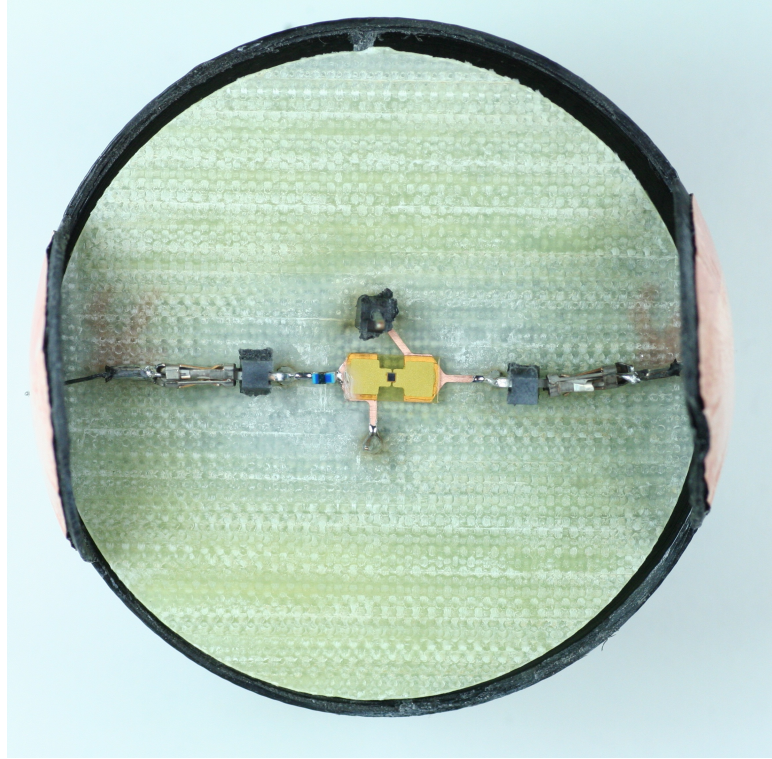
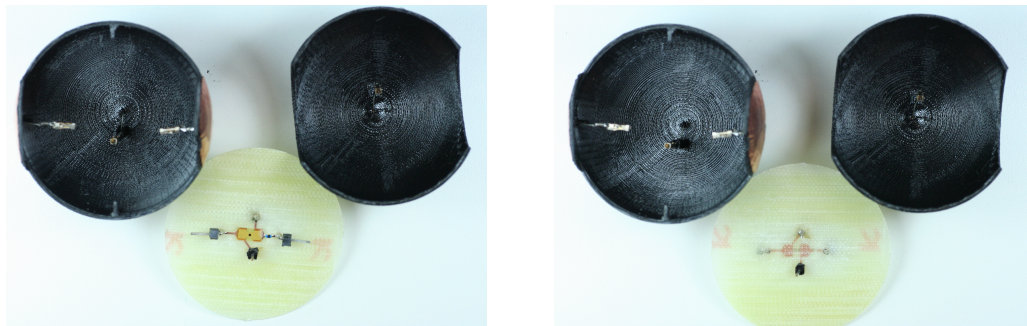


Figure 6.2. The fully assembled PCB shown placed into the bottom hemisphere of the ABS shell.

cap required, a laser was used to accurately cut the necessary size from the copper tape. The spherical-caps were then placed onto the ABS shell. Using 28 AWG wire with a diameter of 0.321 mm, the feed wires were soldered onto the spherical-caps. The header connectors were then soldered onto the ends of the feed wires. With the antenna structure completed, the wireless sensor antenna was then assembled. Figure 6.3 shows the three separate components of the wireless sensor antenna: the upper and lower hemispheres of the ABS shell and the PCB. Figures 6.3a and 6.3b give the top and bottom view of the PCB, respectively. Figure 6.4 shows the partially assembled antenna prototype, with the PCB inserted into the bottom hemisphere. Figures 6.4a and 6.4b give a side and top view of the partially assembled antenna, respectively. Finally, Figure 6.5 shows the completed wireless sensor antenna with

Figures 6.5a and 6.5b giving two separate views of the antenna. Notice in Figure 6.5b, the clear evidence of solder on the top spherical-cap where the feed wire was attached to it. The banding look present in Figure 6.5 of the ABS shell is a result of the 3D printer using a fused deposition modeling process. With the manufacturing occurring in-house and simple construction, the first goal outlined in Section 5.1 is met.



(a) Exploded Antenna: Top view of the PCB.

(b) Exploded Antenna: Bottom view of the PCB.

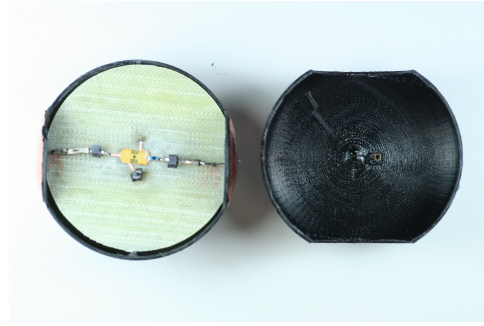
Figure 6.3. Exploded antenna showing the top and bottom hemispheres of the ABS shell and the completed PCB.

## 6.2. Testing the Prototype Antenna

With the prototype antenna completed, it was possible to test the functionality of the design. Taking performance measurements of the prototype validates the simulation results and provides insight on the ability to successfully manufacture the antenna design. A 3 meter anechoic chamber was used to test the prototype in order to obtain interference free, repeatable results. The complete test setup is shown in Figure 6.6. The prototype antenna was affixed to a block of styrofoam, where a small hollow made in the Styrofoam prevented the prototype antenna from being jostled. Because Styrofoam has similar electrical characteristics to air, having



(a) Partially assembled antenna from the side.



(b) Partially assembled antenna from the top.

Figure 6.4. Partially assembled antenna.



(a) Side view of the fully assembled antenna.

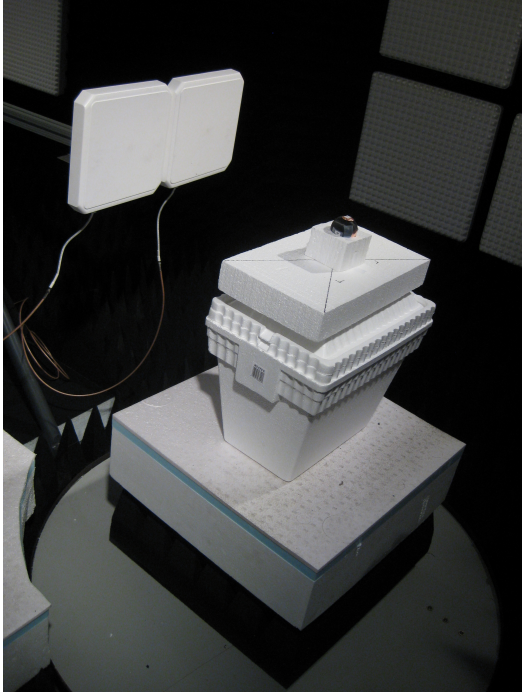


(b) Alternate view of the fully assembled antenna.

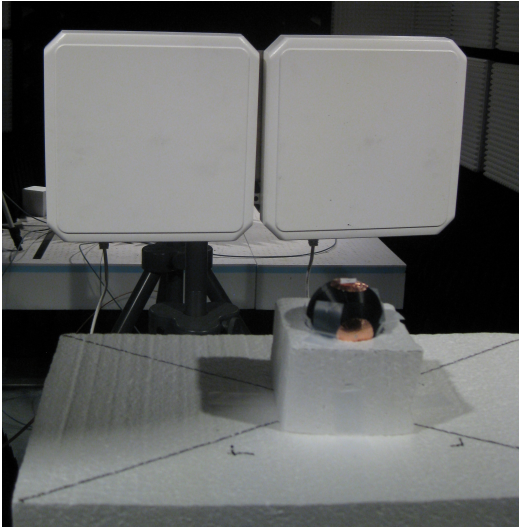
Figure 6.5. Fully assembled wireless sensor antenna.

it close to the prototype antenna negligibly affected the measured results. The entire Styrofoam assembly was then positioned on top of a Styrofoam tower. The tower was then placed onto a turntable. The turntable allows accurate positioning of the prototype antenna during testing in order to obtain a complete radiation pattern measurement. This is shown in Figure 6.6a.

Two left-hand, circularly polarized patch antennas were used to perform the measurements. Circularly polarized antennas were used rather than linearly polarized antennas since this presents a more realistic real-world measurement scenario. One antenna was responsible for interrogating the RFID IC on the prototype antenna while the other antenna received the backscattered radiation. The two antennas were placed side-by-side, 0.47 meters from the center of rotation of the turntable. Figure 6.6b shows the antenna placement in relation to the prototype antenna.



(a) Measurement antennas and turntable.



(b) Test setup showing the prototype antenna in a Styrofoam block, with the measurement antennas in the background.

Figure 6.6. Complete measurement test setup.

To obtain the radiation pattern measurements, the turntable was then stepped from 0 degrees to 350 degrees in steps of 10 degrees while the response of the prototype



antenna was measured. In order to obtain a radiation pattern from each of the three principal planes (XY, XZ, YZ) the prototype needed to be physically realigned between each measurement run. The principal planes used for measurement are the same as those defined by the axes in Figures 2.4 and 5.8.

Because an electrically small antenna is difficult to measure directly, a relative method was used. This method uses an RFID reader with an adjustable output power. For each angle step in the radiation pattern, the power output is decreased until the RFID reader is no longer able to read the RFID IC. The lowest power level is then recorded for that angle in the radiation pattern. The RFID reader used here uses a software-defined radio (SDR) in order to allow power levels to be stepped at fixed frequency points. The RFID reader used is based off of the USRP1 software-defined radio system presented in [21]. The software required some modifications in order to allow a frequency sweep from 800 MHz to 1 GHz, the limit of the USRP 1 hardware. A power amplifier was added in-line to the interrogation antenna, compensating for cable losses between the measurement system and the measurement antenna as well as the low output power available from the USRP 1. A directional coupler and power meter are used in order to determine the current output power. Calibrating the system allows for an accurate determination of the power level provided to the interrogating antenna. With this accurate power measurement and a fixed distance between the measurement antennas and the prototype antenna, it is possible to determine the theoretical maximum read range. From [54], the maximum read range  $r$  may be determined using

$$r = d\sqrt{\frac{EIRP}{P_{min}G_t}} \quad (6.1)$$

where EIRP stands for the equivalent isotropically radiated power in reference to the measurement antennas (transmit power multiplied by transmit antenna gain),  $P_{min}$

is the minimum turn-on power of the RFID IC measured at the measurement antenna port, and  $G_t$  is the gain of the measurement antennas.

The response from the prototype antenna was measured in 5 MHz steps from 800 MHz to 1 GHz at each turntable position in the three principal planes. The upper frequency was limited to 1 GHz (versus the 1.1 GHz upper limit of the simulation data) because of the hardware limitations of the USRP1. Using the measured data and Equation 6.1, the prototyped antenna is compared to the simulated results in the next section.

### 6.3. Results of the Prototype Antenna

Using the data collected according to the procedure outlined in Section 6.2, the resulting maximum read range at 915 MHz was computed using Equation 6.1 and plotted in Figure 6.7. As predicted in the simulated XY-plane radiation pattern (Figure 5.17a), the measured XY-plane displayed in Figure 6.7a shows the best response, achieving a maximum read range of approximately 3.5 meters. The measured XZ-plane shown in Figure 6.7b does not achieve as great a beamwidth as the XY-plane but still achieves a maximum read range of approximately 3.5 meters. The asymmetry of the radiation pattern is similar to the simulation results shown in Figure 5.17b. The measured YZ-plane, shown in Figure 6.7c, exhibits the poorest results. However, the read ranges are generally greater than 1 meter. While the simulated results, shown in Figure 5.17c, did not predict that the YZ-plane would exhibit the worst response, the symmetry of the responses do correlate well.

The three measured radiation patterns (see Figure 6.7) confirm the near-isotropic radiation pattern of the prototype antenna. None of the plots contained a significant null, as would be present if the antenna was only omni-directional. It seems that from the comparison between the maximum read range plots, shown in Figure 6.7, and the simulated radiation patterns, shown in Figure 5.17, that the prototype

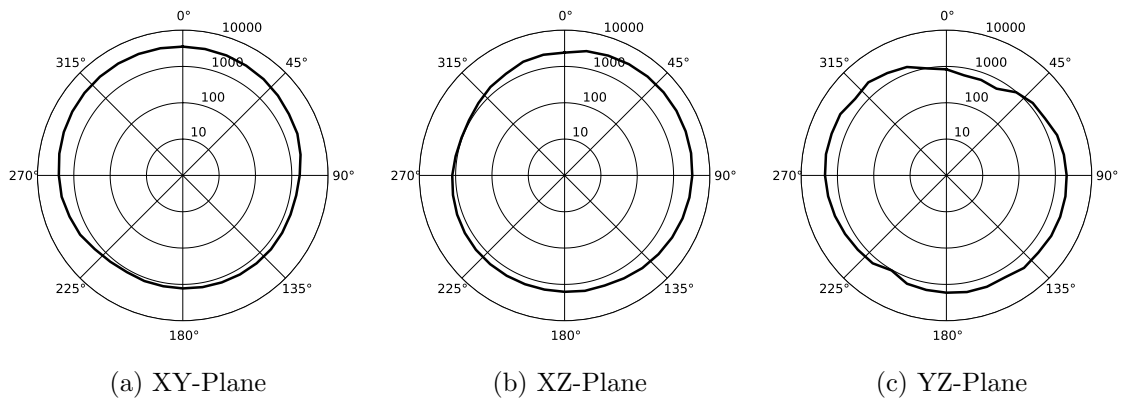


Figure 6.7. Relative radiation pattern measurements given as maximum read distance calculated using Equation 6.1. The units are in mm.

antenna correlates well with the simulated data. However, this visual comparison is not completely satisfactory. A more quantitative comparison method is required.

While the performance metrics outlined in Chapter 5 cannot be directly compared, certain manipulations allow for a useful comparison. For example, PRC cannot be directly compared to the minimum turn-on power measured during testing in Section 6.2. However, noticing that PRC is a power metric where minimization leads to better performance, this appears equivalent to the minimum turn-on power measurements, where the lower the transmit power required to turn on the RFID IC, the better the performance.

Starting with the Friis equation, Equation 2.13, it is possible to relate PRC and minimum turn-on power using

$$\begin{aligned} \frac{P_r}{P_t} &= G_t G_r \left( \frac{\lambda}{4\pi R} \right)^2 \\ \implies P_r &= P_t G_t G_r \left( \frac{\lambda}{4\pi R} \right)^2, \end{aligned} \quad (6.2)$$

$$\begin{aligned} P_{th} &= P_r (1 - |s|^2) \\ \implies P_r &= \frac{P_{th}}{1 - |s|^2} \end{aligned} \quad (6.3)$$

where  $P_{th}$  is the power required to turn on the RFID IC and  $|s|^2$  is PRC, defined in Equation 5.1. Equation 6.3 states that the power received by the RFID IC antenna needs to be greater than the IC threshold power by an amount equal to the power lost due to reflections between the RFID IC and the antenna.

Using the resulting equations, Equations 6.2 and 6.3, along with the fact that  $P_{th}$ ,  $G_t$ ,  $G_r$ , and  $R$  are all constant, the relation between minimum turn-on power and PRC is possible to be derived as

$$\begin{aligned} P_r &= P_t G_t G_r \left( \frac{\lambda}{4\pi R} \right)^2, \\ P_r &= \frac{P_{th}}{1 - |s|^2} \\ \implies \frac{P_{th}}{1 - |s|^2} &= P_t G_t G_r \left( \frac{\lambda}{4\pi R} \right)^2 \\ \implies \frac{P_{th}}{1 - |s|^2} &= P_t \lambda^2 K, \text{ where } K = \frac{G_t G_r}{(4\pi R)^2} \\ \implies P_t &= \frac{P_{th}}{(1 - |s|^2) \lambda^2 K} \\ \implies P_{min \text{ turn-on power}} &= \frac{1}{(1 - |s|^2) \lambda^2 K}. \end{aligned} \quad (6.4)$$

From Equation 6.4, it can be seen how the measured minimum turn-on power is related to the PRC. By normalizing the results, the constant  $K$  is eliminated and both values are able to be compared. Figure 6.8 displays this comparison.

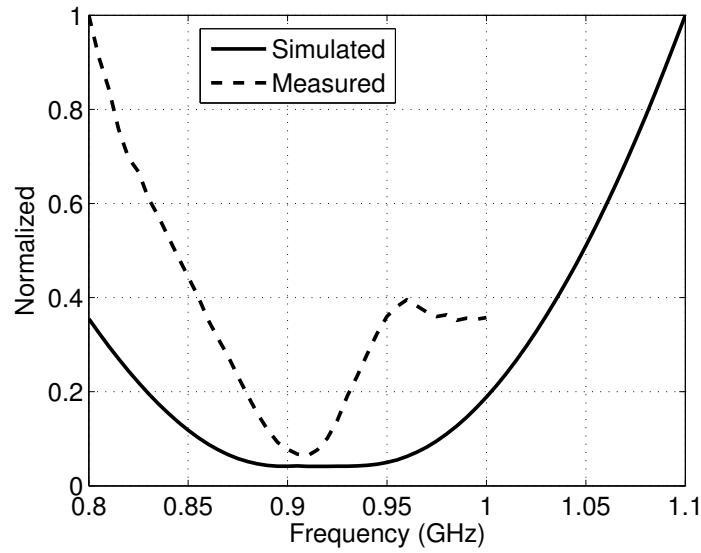


Figure 6.8. Normalized plot, comparing the simulated PRC for the prototype antenna to the measured minimum turn-on power.

Figure 6.8 compares measured and simulated results. A reasonable correlation is shown. The minimum turn-on power for the measured results occurs at 910 MHz, which is below that of the simulated results with the simulated operating frequency being 930 MHz, shown in Table 5.1. Additionally, it appears from the figure that the operational bandwidth of the measured results is lower than what simulation predicted. The deviation of the measurements from simulation could arise from multiple sources. The wire length used was generally uncontrolled, with the only constraints being approximate measurements and what was needed for successful assembly. Another source of error results from inductor tolerance, placement location

tolerance, non-ideal inductor effects such as series resistance and the effect of the solder fillets on the response of the inductor. The impedance of the RFID IC is also another error source. It is likely that non-linear effects are present which the RC model does not account for. Considering these sources of error, the deviation of the measured values from simulation is reasonable.

The second metric for evaluating the performance of the antenna is the radiation pattern. In Chapter 5, this was accomplished by observing the electric field intensity in each principal plane (XY, XZ, YZ) and analyzing the total gain of the antenna across the entire radiating surface. MEG, as defined by Equation 5.2, was used for analysis, along with observing the deviation of gain by determining the maximum and minimum gain. For the measured results, long testing times prevented measurements across the entire radiation surface. Additionally, absolute values for gain and electric field intensity could not be determined because of the antenna being electrically small. With an electrically small antenna, it is difficult to feed it externally (with test equipment) without significantly modifying its operation. The fact that the RFID IC impedance was complex also adds complications to obtaining absolute measurements. As with the simulated PRC to measured results comparison, a relative method will again be used to compare the simulated radiation pattern to the measured results.

The measured results for a radiation pattern are plots of the maximum read range of the antenna as it is swept through each principal plane. Equation 6.1 defines maximum read range, as plotted in Figure 6.7. In the equation, the currently measured power is compared to the legal limit set by the appropriate regulating agency for the country or region in which the antenna is operating. If the currently measured power is less than EIRP, the legal limit, the maximum read range is greater than the current distance by a factor of the square root of this ratio. In other words, read range is proportional to the square root of power.

Field intensity, in contrast, is given in terms of volts per meter. From [8], field intensity is related to power as

$$\mathcal{S}_{av} = \frac{|\mathbf{E}|^2}{2\eta} \quad (6.5)$$

where  $\mathcal{S}_{av}$  is time-average power density in watts per square meter,  $\mathbf{E}$  is the electric field intensity in volts per meter and  $\eta$  is the intrinsic impedance of the medium where  $\mathbf{E}$  exists. Equation 6.5 assumes that the propagating wave is a TEM mode in an isotropic medium. Restating Equation 6.5, field power is proportional to the square of the electric field intensity. Then, with respect to the electric field intensity, the electric field intensity is proportional to the square root of power. With this, it can be said that the electric field intensity is directly proportional to the maximum read range. By plotting both the normalized quantities of maximum read range and field intensity, it is possible to directly compare the two quantities. This allows for an analysis of how well the relative measured radiation pattern of the prototype antenna matches with the predicted radiation pattern given by simulation. Figure 6.9 displays this comparison.

Figure 6.9 shows that in the three principal planes, the antenna exhibits a near-isotropic pattern. For the XY-plane shown in Figure 6.9a, the measured results show a different front-to-back ratio than simulation predicted. The XZ-plane shown in Figure 6.9b, shows good agreement, with the worst error occurring around 120 degrees through the sweep. The YZ-plane shown in Figure 6.9c shows excellent agreement, with only a minimal null occurring in the measured results at the poles. Differences between the measured and simulated results likely stem from the manufacturing tolerances listed previously. Overall, however, the measured results confirm the near-isotropic radiation pattern of this antenna design.

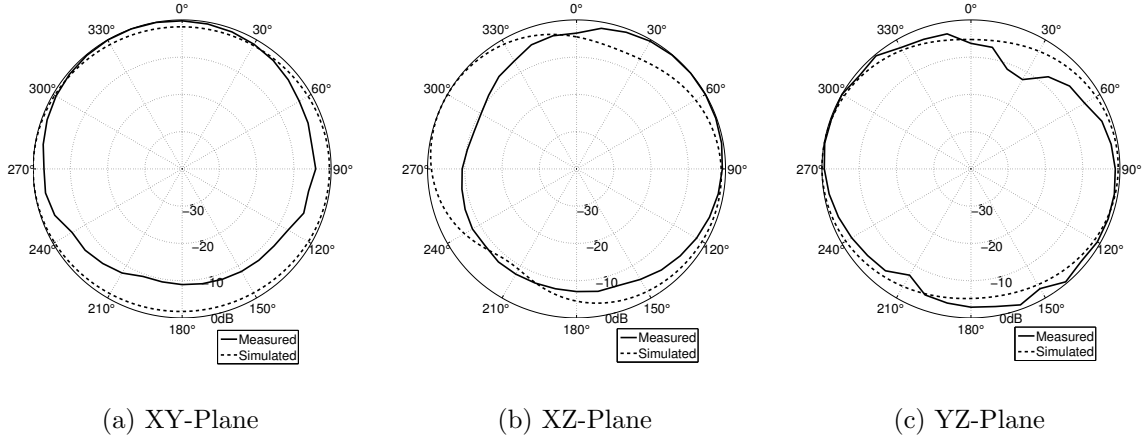


Figure 6.9. Normalized radiation pattern comparison at 915 MHz between the simulated total electric field intensity, shown in Figure 5.17, and the minimum read range plot, shown in Figure 6.7.

#### 6.4. Design Repeatability

While Section 6.3 proved the performance of the antenna design as predicted by simulation, it did not prove whether the design was able to be repeatably produced. The only way to determine this was to manufacture additional prototypes. Because of limited resources for this project, only three additional prototypes were produced and tested. The production and testing of these prototypes was the same as outlined in Sections 6.1 and 6.2, respectively. With the simulated results already compared with the measured results from the first prototype sphere, the results given in this section compare the measured results of the three new prototype antennas with that of the first. Figure 6.10 shows a comparison of the normalized, measured minimum turn-on powers between the four prototype antennas as well as simulated PRC for reference. Figure 6.11 compares the maximum read ranges in each principal plane between the four prototype antennas at 915 MHz.



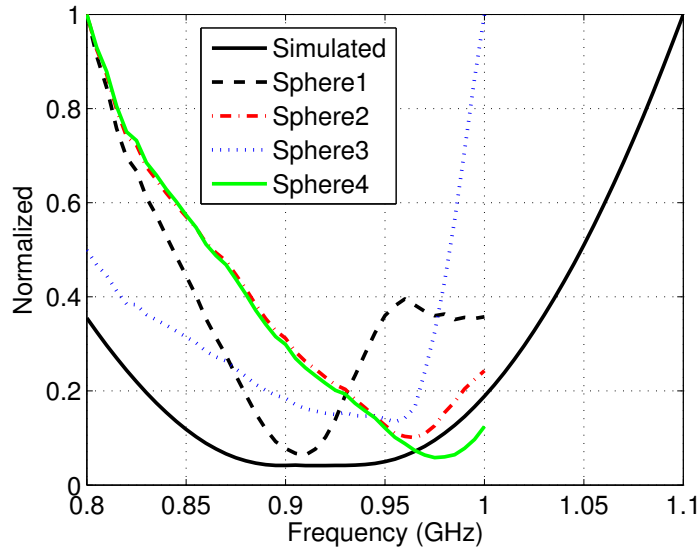


Figure 6.10. Normalized plot, comparing the measured minimum turn-on power between the four prototype antennas.

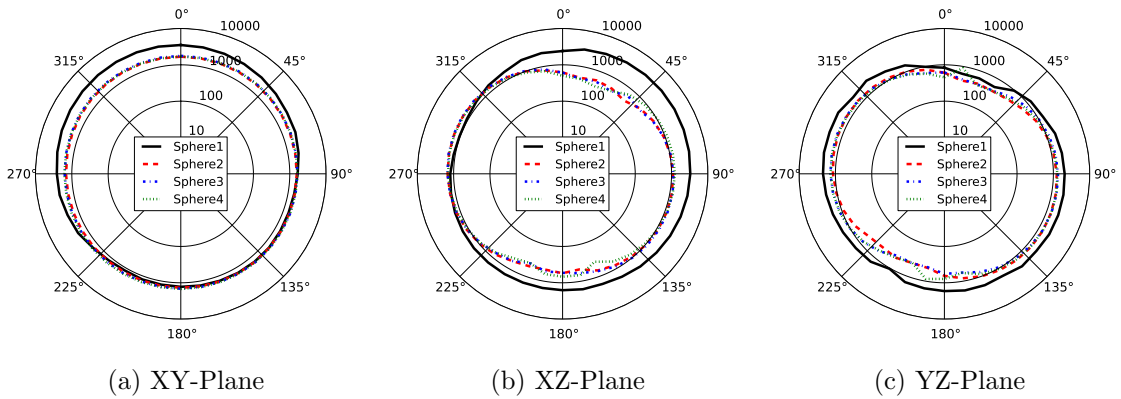


Figure 6.11. Normalized radiation pattern plots comparing the minimum read range between the four prototype antennas at 915 MHz.

In Figure 6.10, the three newest prototype antennas (Sphere2, Sphere3, and Sphere4) appear to be tuned higher than the original (Sphere1). The minimum turn-on power for Sphere1 occurs at 910 MHz, while it appears the three newest antennas are near 965 MHz. The reason for this is because of the spherical-caps used

for the newer antennas. Because of an error with laser cutting, the spherical-caps used were smaller than intended. A smaller sized spherical-cap explains the higher operating frequency for the three newer prototype antennas. While Sphere3 does not appear to operate well, it appears the performance was trending with that of Sphere2 and Sphere4. The Sphere3 data exhibits a known problem with the USRP1 test setup, which causes the hardware to unsuccessfully interrogate RFID tags in some instances, resulting in invalid data at certain frequency points. With this knowledge, Sphere3 may have an operating point similar to that of Sphere2 and Sphere4, near 965 MHz. While the newer prototype designs didn't match the response of the original prototype, the repeatability between the three newer designs confirms the ability to reliably and repeatedly manufacture this design.

With the previous results showing that the three new prototype antennas operate at a higher frequency than the original, it is expected that the maximum read range will suffer at 915 MHz compared to the original design. Figure 6.11 confirms this expectation. While the maximum read range for the three newer prototype antennas is generally less, the overall shape in all three principal planes is similar to the first prototype. The same behavior should then be exhibited at 965 MHz, except with the three newer prototypes having a greater maximum read range than the first prototype. Figure 6.12 displays this data.

Because the overall shape of the patterns match between the four prototype antennas in both Figures 6.11 and 6.12, it is logical to conclude that attaining a repeatable, near-isotropic radiation pattern is possible with this antenna design. Besides an operating frequency shift because of a manufacturing error, the wireless sensor antenna platform presented in this chapter meets the goals set in Section 5.1. For the first goal, Figure 6.5 shows that the prototype antenna is small in size and does not require expensive methods or materials for manufacturing. Figures

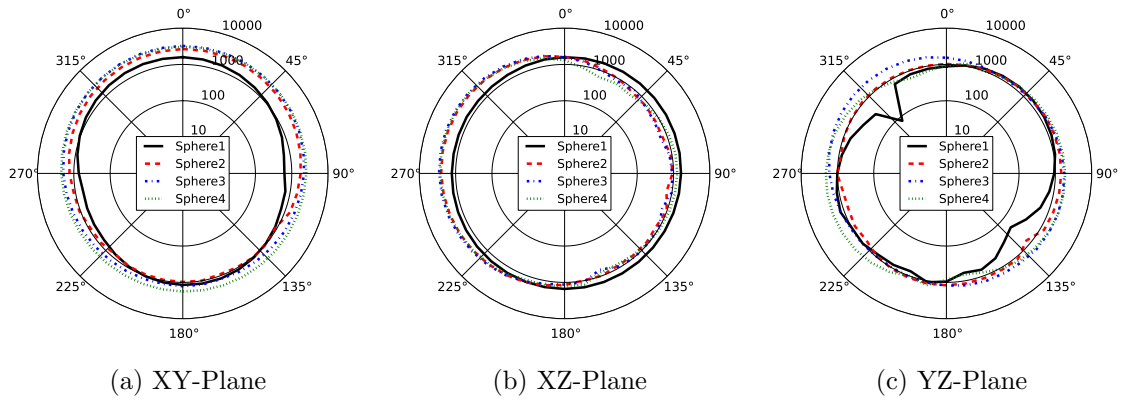


Figure 6.12. Normalized radiation pattern plots comparing the minimum read range between the four prototype antennas at 965 MHz.

6.9, 6.11, and 6.12 show that the antenna design exhibits a near-isotropic radiation pattern, satisfying the second goal. The third goal states that the antenna must operate and span the UHF RFID spectrum for the United States. While only the first prototype is within this band (902 MHz to 928 MHz), it is shown in Figure 6.10 that all four prototype antennas exhibit the necessary bandwidth to span the band, excluding any manufacturing defects. The fifth goal states that the antenna must be rugged. Compared to the previous sensor designs in Chapter 3, the ABS shell significantly improves the ruggedness of the prototype sensor platform. Adding a conformal coating to the outside would further strengthen the design against external environmental factors. The fourth goal, stating that the antenna must integrate with sensor electronics, will be explored in the next chapter.

## CHAPTER 7. SENSOR ELECTRONICS INTEGRATION

The test results shown in Chapter 6 show that the antenna design developed meets the criteria formulated in Section 5.1. While the antenna design is a major portion of a wireless sensor, the electronics used are what determine its functionality. Just using an RFID IC does not constitute a working sensor. This chapter finalizes the work of developing a wireless sensor platform. The prototype antenna of Chapter 6 is integrated with a new RFID IC, capable of taking thermal measurements and interfacing with other sensor electronics. The effect of this change on the performance of the antenna is analyzed through simulation and by testing manufactured prototypes.

### 7.1. Multifunctional RFID IC

As mentioned in Section 3.1, the RFID protocol is an attractive communications solution for wireless sensors. The RFID protocol allows for minimal power expenditure by the wireless sensor, instead relying on the RFID reader to provide power for the communications medium. Furthermore, the communications circuitry required for the wireless sensor is minimal. All these factors contribute to a low cost sensor design. However, the Alien Higgs 3 UHF RFID IC [45] does not provide any interface for the external electronics required in a wireless sensor. In order to create a working prototype wireless sensor, a different RFID IC needed to be chosen or developed.

Fortunately, there currently exist solutions for interfacing an RFID IC with external electronic components. Two such solutions which exist currently are from IDS Microchip [55] and Impinj [56]. Using these ICs, the antenna design of Chapter 6 could perform temperature measurements and interface with other sensor electronics on the PCB. Only minimal modifications to the series matching inductor and the spherical-cap size need to be made in order to match the antenna to the different

input impedances of the ICs. By making these changes, a suitable wireless sensor can be designed.

## 7.2. Initial Wireless Sensor Design

The antenna design utilizing the new RFID IC does not contain any additional sensor electronics. This was done in order to ensure that the antenna could be more simply matched to the new RFID IC, without accounting for the effects of the additional electronics on the performance of the antenna.

The UHF RFID IC by IDS Microchip [55] was chosen for the wireless sensor design. The motivation for this design choice was the in-house availability of the IDS IC. The IC exhibits an input impedance of  $31-j320 \Omega$  at 860 MHz [55]. This was the value provided by the datasheet and an equivalent circuit model was not provided. Since input impedance is inherently frequency dependent, an equivalent circuit was determined which exhibited similar impedance characteristics. This equivalent circuit took the form of a parallel RC circuit, with a parallel resistance of  $3.334 \text{ k}\Omega$  and a parallel capacitance of  $569.6 \text{ fF}$ . This equates to an impedance of  $27.7-j302.8 \Omega$  at 915 MHz. Therefore, the redesigned antenna will need to present the RFID IC with a conjugate impedance of  $27.7+j302.8 \Omega$  at 915 MHz.

The IDS IC contains internal circuitry which makes it suitable for use in a wireless sensor. Besides RFID communications, the IC also has built-in temperature sensing circuitry. Additionally, if the IC is externally powered, it is able to measure and store temperature data periodically, even when not being actively interrogated. The IC also contains serial communications in order to interface with external sensor electronics. This allows the IC to actively control and gather data from other electronic devices. It is then able to communicate the additional data using the RFID communications protocol. These features make the IDS IC an excellent choice for wireless sensing applications.

The first step in redesigning the antenna is to determine the PCB layout needed. This includes the footprint for the IC, antenna traces and other related components needed to successfully integrate the new IC to the antenna design. The changes needed for the IDS IC include a different footprint, a modified layout of the antenna traces, and an added capacitor. The capacitor connects to the charge pump output of the RFID IC. The charge pump in an RFID IC is described in Section 2.4. The capacitor increases the energy storage of the charge pump circuitry, thereby increasing the read range of the sensor. With the PCB layout completed, the PCB can then be integrated with the rest of the antenna designed previously. The completed design is shown modeled in Figure 7.1.

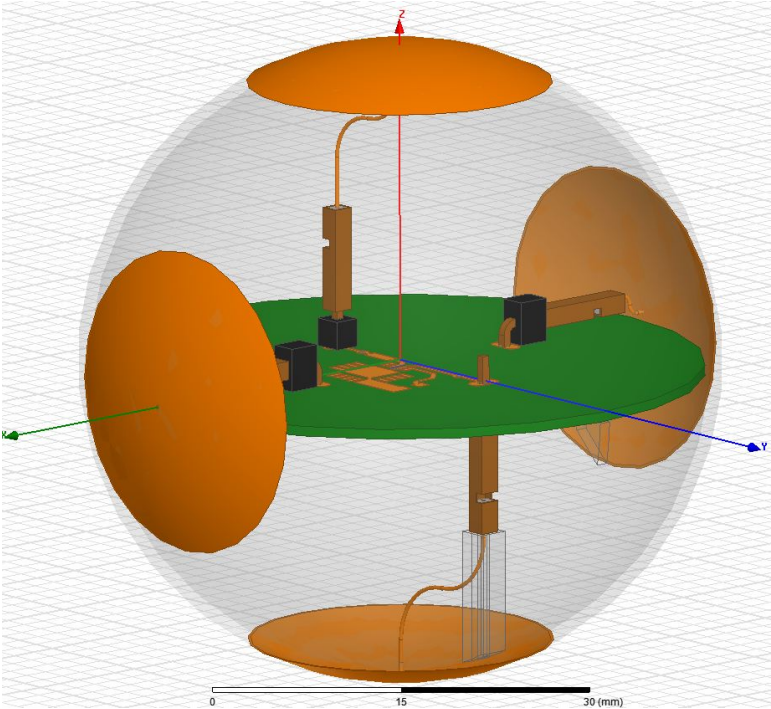


Figure 7.1. Model of the antenna and PCB used to test the wireless sensor utilizing the IDS RFID IC [55]. The IDS IC allows for temperature measurements internally and external control of additional sensor electronics.

### 7.3. IDS Wireless Sensor Simulation and Construction

The next step in completing the design is to simulate the performance of the antenna. Through simulation, modifications to the tuning elements of the antenna are made. For the antenna design used, the size of the spherical-caps and the value of the discrete matching component are what tune the antenna. In simulation, the spherical-cap size is controlled by varying the variable  $h$ , as shown in Figure 5.1. Because the antenna must have an inductive or positive value for the reactive portion of its impedance, a series inductor is again used for a tuning element. As described in Section 5.3, the characteristic impedance of the antenna traces on the PCB need to be known in order to correctly account for the actual impedance of the inductor seen at the port. The same method of simulating the PCB using ADS and extracting the characteristic impedance was used. Through this method, it was found that the antenna traces of the new design have a characteristic impedance of  $167.8 \Omega$ . Using this value, the antenna was tuned for the IDS IC at 915 MHz. The dimensions used for this design as well as the resulting performance criteria are specified in Table 7.1 and Figure 7.2. The Higgs 3 reference refers to the antenna design shown in Figure 5.8, since it uses the Higgs 3 RFID IC.

Table 7.1. Dimensional, bandwidth, and operating frequency comparison between the antenna design utilizing the Higgs 3 IC and the IDS IC.

<b>Antenna</b>	<b><math>f_0</math> (MHz)</b>	<b>Bandwidth (MHz)</b>	<b><math>h</math> (mm)</b>	<b>Inductor (nH)</b>
Higgs 3	920	55.5	3.4	33
IDS	905	15.1	3.0	33

Compared to the Higgs 3 design (see Table 7.1), the IDS design uses a smaller spherical-cap but still uses the same inductor value. While similar in dimensions, the

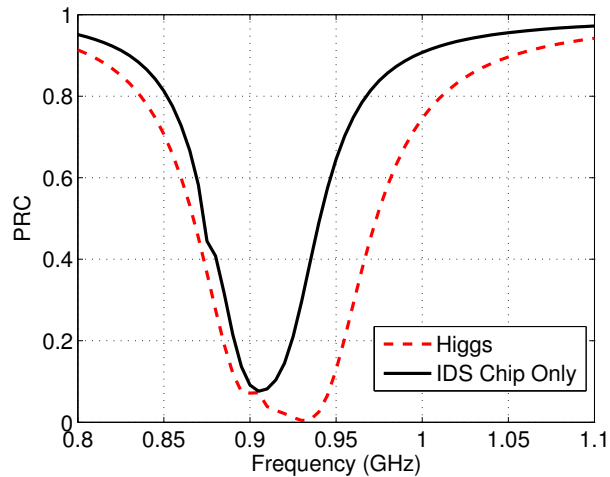


Figure 7.2. PRC comparison between the antenna design for the Higgs 3 IC and the design for the IDS IC.

IDS design has an operating frequency that is lower than the optimum 915 MHz and bandwidth that is markedly reduced. This occurs for various reasons. A cause for the lower operating frequency is a non-optimum value of the series inductor. While a value adjusted slightly lower in inductance resulted in better performance, the discrete values available meant that 30 nH was the next lowest value available. This caused the resonance point to be too high in frequency for the RFID frequency allocation available in the United States. A cause for the reduction in bandwidth is a less effective use of the antenna volume. Because of the smaller spherical-caps, the antenna has a smaller effective aperture which causes a higher Q value and less bandwidth [42], [47]. While an optimum value for the spherical-cap could have been obtained for a preferred operating frequency of 915 MHz, the available inductor sizes and manufacturing tolerances available negated the benefit of further optimization. The effects of having a lower operating frequency and smaller bandwidth in comparison to the antenna design for the Higgs 3 is shown graphically in Figure 7.2.



Besides performance over frequency of the sensor antenna, the radiation pattern is the other important metric. Figure 7.3 displays the simulated electric field intensity at 915 MHz. As with the previous antenna utilizing the Higgs 3 IC, the field intensity plots in each principal plane show a near-isotropic radiation pattern. Table 7.2 compares the gain metrics for the Higgs 3 antenna, derived in Section 5.3, with the antenna design for the IDS IC. From the table, the IDS tag design exhibits a higher MEG in addition to having a smaller range in gains. This points to the conclusion that the IDS antenna will exhibit more of an isotropic radiation pattern than the antenna design for the Higgs 3 IC.

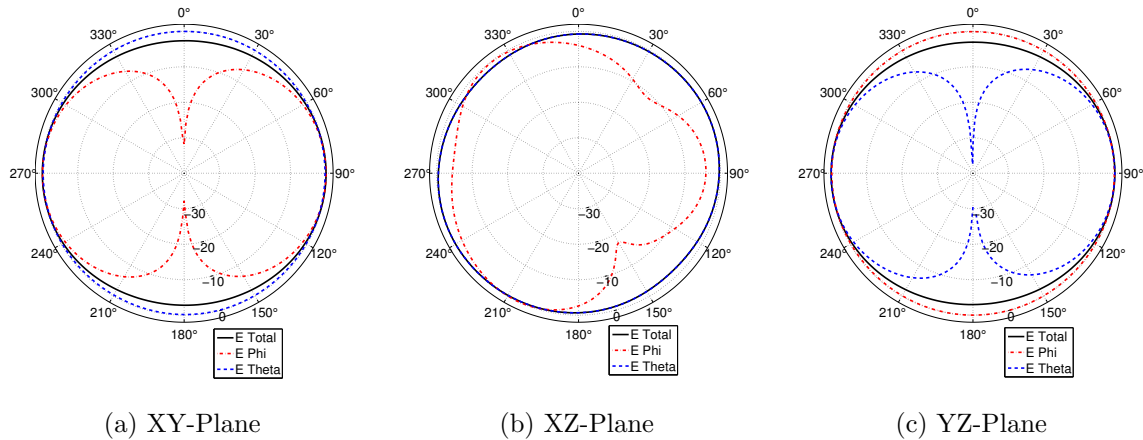


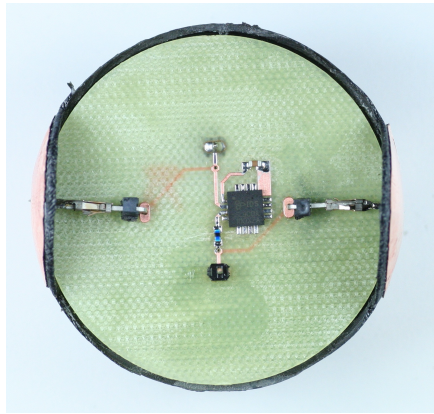
Figure 7.3. Simulated, normalized, electric field intensity patterns for the IDS IC antenna design. The plots are from simulation results.

With an antenna design proven through simulation, the design was then manufactured. A similar process as detailed in Section 6.1 was used. Photographs of the PCB used are shown in Figure 7.4. Figure 7.4a shows the overall outline of the PCB design while Figure 7.4b shows a close-up view of the IDS IC and the charge pump

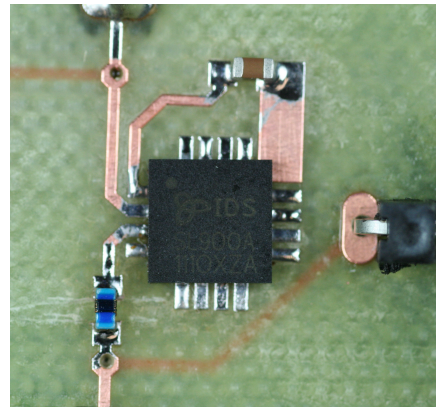
Table 7.2. Gain comparison between the Higgs 3 antenna design and the IDS design.

Antenna	MEG (dBi)	Max Gain (dBi)	Min Gain (dBi)
Higgs 3	-0.45	1.81	-8.07
IDS	-0.21	1.61	-2.45

capacitor included. The capacitor has a value of 2.2  $\mu\text{F}$ . The blue discrete component shown near the bottom left of the figure is the series inductor used for impedance matching.



(a) IDS PCB design.



(b) Close-up showing the altered antenna traces, charge pump capacitor (top, brown) and IDS IC.

Figure 7.4. PCB design used for the IDS IC based wireless sensor antenna.

#### 7.4. IDS Wireless Sensor Testing and Results

The constructed antenna was tested in a manner similar to that outlined in Section 6.2. Figure 7.5 displays the maximum read ranges measured in each principal plane. Maximum read range is defined by Equation 6.1. The jagged pattern evident in Figure 7.5c near 60 degrees and 150 degrees results from the tag interrogation error in

the USRP test setup described in Section 6.4. Overall, the patterns are near-isotropic without any significant nulls present. Over all three principal planes, the maximum read range varies between a maximum value of 2.73 meters in the XY-plane and a minimum of 0.24 meters in the XZ-plane.

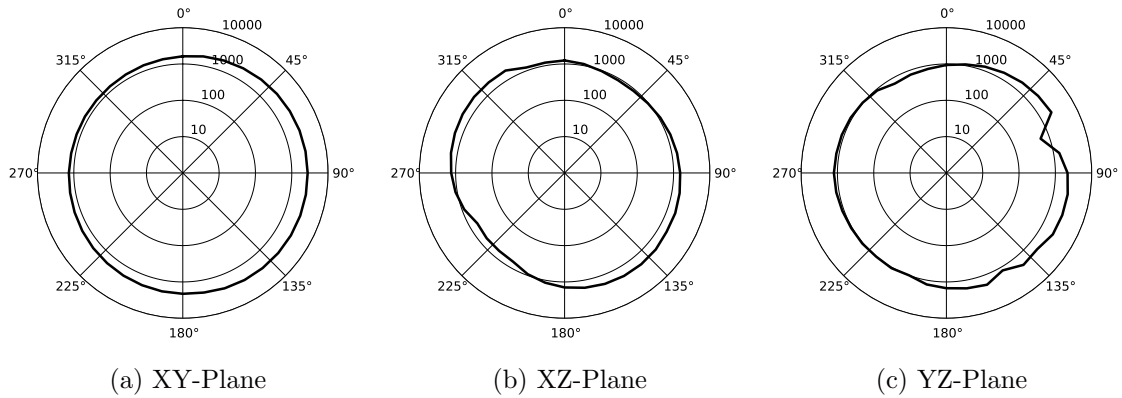


Figure 7.5. Relative radiation pattern measurements given as maximum read distance calculated using Equation 6.1. The units are in mm.

Figures 7.6 and 7.7 compare the simulated performance of the antenna to the measured results. The validity of these comparisons is derived in Section 6.3. The simulated results (see Figure 7.6) correctly predicted the operating frequency of the antenna but underestimated the bandwidth available. A potential explanation for this phenomenon is the use of the parallel RC circuit to model the input impedance of the IDS IC. The RC model suggested a faster roll-off than the actual device exhibited. This deviation is caused by the non-linear effects of the UHF RFID IC evident across different frequencies and input powers. Additionally, the effect of adding the charge pump capacitor was not known and therefore not modeled. From these results, it is

valid to conclude that the IDS IC with a charge pump capacitor operates at a frequency as predicted but with a decreased bandwidth.

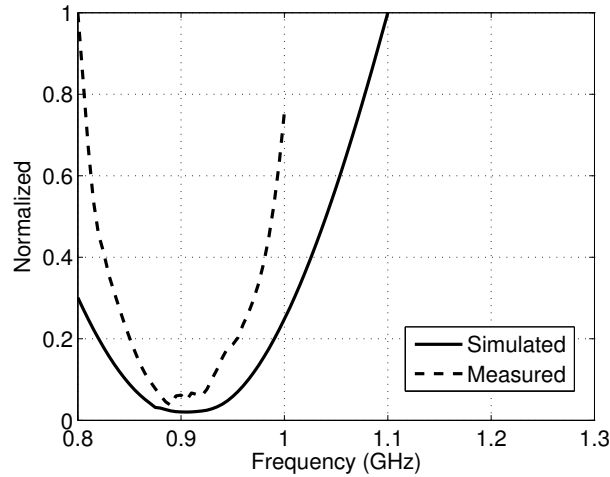


Figure 7.6. Normalized plot, comparing the simulated PRC for the IDS IC antenna to the measured minimum turn-on power.

The near-isotropic performance as predicted by simulation is exhibited by the measured results (see Figure 7.7). There do exist some discrepancies, evident in all three principal planes. These likely result from manufacturing tolerances and the simulation not taking into account the effects of the electronic packages (IDS IC and discrete components). Besides the measurement error in Figure 7.7c, the measured results correlate well with simulation.

Because the antenna design is similar to the design used with the Higgs 3 RFID IC, the radiation patterns should be similar. Figure 7.8 displays a comparison between the two antenna designs. As predicted, the radiation patterns correlate well between the two designs in all three principal planes. Differences result from the separate PCB designs and different supporting electronics required for each RFID IC. Viewing

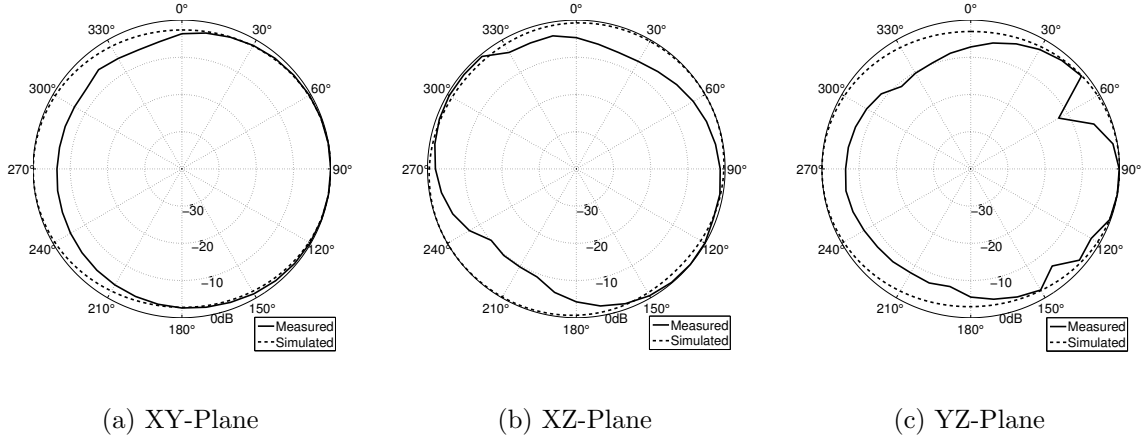


Figure 7.7. Normalized radiation pattern comparison between the simulated total electric field intensity and the minimum read range plot shown in Figure 6.7 at 915 MHz.

Figures 7.4 and 6.5, the differences in the PCB layout between the two designs can be seen. From a visual analysis of Figure 7.8, the IDS design performs as well to marginally better in each principal plane. This confirms the simulated results shown in Table 7.2.

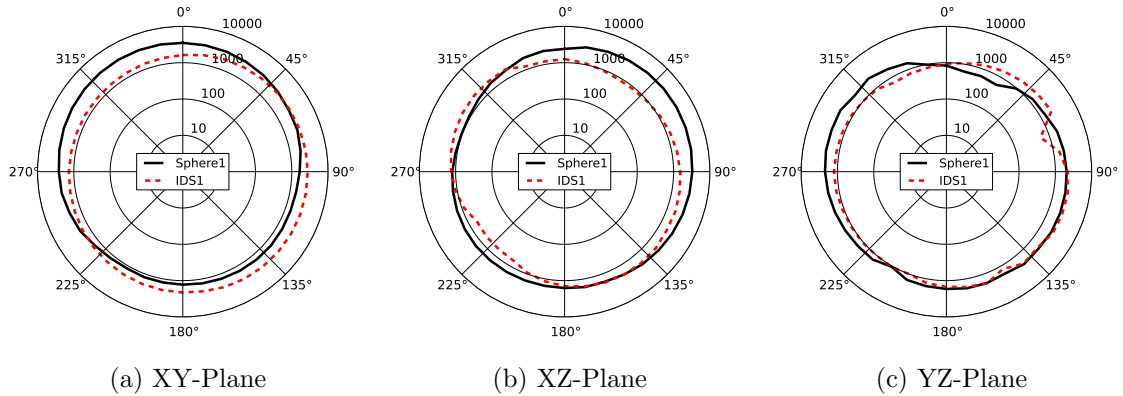


Figure 7.8. Comparison between the measured maximum read range for the Higgs 3 antenna design (Sphere1) and the IDS antenna design (IDS1) at 915 MHz.

## CHAPTER 8. CONCLUSIONS

The final antenna design shown in Figure 7.1 is the culmination of all the research completed for this work. As stated in Section 1.4, the goal for this research was to develop a wireless sensor suitable for deployment where orientation is uncontrolled. This situation would occur if the wireless sensor was deployed from a UAV. The results provided in both Chapters 6 and 7 demonstrate the ability of the antenna to operate in any orientation. Besides a tolerance to orientation, the sensor also needed to provide internal volume for sensor electronics. The wireless sensor platform created provides internal volume for sensor electronics as well as a simple method for integrating the electronics with the antenna design. The internal PCB, shown in Figure 7.4a, provides a simple method for integrating electronics with the sensor platform. In addition to an electronics platform, the PCB also offers a simple method for constructing the antenna. The PCB allows the sensor to be assembled and disassembled in a stepped process, as displayed by Figures 6.3, 6.4 and 6.5.

Besides the construction and electrical performance of the sensor, it also needed to be small and rugged enough for deployment into an uncontrolled environment. The size of the sensor is small, on the threshold of being electrically small, with a diameter of 52.1 mm. For perspective, this is 12.1 mm larger in radius than a typical table tennis ball. With its small size and spherical shape, the sensor is easy to pack and deploy. A UAV should be able to deploy the sensor in large numbers without difficulty. The sensor itself is also rugged. The shell is made out of ABS plastic and all of the electronic components are housed inside this shell. If the sensor itself was coated with a type of conformal coating, it could easily be made to withstand the harsh environmental conditions found outdoors around the world.

As mentioned previously, the antenna performance allows the sensor to be used in any orientation. Typically, the read range for the sensor was in excess of one

meter for effective radiated powers from the measurement antenna at or below legal limits in the United States. However, only having a meter of read range may prove challenging for a UAV to interrogate the wireless sensor. Future research should focus on studying the capabilities needed to read a sensor from a UAV. If the current capabilities are not adequate, a directional antenna design should be researched. In order to circumvent the uncontrolled orientation issue resulting from an uncontrolled deployment, the sensor could be asymmetrically weighted. This would ensure that the sensor would land in an orientation suitable for the directional radiation pattern of the antenna. The directional radiation pattern would increase the gain in a certain direction, thereby causing the maximum read range to also increase.

Additional research should also focus on determining energy storage methods suitable for the sensor, weather proofing methods and their effectiveness, and the effects of objects near the sensor on the performance of the antenna. Energy storage methods, such as a super-capacitor or a battery, add the capability for extended read range and constant sensing capabilities, even when not being interrogated. However, a super-capacitor and a battery add cost to the inexpensive sensor, and in the case of a battery, introduce a consumable to the design. Weatherproofing is another consideration before the sensor is used. The type of weatherproofing needed, its effectiveness, and its effect on the antenna will determine the usage range for the sensor. Lastly, the loading of the antenna by objects near the sensor will determine the actual performance seen when the sensor is fielded. These include dielectric loading from ground effects and the attenuation caused by plants and other liquid filled materials. The change in performance may affect whether the sensor can be deployed in certain areas, whether a battery is needed for increased range, and/or the antenna needs to use a design more resilient to these factors.

Overall, the research completed in this work fulfilled the goals set for it. Both antenna designs shown in Chapter 6 and 7 were both easy and inexpensive to produce, fulfilling the first goal set in Section 5.1. Both antennas also satisfied the second goal by exhibiting a near-isotropic radiation pattern. For the third goal, both antenna designs again fulfilled it by operating in the UHF RFID spectrum in the United States. The fourth goal was finally met by the antenna design of Chapter 7. This antenna contained the IDS UHF RFID IC, which allows the antenna design to measure and log temperature, as well as easily interface with other sensor electronics. This allows the antenna design to serve as a functioning wireless sensor. The last goal specifying that the antenna needed to be ruggedized for the harsh conditions during deployment and long-term use was satisfied by the antenna designs in both Chapters 6 and 7. The ABS shell gave the antenna a rigid structure as well as protected the internal sensing electronics. In addition to the goals, the simulated performance accurately predicted the real-world performance of the manufactured prototype antennas. With these goals met and the validation of the design process, the antenna meets the overarching objective of creating a wireless sensor for deployment by a UAV. This wireless sensor platform will help expand the ability to collect data autonomously.



## REFERENCES

- [1] M. Korda, *With Wings Like Eagles : The Untold Story of the Battle of Britain*. New York: Harper Perennial, 2010.
- [2] D. Dobkin, *The RF in RFID: Passive UHF RFID in Practice*, ser. Communications Engineering Series. Elsevier / Newnes, 2008.
- [3] J. Khan, R. Katz, and K. Pister, “Emerging challenges: Mobile networking for “smart dust”,” *Journal of Communications and Networks*, vol. 2, no. 3, pp. 188–196, 2000.
- [4] M. Buettner, B. Greenstein, A. Sample, J. Smith, and D. Wetherall, “Revisiting smart dust with RFID sensor networks,” in *Proceedings of the 7th ACM Workshop on Hot Topics in Networks (HotNets-VII)*, 2008.
- [5] M. Philipose, J. Smith, B. Jiang, A. Mamishev, S. Roy, and K. Sundara-Rajan, “Battery-free wireless identification and sensing,” *Pervasive Computing, IEEE*, vol. 4, no. 1, pp. 37–45, 2005.
- [6] N. Cho, S. Song, S. Kim, S. Kim, and H. Yoo, “A 5.1- $\mu$ w UHF RFID tag chip integrated with sensors for wireless environmental monitoring,” in *Solid-State Circuits Conference, 2005. ESSCIRC 2005. Proceedings of the 31st European. IEEE*, 2005, pp. 279–282.
- [7] I. Klotz. (2012, February) The skies open up for drones. Discovery News. [Online]. Available: <http://news.discovery.com/tech/drones-sky-122302.html>
- [8] C. Balanis, *Advanced Engineering Electromagnetics*, 2nd ed. Wiley, 2012.
- [9] W. Hayt and J. Buck, *Engineering Electromagnetics*, 7th ed., ser. McGraw-Hill series in electrical engineering. McGraw-Hill Higher Education, 2006.

- [10] D. Pozar, *Microwave Engineering*, 3rd ed. Wiley, 2005.
- [11] C. Balanis, *Antenna Theory: Analysis and Design*, 3rd ed. John Wiley & Sons, 2005.
- [12] S. Mess-Elektronik. (2007, May) UHA 9125 D, Half - Wave Dipole, 1.0 4 GHz. [Online]. Available: [http://en.wikipedia.org/wiki/File:Half\\_%E2%80%9393\\_Wave\\_Dipole.jpg](http://en.wikipedia.org/wiki/File:Half_%E2%80%9393_Wave_Dipole.jpg)
- [13] (2006, August) HWDipoleGain. [Online]. Available: <http://commons.wikimedia.org/wiki/File:HWDipoleGain.svg>
- [14] S. Mess-Elektronik. (2007, May) Broadband microwave horn antenna. [Online]. Available: [http://en.wikipedia.org/wiki/File:Schwarzbeck\\_BBHA\\_9120\\_D.jpg](http://en.wikipedia.org/wiki/File:Schwarzbeck_BBHA_9120_D.jpg)
- [15] Agilent Technologies. Pyramidal horn. [Online]. Available: <http://edocs.soco.agilent.com/display/empro2009/Pyramidal+Horn>
- [16] L. Frenzel. (2012, March) Back to basics: Impedance matching (part 2). [Online]. Available: <http://electronicdesign.com/communications/back-basics-impedance-matching-part-2>
- [17] ——. (2012, March) Back to basics: Impedance matching (part 3). [Online]. Available: <http://electronicdesign.com/communications/back-basics-impedance-matching-part-3>
- [18] (2011) Single stub mat. [Online]. Available: [http://www.arcticpeak.com/antennapages/single\\_stub\\_match.html](http://www.arcticpeak.com/antennapages/single_stub_match.html)
- [19] Quarter wave transformer matching. [Online]. Available: [http://examcrazy.com/Engineering/Electronics-Communication/Quarter-Wave\\_Transformer\\_Matching.asp](http://examcrazy.com/Engineering/Electronics-Communication/Quarter-Wave_Transformer_Matching.asp)

- [20] G. Marrocco, “The art of UHF RFID antenna design: impedance-matching and size-reduction techniques,” *Antennas and Propagation Magazine, IEEE*, vol. 50, no. 1, pp. 66–79, 2008.
- [21] M. Buettner and D. Wetherall, “A software radio-based UHF RFID reader for PHY / MAC experimentation,” in *IEEE International Conference on RFID*. Orlando, FL: IEEE, 2011, pp. 198–205.
- [22] L. Ni, Y. Liu, Y. Lau, and A. Patil, “LANDMARC: Indoor location sensing using active RFID,” *Wireless networks*, vol. 10, no. 6, pp. 701–710, 2004.
- [23] Z. Li, C. Chu, and W. Yao, “SIP-RLTS: An RFID location tracking system based on SIP,” in *RFID, 2008 IEEE International Conference on*. IEEE, 2008, pp. 173–182.
- [24] M. Buettner, R. Prasad, M. Philipose, and D. Wetherall, “Recognizing daily activities with RFID-based sensors,” in *Proceedings of the 11th international conference on Ubiquitous computing*. ACM, 2009, pp. 51–60.
- [25] S. Roy, V. Jandhyala, J. Smith, D. Wetherall, B. Otis, R. Chakraborty, M. Buettner, D. Yeager, Y. Ko, and A. Sample, “RFID: From supply chains to sensor nets,” *Proceedings of the IEEE*, vol. 98, no. 9, pp. 1583–1592, 2010.
- [26] F. Hu, S. Kumar, and Y. Xiao, “Towards a secure, RFID/sensor based telecardiology system,” in *Proceedings of the 4th Annual IEEE Consumer Communications and Networking Conference (CCNC07)*, 2007, pp. 732–736.
- [27] R. Bhattacharyya, C. Di Leo, C. Floerkemeier, S. Sarma, and L. Anand, “RFID tag antenna based temperature sensing using shape memory polymer actuation,” in *Sensors, 2010 IEEE*. IEEE, 2010, pp. 2363–2368.

- [28] S. Caizzone, C. Occhiuzzi, and G. Marrocco, "Multi-chip RFID antenna integrating shape-memory alloys for detection of thermal thresholds," *Antennas and Propagation, IEEE Transactions on*, vol. 59, no. 7, pp. 2488–2494, 2011.
- [29] R. Bhattacharyya, C. Floerkemeier, S. Sarma, and D. Deavours, "RFID tag antenna based temperature sensing in the frequency domain," in *RFID (RFID), 2011 IEEE International Conference on*. IEEE, 2011, pp. 70–77.
- [30] Y. Ikemoto, S. Suzuki, H. Okamoto, H. Murakami, H. Asama, S. Morishita, T. Mishima, X. Lin, and H. Itoh, "Force sensor system for structural health monitoring using passive RFID tags," *Sensor Review*, vol. 29, no. 2, pp. 127–136, 2009.
- [31] C. Occhiuzzi, C. Paggi, and G. Marrocco, "Passive RFID strain-sensor based on meander-line antennas," *Antennas and Propagation, IEEE Transactions on*, vol. 59, no. 12, pp. 4836–4840, 2011.
- [32] X. Yi, T. Wu, Y. Wang, R. Leon, M. Tentzeris, and G. Lantz, "Passive wireless smart-skin sensor using RFID-based folded patch antennas," *International Journal of Smart and Nano Materials*, vol. 2, no. 1, pp. 22–38, 2011.
- [33] R. Bhattacharyya, C. Floerkemeier, and S. Sarma, "Towards tag antenna based sensing-an RFID displacement sensor," in *RFID, 2009 IEEE International Conference on*. IEEE, 2009, pp. 95–102.
- [34] C. Occhiuzzi, A. Rida, G. Marrocco, and M. Tentzeris, "Passive ammonia sensor: RFID tag integrating carbon nanotubes," in *Antennas and Propagation (APSURSI), 2011 IEEE International Symposium on*. IEEE, 2011, pp. 1413–1416.

- [35] J. Lynch and K. Loh, "A summary review of wireless sensors and sensor networks for structural health monitoring," *Shock and Vibration Digest*, vol. 38, no. 2, pp. 91–130, 2006.
- [36] C. Kruesi, R. Vyas, and M. Tentzeris, "Design and development of a novel 3-D cubic antenna for wireless sensor networks (WSNs) and RFID applications," *Antennas and Propagation, IEEE Transactions on*, vol. 57, no. 10, pp. 3293–3299, 2009.
- [37] I. Nassar and T. Weller, "Development of novel 3-D cube antennas for compact wireless sensor nodes," *Antennas and Propagation, IEEE Transactions on*, no. 99, pp. 1–1, 2012.
- [38] D. Kholodnyak, P. Turalchuk, A. Mikhailov, S. Dudnikov, and I. Vendik, "3D antenna for UHF RFID tags with eliminated read-orientation sensitivity," in *Microwave Conference, 2006. 36th European. Ieee*, 2006, pp. 583–586.
- [39] C. Medeiros, J. Costa, and C. Fernandes, "Passive UHF RFID tag for airport suitcase tracking and identification," *Antennas and Wireless Propagation Letters, IEEE*, vol. 10, pp. 123–126, 2011.
- [40] H. Ryu, G. Jung, D. Ju, S. Lim, and J. Woo, "An electrically small spherical UHF RFID tag antenna with quasi-isotropic patterns for wireless sensor networks," *Antennas and Wireless Propagation Letters, IEEE*, vol. 9, pp. 60–62, 2010.
- [41] G. Jung, H. Ryu, S. Lim, and J. Woo, "Design of a spherical-shaped, UHF RFID tag antenna with 3-axes polarization," in *Antennas and Propagation Society International Symposium, 2009. APSURSI'09. IEEE. IEEE*, 2009, pp. 1–4.

- [42] S. Best, “Low Q electrically small linear and elliptical polarized spherical dipole antennas,” *Antennas and Propagation, IEEE Transactions on*, vol. 53, no. 3, pp. 1047–1053, 2005.
- [43] ANSYS. (2012) Hfss 13. [Online]. Available: <http://www.ansys.com/Products/Simulation+Technology/Electromagnetics/High-Performance+Electronic+Design/ANSYS+HFSS>
- [44] M. Sadiku, *Numerical Techniques in Electromagnetics With Matlab*, 3rd ed. CRC Press INC, 2009.
- [45] (2012, January) Higgs 3 EPC Class 1 Gen 2 RFID tag IC. [Online]. Available: <http://www.alientechnology.com/docs/products/Alien-Technology-Higgs-3-ALC-360.pdf>
- [46] T. Bird, “Definition and misuse of return loss [report of the transactions editor-in-chief],” *Antennas and Propagation Magazine, IEEE*, vol. 51, no. 2, pp. 166–167, 2009.
- [47] S. Best and D. Hanna, “A performance comparison of fundamental small-antenna designs,” *Antennas and Propagation Magazine, IEEE*, vol. 52, no. 1, pp. 47–70, 2010.
- [48] H. Wheeler, “Antenna topics in my experience,” *Antennas and Propagation, IEEE Transactions on*, vol. 33, no. 2, pp. 144 – 151, feb 1985.
- [49] P. Nikitin, K. Rao, S. Lam, V. Pillai, R. Martinez, and H. Heinrich, “Power reflection coefficient analysis for complex impedances in RFID tag design,” *Microwave Theory and Techniques, IEEE Transactions on*, vol. 53, no. 9, pp. 2721 – 2725, sept. 2005.

- [50] G. Pan, Y. Li, Z. Zhang, and Z. Feng, “Isotropic radiation from a compact planar antenna using two crossed dipoles,” *Antennas and Wireless Propagation Letters, IEEE*, vol. 11, pp. 1338–1341, 2012.
- [51] (2011) Advanced Design System. Agilent.
- [52] J. Nielsen and G. Pedersen, “Mobile handset performance evaluation using radiation pattern measurements,” *Antennas and Propagation, IEEE Transactions on*, vol. 54, no. 7, pp. 2154–2165, 2006.
- [53] *Test Plan for Mobile Station Over the Air Performance*, CTIA Certification Std., Rev. 2.2.2, December 2008.
- [54] K. Rao, P. Nikitin, and S. Lam, “Antenna design for UHF RFID tags: A review and a practical application,” *Antennas and Propagation, IEEE Transactions on*, vol. 53, no. 12, pp. 3870–3876, 2005.
- [55] S1900a. [Online]. Available: <http://www.ids-microchip.com/sl900a.php>
- [56] (2012) Impinj Monza X chips. [Online]. Available: [http://www.impinj.com/support/downloadable\\_documents.aspx#Monza%20X%20Chips](http://www.impinj.com/support/downloadable_documents.aspx#Monza%20X%20Chips)

## APPENDIX A. MATLAB CODE

This appendix contains all of the Matlab code used in analyzing data and creating the figures used in this work.

### A.1. Simulated Data Plotting

```
1  % Thesis plotting
   % This program makes the relevant plots used in the thesis work
   %Layne Berge February 27th, 2013
   clear; clc; close all;

5
   % Set plotting for typical rectangular plots
   set(0,'DefaultAxesColorOrder',[0 0 0], ...
       'DefaultAxesFontSize', 14, ...
       'DefaultTextFontSize', 14, ...
10      'DefaultLineLineWidth',2);

   % File directories used
   fileDir = 'D:\Documents\Research\Thesis\Results\None Skewed\VSWR\';
   fileDirOne = 'D:\Documents\Research\Thesis\Results\One Skewed\';
15  fileDirBoth = 'D:\Documents\Research\Thesis\Results\Both Skewed\';
   fileDirPrev = 'D:\Documents\Research\Thesis\Results\PreviousDesign\';
   fileName = 'hatheight_3p4_VSWR.csv';
   fileNameXY = 'XY-Circular-H-0.csv';
   fileNameYZ = 'YZ-Circular-H-110.csv';
20  fileNamePRCNone = 'PRC_3p4_33nH.csv';
   fileNamePRCOne = 'PRC_3p4_33nH.csv';
   fileNamePRCBoth = 'PRC_3p0_37nH.csv';
   fileNamePrev = 'PreviousDesign_Thin_PRC.csv';
   fileNamePrevRL = 'PreviousDesign_Thin_negRL.csv';

25
   % Read in initial data
   data = csvread([fileDir,fileName],1,0);
   dataPRC = csvread([fileDir,fileNamePRCNone],1,0);
   dataXYmeas = csvread([fileDir,fileNameXY],5,0);
30  dataYZmeas = csvread([fileDir,fileNameYZ],5,0);
   dataPrev = csvread([fileDirPrev,fileNamePrev],1,0);
   dataPrevRL = csvread([fileDirPrev,fileNamePrevRL],1,0);

   % Plot VSWR of None Skewed Double Dipole Antenna
35  figure(1)
   f = data(:,1);
   vswr = data(:,2);
   plot(f,vswr,'-k');
   xlabel('Frequency (GHz)');
40  ylabel('VSWR');
   title('VSWR');
   grid on;
   axis([0.8 1.1 0 70]);
```



```

45 % Plot E-field of None Skewed Double Dipole
fileDir2 = 'D:\Documents\Research\Thesis\Results\None Skewed\ ...
Polar E Plots\';
fileName2 = 'E_XY_3p4.csv';
fileName3 = 'E_XZ_3p4.csv';
50 fileName4 = 'E_YZ_3p4.csv';

dataXY = csvread([fileDir2,fileName2],1,0);
dataXZ = csvread([fileDir2,fileName3],1,0);
dataYZ = csvread([fileDir2,fileName4],1,0);
55
XYang = dataXY(:,1);
XYtotal = dataXY(:,2);
XYphi = dataXY(:,3);
XYtheta = dataXY(:,4);
60
XZang = dataXZ(:,1);
XZtotal = dataXZ(:,2);
XZphi = dataXZ(:,3);
XZtheta = dataXZ(:,4);
65
YZang = dataYZ(:,1);
YZtotal = dataYZ(:,2);
YZphi = dataYZ(:,3);
YZtheta = dataYZ(:,4);
70
set(0,'DefaultAxesColorOrder',[0 0 0], ...
'DefaultAxesFontSize', 24, ...
'DefaultTextFontSize', 24, ...
'DefaultLineLineWidth',3);
75
figure(2)
mmpolar(XYang.*pi/180,XYtotal,'-k'); hold on;
mmpolar(XYang.*pi/180,XYphi,'-.r');
mmpolar(XYang.*pi/180,XYtheta,'--b','style','compass',...
80 'RLimit',[-40,0],'RTickUnits','dB','TTickDelta',30,...
'TTickSign','+', 'RTickAngle',165);
legend('E Total','E Phi','E Theta');
% title('E Field Normalized XY Plane');

85 figure(3)
mmpolar(XZang.*pi/180,XZtotal,'-k'); hold on;
mmpolar(XZang.*pi/180,XZphi,'-.r');
mmpolar(XZang.*pi/180,XZtheta,'--b','style','compass',...
90 'RLimit',[-40,0],'RTickUnits','dB','TTickDelta',30,...
'TTickSign','+', 'RTickAngle',165);
legend('E Total','E Phi','E Theta');
% title('E Field Normalized XZ Plane');

95 figure(4)
mmpolar(YZang.*pi/180,YZtotal,'-k'); hold on;

```

```

mmpolar(YZang.*pi/180,YZphi,'-.r');
mmpolar(YZang.*pi/180,YZtheta,'--b','style','compass',...
'RLimit',[-40,0],'RTickUnits','dB','TTickDelta',30,...
'TTickSign','+', 'RTickAngle',165);
100 legend('E Total','E Phi','E Theta');
% title('E Field Normalized YZ Plane');

% Plot comparison of three double dipole designs
set(0,'DefaultAxesColorOrder',[0 0 0], ...
105 'DefaultAxesFontSize', 14, ...
'DefaultTextFontSize', 14, ...
'DefaultLineLineWidth',2);

figure(5)
110 measf = dataXYmeas(:,1);
measFR = dataXYmeas(:,2);
index = find(measFR > 10);
measFR(index) = [];
measfr = measf;
115 measfr(index) = [];
measFRi = interp1(measfr,measFR,measf);

measf2 = dataYZmeas(:,1);
measFR2 = dataYZmeas(:,2);
120 index2 = find((diff(measFR2) > 2).*...
(diff(measFR2)<5)) + 1;
measFR2(index2) = [];
measf2r = measf2;
measf2r(index2) = [];
125 measFR2i = interp1(measf2r,measFR2,measf2);

fPRC = dataPRC(:,1);
PRC = dataPRC(:,2);

130 measFRi = 10.^(measFRi./10);
measFR2i = 10.^(measFR2i./10);
plot(measf./1e3,measFRi./(10^(12/10)),'-k'); hold on;
plot(measf2./1e3,measFR2i./(10^(12/10)),'--k');
vswr = vswr.^2;
135 plot(f,vswr./max(vswr),'-r');
plot(fPRC,PRC,'-g');
xlabel('Frequency (GHz)');
ylabel('VSWR');
%title('VSWR');
140 grid on;
axis([0.8 1.0 0 1.0]);

% Plot PRC for double dipole none skewed
figure(6)
145 plot(fPRC,PRC,'-k');
xlabel('Frequency (GHz)');
ylabel('PRC');

```

```

title('Power Reflection Coefficient (PRC)');
grid on;
150 axis([0.8 1.1 0 1.0]);

f10dB = find((PRC<=0.1).*(PRC>0));
f10dB = f(f10dB);
BW = max(f10dB) - min(f10dB);
155 f0 = (max(f10dB) + min(f10dB))/2;
disp(['BW = ',num2str(BW),' GHz and f0 = ',num2str(f0),' GHz']);

% PRC comparison between the three double dipole designs
figure(7)
160 dataPRCNone = csvread([fileDir,fileNamePRCNone],1,0);
dataPRCOne = csvread([fileDirOne,fileNamePRCOne],1,0);
dataPRCBoth = csvread([fileDirBoth,fileNamePRCBoth],1,0);

fPRCNone = dataPRCNone(:,1);
165 fPRCOne = dataPRCOne(:,1);
fPRCBoth = dataPRCBoth(:,1);

PRCNone = dataPRCNone(:,2);
PRCOne = dataPRCOne(:,2);
170 PRCBoth = dataPRCBoth(:,2);

plot(fPRCNone,PRCNone,'-k'); hold on;
plot(fPRCOne,PRCOne,'--r');
plot(fPRCBoth,PRCBoth,'-.b');
175 xlabel('Frequency (GHz)');
ylabel('PRC');
% title('Power Reflection Coefficient (PRC)');
grid on;
axis([0.8 1.1 0 1.0]);
180 legend('None Skewed','One Skewed','Both Skewed');

% PRC for previous spherical design (IV Bag design)
figure(8)
fPRCPrev = dataPrev(:,1);
185 PRCPrev = dataPrev(:,2);
plot(fPRCPrev,PRCPrev,'-k');
xlabel('Frequency (MHz)');
ylabel('PRC');
grid on;
190 axis([870 970 0 1.0]);

% -Return loss for previous spherical design (IV Bag design)
figure(9)
fPRCPrevRL = dataPrevRL(:,1);
195 PRCPrevRL = dataPrevRL(:,2);
plot(fPRCPrevRL,PRCPrevRL,'-k');
xlabel('Frequency (MHz)');
ylabel('-Return Loss');
grid on;

```

```

200 axis([870 970 -4 0]);

%%%%%%%%%%%%%%%%%%%%%%%%%%%%%%%%%%%%%%%%%%%%%%%%%%%%%%%%%%%%%%%%%%%%%%%%%%%%%%
%%%%%%%%%%%%%%%%%%%%%%%%%%%%%%%%%%%%%%%%%%%%%%%%%%%%%%%%%%%%%%%%%%%%%%%%%%%%%% Single Dipole Spherical Cap %%%%%%%%%%%%%%%
%%%%%%%%%%%%%%%%%%%%%%%%%%%%%%%%%%%%%%%%%%%%%%%%%%%%%%%%%%%%%%%%%%%%%%%%%%%%%%
205 %%
set(0,'DefaultAxesColorOrder',[0 0 0], ...
    'DefaultAxesFontSize', 14, ...
    'DefaultTextFontSize', 14, ...
    'DefaultLineLineWidth',2);

210 % 6mm Cap Height
fileDir = 'D:\Documents\Research\Thesis\Results\SingleDipole\';
fileName = 'SingleDipole_PRC_6mmHat_1p05GHz-f0_36p2MHz-BW.csv';
dataPRC6mm = csvread([fileDir,fileName],1,0);
215 fileName = 'SingleDipole_ReZ_6mmHat_1p05GHz-f0_36p2MHz-BW.csv';
dataReZ6mm = csvread([fileDir,fileName],1,0);
fileName = 'SingleDipole_ImZ_6mmHat_1p05GHz-f0_36p2MHz-BW.csv';
dataImZ6mm = csvread([fileDir,fileName],1,0);

220 % 15mm Cap Height
fileDir = 'D:\Documents\Research\Thesis\Results\SingleDipole\';
fileName = 'SingleDipole_PRC_15mmHat_10MHz-f0_0MHz-BW.csv';
dataPRC15mm = csvread([fileDir,fileName],1,0);
225 fileName = 'SingleDipole_ReZ_15mmHat_10MHz-f0_0MHz-BW.csv';
dataReZ15mm = csvread([fileDir,fileName],1,0);
fileName = 'SingleDipole_ImZ_15mmHat_10MHz-f0_0MHz-BW.csv';
dataImZ15mm = csvread([fileDir,fileName],1,0);

% PRC plot
230 figure(10)
i=11;
f = dataPRC6mm(:,1);
PRC = dataPRC6mm(:,2);
PRC15 = dataPRC15mm(:,2);
235 plot(f,PRC,'-k',f,PRC15,'--k');
legend('6 mm','15 mm');
xlabel('Frequency (GHz)');
ylabel('PRC');
grid on;
240 axis([0.8 1.1 0 1]);

% Impedance plot 6mm
figure(11)
245 f = dataReZ6mm(:,1);
ReZ = dataReZ6mm(:,2);
f = dataImZ6mm(:,1);
ImZ = dataImZ6mm(:,2);
plot(f,ReZ,'-k',f,ImZ,'--k');
legend('Re{Z}','Im{Z}');
250 xlabel('Frequency (GHz)');
ylabel('Impedance \Omega');

```

```

grid on;
axis([0.8 1.1 0 210]);

255 % Impedance plot 15mm
figure(12)
f = dataReZ15mm(:,1);
ReZ = dataReZ15mm(:,2);
f = dataImZ15mm(:,1);
260 ImZ = dataImZ15mm(:,2);
plot(f,ReZ,'-k',f,ImZ,'--k');
legend('Re{Z}','Im{Z}');
xlabel('Frequency (GHz)');
ylabel('Impedance \Omega');
265 grid on;
axis([0.8 1.1 0 300]);

% E-field Plot 6 mm
fileDir = 'D:\Documents\Research\Thesis\Results\SingleDipole\';
270 fileNameXY = 'SingleDipole_E-XY_6mmHat.csv';
fileNameXZ = 'SingleDipole_E-XZ_6mmHat.csv';
fileNameYZ = 'SingleDipole_E-YZ_6mmHat.csv';
dataXY = csvread([fileDir,fileNameXY],1,0);
dataXZ = csvread([fileDir,fileNameXZ],1,0);
275 dataYZ = csvread([fileDir,fileNameYZ],1,0);

XYang = dataXY(:,1);
XYtotal = dataXY(:,2);
XYphi = dataXY(:,3);
280 XYtheta = dataXY(:,4);

XZang = dataXZ(:,1);
XZtotal = dataXZ(:,2);
XZphi = dataXZ(:,3);
285 XZtheta = dataXZ(:,4);

YZang = dataYZ(:,1);
YZtotal = dataYZ(:,2);
YZphi = dataYZ(:,3);
290 YZtheta = dataYZ(:,4);

set(0,'DefaultAxesColorOrder',[0 0 0], ...
'DefaultAxesFontSize', 24, ...
'DefaultTextFontSize', 24, ...
295 'DefaultLineLineWidth',3);

figure(13)
mmpolar(XYang.*pi/180,XYtotal,'-k'); hold on;
mmpolar(XYang.*pi/180,XYphi,'-.r');
300 mmpolar(XYang.*pi/180,XYtheta,'--b','style','compass',...
'RLimit',[-40,0],'RTickUnits','dB','TTickDelta',30,...
'TTickSign','+', 'RTickAngle',165);
legend('E Total','E Phi','E Theta');

```

```

305 % title('E Field Normalized XY Plane');

figure(14)
mmpolar(XZang.*pi/180,XZtotal,'-k'); hold on;
mmpolar(XZang.*pi/180,XZphi,'-.r');
mmpolar(XZang.*pi/180,XZtheta,'--b','style','compass',...
310 'RLimit',[-40,0],'RTickUnits','dB','TTickDelta',30,...
'TTickSign','+', 'RTickAngle',165);
legend('E Total','E Phi','E Theta');
% title('E Field Normalized XZ Plane');

315 figure(15)
mmpolar(YZang.*pi/180,YZtotal,'-k'); hold on;
mmpolar(YZang.*pi/180,YZphi,'-.r');
mmpolar(YZang.*pi/180,YZtheta,'--b','style','compass',...
320 'RLimit',[-40,0],'RTickUnits','dB','TTickDelta',30,...
'TTickSign','+', 'RTickAngle',165);
legend('E Total','E Phi','E Theta');
% title('E Field Normalized YZ Plane');

% E-field Plot 15 mm
325 fileDir = 'D:\Documents\Research\Thesis\Results\...
SingleDipole\';
fileNameXY = 'SingleDipole_E-XY_15mmHat.csv';
fileNameXZ = 'SingleDipole_E-XZ_15mmHat.csv';
fileNameYZ = 'SingleDipole_E-YZ_15mmHat.csv';
330 dataXY = csvread([fileDir,fileNameXY],1,0);
dataXZ = csvread([fileDir,fileNameXZ],1,0);
dataYZ = csvread([fileDir,fileNameYZ],1,0);

XYang = dataXY(:,1);
335 XYtotal = dataXY(:,2);
XYphi = dataXY(:,3);
XYtheta = dataXY(:,4);

XZang = dataXZ(:,1);
340 XZtotal = dataXZ(:,2);
XZphi = dataXZ(:,3);
XZtheta = dataXZ(:,4);

YZang = dataYZ(:,1);
345 YZtotal = dataYZ(:,2);
YZphi = dataYZ(:,3);
YZtheta = dataYZ(:,4);

set(0,'DefaultAxesColorOrder',[0 0 0], ...
350 'DefaultAxesFontSize', 24, ...
'DefaultTextFontSize', 24, ...
'DefaultLineLineWidth',3);

figure(16)
355 mmpolar(XYang.*pi/180,XYtotal,'-k'); hold on;

```

```

mmpolar(XYang.*pi/180,XYphi,'-.r');
mmpolar(XYang.*pi/180,XYtheta,'--b','style','compass',...
'RLimit',[-40,0],'RTickUnits','dB','TTickDelta',30,...
'TTickSign','+', 'RTickAngle',165);
360 legend('E Total','E Phi','E Theta');
% title('E Field Normalized XY Plane');

figure(17)
mmpolar(XZang.*pi/180,XZtotal,'-k'); hold on;
365 mmpolar(XZang.*pi/180,XZphi,'-.r');
mmpolar(XZang.*pi/180,XZtheta,'--b','style','compass',...
'RLimit',[-40,0],'RTickUnits','dB','TTickDelta',30,...
'TTickSign','+', 'RTickAngle',165);
legend('E Total','E Phi','E Theta');
370 % title('E Field Normalized XZ Plane');

figure(18)
mmpolar(YZang.*pi/180,YZtotal,'-k'); hold on;
mmpolar(YZang.*pi/180,YZphi,'-.r');
375 mmpolar(YZang.*pi/180,YZtheta,'--b','style','compass',...
'RLimit',[-40,0],'RTickUnits','dB','TTickDelta',30,...
'TTickSign','+', 'RTickAngle',165);
legend('E Total','E Phi','E Theta');
% title('E Field Normalized YZ Plane');
380

%%%%%%%%%%%%%%%%%%%%%%%%%%%%%%%%%%%%%%%%%%%%%%%%%%%%%%%%%%%%%%%%%%%%%%%%%%
%%%%%%%%%%%%%%%%%%%%%%%%%%%%%%%%%%%%%%%%%%%%%%%%%%%%%%%%%%%%%%%%%%%%%%%%%% Single Dipole Spiral Spherical Cap %%%%%%%%%
%%%%%%%%%%%%%%%%%%%%%%%%%%%%%%%%%%%%%%%%%%%%%%%%%%%%%%%%%%%%%%%%%%%%%%%%%%
385 set(0,'DefaultAxesColorOrder',[0 0 0], ...
'DefaultAxesFontSize', 14, ...
'DefaultTextFontSize', 14, ...
'DefaultLineStyle','solid','DefaultLineLineWidth',2);

390 fileDir = 'D:\Documents\Research\Thesis\Results\...
SingleDipole\';
fileName = 'SingleDipoleSpiral_PRC_3mmHat_2p6mm...
SpiralRadius_-910MHz-f0_21p8MHz-BW.csv';
dataPRCspiral = csvread([fileDir,fileName],1,0);
395 fileName = 'SingleDipoleSpiral_ReZ_3mmHat_2p6mm...
SpiralRadius_-910MHz-f0_21p8MHz-BW.csv';
dataReZspiral = csvread([fileDir,fileName],1,0);
fileName = 'SingleDipoleSpiral_ImZ_3mmHat_2p6mm...
SpiralRadius_-910MHz-f0_21p8MHz-BW.csv';
400 dataImZspiral = csvread([fileDir,fileName],1,0);

% Plot PRC
figure(19)
f = dataPRCspiral(:,1);
405 PRC = dataPRCspiral(:,2);
plot(f,PRC,'-k');
xlabel('Frequency (GHz)');

```

```

ylabel('PRC');
grid on;
410 axis([0.8 1.1 0 1]);

% Plot impedance
figure(20)
f = dataReZspiral(:,1);
415 ReZ = dataReZspiral(:,2);
f = dataImZspiral(:,1);
ImZ = dataImZspiral(:,2);
plot(f,ReZ,'-k',f,ImZ,'--k');
legend('Re{Z}','Im{Z}');
420 xlabel('Frequency (GHz)');
ylabel('Impedance \Omega');
grid on;
axis([0.8 1.1 0 500]);

425 % E-field Plot 3 mm Hat 2.6 mm radius
fileDir = 'D:\Documents\Research\Thesis\Results\SingleDipole\';
fileNameXY = 'SingleDipoleSpiral_E-XY_3mmHat_2p6mmSpiralRadius.csv';
fileNameXZ = 'SingleDipoleSpiral_E-XZ_3mmHat_2p6mmSpiralRadius.csv';
fileNameYZ = 'SingleDipoleSpiral_E-YZ_3mmHat_2p6mmSpiralRadius.csv';
430 dataXY = csvread([fileDir,fileNameXY],1,0);
dataXZ = csvread([fileDir,fileNameXZ],1,0);
dataYZ = csvread([fileDir,fileNameYZ],1,0);

XYang = dataXY(:,1);
435 XYtotal = dataXY(:,2);
XYphi = dataXY(:,3);
XYtheta = dataXY(:,4);

XZang = dataXZ(:,1);
440 XZtotal = dataXZ(:,2);
XZphi = dataXZ(:,3);
XZtheta = dataXZ(:,4);

YZang = dataYZ(:,1);
445 YZtotal = dataYZ(:,2);
YZphi = dataYZ(:,3);
YZtheta = dataYZ(:,4);

set(0,'DefaultAxesColorOrder',[0 0 0], ...
450 'DefaultAxesFontSize', 24, ...
'DefaultTextFontSize', 24, ...
'DefaultLineLineWidth',3);

figure(21)
455 mmpolar(XYang.*pi/180,XYtotal,'-k'); hold on;
mmpolar(XYang.*pi/180,XYphi,'-r');
mmpolar(XYang.*pi/180,XYtheta,'--b','style','compass',...
'RLimit',[-40,0],'RTickUnits','dB','TTickDelta',30,...
'TTickSign','+', 'RTickAngle',165);

```



```

460 legend('E Total','E Phi','E Theta');
% title('E Field Normalized XY Plane');

figure(22)
mmpolar(XZang.*pi/180,XZtotal,'-k'); hold on;
465 mmpolar(XZang.*pi/180,XZphi,'-r');
mmpolar(XZang.*pi/180,XZtheta,'--b','style','compass',...
'RLimit',[-40,0],'RTickUnits','dB','TTickDelta',30,...
'TTickSign','+', 'RTickAngle',165);
legend('E Total','E Phi','E Theta');
470 % title('E Field Normalized XZ Plane');

figure(23)
mmpolar(YZang.*pi/180,YZtotal,'-k'); hold on;
mmpolar(YZang.*pi/180,YZphi,'-r');
475 mmpolar(YZang.*pi/180,YZtheta,'--b','style','compass',...
'RLimit',[-40,0],'RTickUnits','dB','TTickDelta',30,...
'TTickSign','+', 'RTickAngle',165);
legend('E Total','E Phi','E Theta');
% title('E Field Normalized YZ Plane');

480 %%
%%%%%%%%%%%%%%%%%%%%%%%%%%%%%%%%%%%%%%%%%%%%%%%%%%%%%%%%%%%%%%%%%%%%%%%%
%%%%%%%%%%%%%%%%%%%%%%%%%%%%%%%%%%%%%%%%%%%%%%%%%%%%%%%%%%%%%%%%%%%%%%%%
%%%%%%%%%%%%%%%%%%%%%%%%%%%%%%%%%%%%%%%%%%%%%%%%%%%%%%%%%%%%%%%%%%%%%%%% Simulated to Measured Results Comparison %%%%%%%%%
%%%%%%%%%%%%%%%%%%%%%%%%%%%%%%%%%%%%%%%%%%%%%%%%%%%%%%%%%%%%%%%%%%%%%%%%
%%%%%%%%%%%%%%%%%%%%%%%%%%%%%%%%%%%%%%%%%%%%%%%%%%%%%%%%%%%%%%%%%%%%%%%%

485 set(0,'DefaultAxesColorOrder',[0 0 0], ...
'DefaultAxesFontSize', 14, ...
'DefaultTextFontSize', 14, ...
'DefaultLineLineWidth',2);

490 % Plot PRC
figure(24)
fileDir = 'D:\Documents\Research\Thesis\Results\None Skewed\VSWR\';
fileNamePRCNone = 'PRC_3p4_33nH.csv';
495 dataPRCNone = csvread([fileDir,fileNamePRCNone],1,0);
fPRCNone = dataPRCNone(:,1);
PRCNone = dataPRCNone(:,2);

% Compare and plot simulated PRC with measured max read range
500 fileDirMeas = 'D:\Documents\Research\Thesis\Testing\Sphere1\XY\';
fileNameMeas = 'XY-Circular-H-0.csv';
% fileNameMeas = 'Sphere2-XY-H-0.csv';
dataMeas = csvread([fileDirMeas,fileNameMeas],5,0);
dataMeas = PatternInterp(dataMeas,'diff',2);
505 fMeas = dataMeas(:,1);
PMeas = dataMeas(:,2);
PMeas = PMeas + 16; % Account for cable losses
PMeas = 10.^(PMeas./10);
PMeas = PMeas./max(PMeas);
510 minFreq = fMeas(find(PMeas == min(PMeas)));
disp(['Measured minimum frequency = ',num2str(minFreq),' MHz']);

```

```

PRCNoneComp = 1./((1-PRCNone).*(.3./fPRCNone).^2);
plot(fPRCNone,PRCNoneComp./max(PRCNoneComp),'-k'); hold on;
515 plot(fMeas./1e3,PMeas,'--k');
xlabel('Frequency (GHz)');
ylabel('Normalized');
grid on;
axis([0.8 1.1 0 1.0]);
520 legend('Simulated','Measured');

figure(25)
fileDir = 'D:\Documents\Research\Thesis\Results\None Skewed\VSWR\';
fileNamePRCNone = 'PRC_3p4_33nH.csv';
525 dataPRCNone = csvread([fileDir,fileNamePRCNone],1,0);
fPRCNone = dataPRCNone(:,1);
PRCNone = dataPRCNone(:,2);

% Compare simulated to measured results for all four measured
530 % antennas
fileDirMeas1 = 'D:\Documents\Research\Thesis\Testing\Sphere1\XY\';
fileNameMeas1 = 'XY-Circular-H-0.csv';
fileDirMeas2 = 'D:\Documents\Research\Thesis\Testing\Sphere2\XY\';
fileNameMeas2 = 'Sphere2-XY-H-0.csv';
535 fileDirMeas3 = 'D:\Documents\Research\Thesis\Testing\Sphere3\XY\';
fileNameMeas3 = 'Sphere3-XY-H-40.csv';
fileDirMeas4 = 'D:\Documents\Research\Thesis\Testing\Sphere4\XY\';
fileNameMeas4 = 'Sphere4-XY-H-0.csv';

540 dataMeas1 = csvread([fileDirMeas1,fileNameMeas1],5,0);
dataMeas1 = PatternInterp(dataMeas1,'diff',2);
fMeas1 = dataMeas1(:,1);
PMeas1 = dataMeas1(:,2);
PMeas1 = PMeas1 + 16; % Account for cable losses
545 PMeas1 = 10.^(PMeas1./10);
PMeas1 = PMeas1./max(PMeas1);
minFreq1 = fMeas(find(PMeas1 == min(PMeas1)));
disp(['Measured minimum frequency 1 = ',num2str(minFreq1),' MHz']);

550 dataMeas2 = csvread([fileDirMeas2,fileNameMeas2],5,0);
dataMeas2 = PatternInterp(dataMeas2,'diff',2);
fMeas2 = dataMeas2(:,1);
PMeas2 = dataMeas2(:,2);
PMeas2 = PMeas2 + 16; % Account for cable losses
555 PMeas2 = 10.^(PMeas2./10);
PMeas2 = PMeas2./max(PMeas2);
minFreq2 = fMeas(find(PMeas2 == min(PMeas2)));
disp(['Measured minimum frequency 2 = ',num2str(minFreq2),' MHz']);

560 dataMeas3 = csvread([fileDirMeas3,fileNameMeas3],5,0);
dataMeas3 = PatternInterp(dataMeas3,'diff',2);
fMeas3 = dataMeas3(:,1);
PMeas3 = dataMeas3(:,2);

```

```

PMeas3 = PMeas3 + 16; % Account for cable losses
565 PMeas3 = 10.^(PMeas3./10);
PMeas3 = PMeas3./max(PMeas3);
minFreq3 = fMeas(find(PMeas3 == min(PMeas3)));
disp(['Measured minimum frequency 3 = ',num2str(minFreq3),' MHz']);

570 dataMeas4 = csvread([fileDirMeas4,fileNameMeas4],5,0);
dataMeas4 = PatternInterp(dataMeas4,'diff',2);
fMeas4 = dataMeas4(:,1);
PMeas4 = dataMeas4(:,2);
PMeas4 = PMeas4 + 16; % Account for cable losses
575 PMeas4 = 10.^(PMeas4./10);
PMeas4 = PMeas4./max(PMeas4);
minFreq4 = fMeas(find(PMeas4 == min(PMeas4)));
disp(['Measured minimum frequency 4 = ',num2str(minFreq4),' MHz']);

580
plot(fPRCNone,PRCNoneComp./max(PRCNoneComp),'-k'); hold on;
plot(fMeas1./1e3,PMeas1,'--k');
plot(fMeas2./1e3,PMeas2,'-.r');
plot(fMeas3./1e3,PMeas3,':b');
585 plot(fMeas4./1e3,PMeas4,'-g');
xlabel('Frequency (GHz)');
ylabel('Normalized');
grid on;
axis([0.8 1.1 0 1.0]);
590 legend('Simulated','Sphere1','Sphere2','Sphere3','Sphere4');

%%
%%%%%%%%%%%%%%%%%%%%%%%%%%%%%%%%%%%%%%%%%%%%%%%%%%%%%%%%%%%%%%%%%%%%%%%%%%
%%%%%%%%%%%%%%%%%%%%%%%%%%%%%%%%%%%%%%%%%%%%%%%%%%%%%%%%%%%%%%%%%%%%%%%%%%
595 %%%%%%%%%%%%%%%%%%%%%%%%%%%%%%%%%%%%%%%%%%%%%%%%%%%%%%%%%%%%%%%%%%%%%%%%%%% IDS Chip Only %%%%%%%%%%%%%%%%%%%%%%%%%%%%%%%%%%%%%%%%%%%%%%%%%%%%%%%%%%%%%%%%%%%%%%%%%%%
%%%%%%%%%%%%%%%%%%%%%%%%%%%%%%%%%%%%%%%%%%%%%%%%%%%%%%%%%%%%%%%%%%%%%%%%%%

set(0,'DefaultAxesColorOrder',[0 0 0], ...
'DefaultAxesFontSize', 14, ...
'DefaultTextFontSize', 14, ...
600 'DefaultLineLineWidth',2);

% PRC Plot
fileDirHiggs = 'D:\Documents\Research\Thesis\Results\None Skewed\VSWR\';
fileNamePRCHiggs = 'PRC_3p4_33nH.csv';
605 dataPRCHiggs = csvread([fileDirHiggs,fileNamePRCHiggs],1,0);
fPRCHiggs = dataPRCHiggs(:,1);
PRCHiggs = dataPRCHiggs(:,2);

fileDirChipOnly = 'D:\Documents\Research\Thesis\Results\IDS\ChipOnly\';
610 fileNamePRCChipOnly = 'PRC_ChipOnly_3mm_33nH_905MHz_15p1MHz.csv';
dataPRCChipOnly = csvread([fileDirChipOnly,fileNamePRCChipOnly],1,0);
fPRCChipOnly = dataPRCChipOnly(:,1);
PRCChipOnly = dataPRCChipOnly(:,2);

615 figure(26)

```

```

plot(fPRCHiggs,PRCHiggs,'--r',fPRCChipOnly,PRCChipOnly,'-k');
xlabel('Frequency (GHz)');
ylabel('PRC');
grid on;
620 axis([0.8 1.1 0 1.0]);
legend('Higgs','IDS Chip Only');

% Simulated to measured comparison
figure(27)
625 fileDirMeas = 'D:\Documents\Research\Thesis\Testing\IDS1\XY\';
fileNameMeas = 'IDS1-XY-H-0.csv';
dataMeas = csvread([fileDirMeas,fileNameMeas],5,0);
dataMeas = PatternInterp(dataMeas,'hybrid',2);
fMeas = dataMeas(:,1);
630 PMeas = dataMeas(:,2);
PMeas = PMeas + 16; % Account for cable losses
PMeas = 10.^(PMeas./10);
PMeas = PMeas./max(PMeas);
minFreq = fMeas(find(PMeas == min(PMeas)));
635 disp(['Measured minimum frequency = ',num2str(minFreq),' MHz']);

PRCChipOnlyComp = 1./((1-PRCChipOnly).*(.3./fPRCChipOnly).^2);
plot(fPRCChipOnly,PRCChipOnlyComp./max(PRCChipOnlyComp),'-k'); hold on;
plot(fMeas./1e3,PMeas,'--k');
640 xlabel('Frequency (GHz)');
ylabel('Normalized');
grid on;
axis([0.8 1.1 0 1.0]);
legend('Simulated','Measured');
645

% E-field Plot
fileNameChipOnlyXY = 'E_XY_ChipOnly_3mm_33nH_905MHz_15p1MHz.csv';
fileNameChipOnlyXZ = 'E_XZ_ChipOnly_3mm_33nH_905MHz_15p1MHz.csv';
fileNameChipOnlyYZ = 'E_YZ_ChipOnly_3mm_33nH_905MHz_15p1MHz.csv';
650 ChipOnlyXY = csvread([fileDirChipOnly,fileNameChipOnlyXY],1,0);
ChipOnlyXZ = csvread([fileDirChipOnly,fileNameChipOnlyXZ],1,0);
ChipOnlyYZ = csvread([fileDirChipOnly,fileNameChipOnlyYZ],1,0);

ChipOnlyXYang = ChipOnlyXY(:,1);
655 ChipOnlyXYtotal = ChipOnlyXY(:,2);
ChipOnlyXYphi = ChipOnlyXY(:,3);
ChipOnlyXYtheta = ChipOnlyXY(:,4);

ChipOnlyXZang = ChipOnlyXZ(:,1);
660 ChipOnlyXZtotal = ChipOnlyXZ(:,2);
ChipOnlyXZphi = ChipOnlyXZ(:,3);
ChipOnlyXZtheta = ChipOnlyXZ(:,4);

ChipOnlyYZang = ChipOnlyYZ(:,1);
665 ChipOnlyYZtotal = ChipOnlyYZ(:,2);
ChipOnlyYZphi = ChipOnlyYZ(:,3);
ChipOnlyYZtheta = ChipOnlyYZ(:,4);

```

```

set(0,'DefaultAxesColorOrder',[0 0 0], ...
670     'DefaultAxesFontSize', 24, ...
        'DefaultTextFontSize', 24, ...
        'DefaultLineLineWidth',3);

figure(28)
675 mmpolar(ChipOnlyXYang.*pi/180,ChipOnlyXYtotal,'-k'); hold on;
mmpolar(ChipOnlyXYang.*pi/180,ChipOnlyXYphi,'-.r');
mmpolar(ChipOnlyXYang.*pi/180,ChipOnlyXYtheta,'--b','style','compass',...
        'RLimit',[-40,0],'RTickUnits','dB','TTickDelta',30,'TTickSign','+',...
        'RTickAngle',165);
680 legend('E Total','E Phi','E Theta');
% title('E Field Normalized XY Plane');

figure(29)
mmpolar(ChipOnlyXZang.*pi/180,ChipOnlyXZtotal,'-k'); hold on;
685 mmpolar(ChipOnlyXZang.*pi/180,ChipOnlyXZphi,'-.r');
mmpolar(ChipOnlyXZang.*pi/180,ChipOnlyXZtheta,'--b','style','compass',...
        'RLimit',[-40,0],'RTickUnits','dB','TTickDelta',30,'TTickSign','+',...
        'RTickAngle',165);
legend('E Total','E Phi','E Theta');
690 % title('E Field Normalized XY Plane');

figure(30)
mmpolar(ChipOnlyYZang.*pi/180,ChipOnlyYZtotal,'-k'); hold on;
mmpolar(ChipOnlyYZang.*pi/180,ChipOnlyYZphi,'-.r');
695 mmpolar(ChipOnlyYZang.*pi/180,ChipOnlyYZtheta,'--b','style','compass',...
        'RLimit',[-40,0],'RTickUnits','dB','TTickDelta',30,'TTickSign',...
        '+','RTickAngle',165);
legend('E Total','E Phi','E Theta');
% title('E Field Normalized XY Plane');
700

%%
%%%%%%%%%%%%%%%%%%%%%%%%%%%%%%%%%%%%%%%%%%%%%%%%%%%%%%%%%%%%%%%%%%%%%%%%%%
%%%%%%%%%%%%%%%%%%%%%%%%%%%%%%%%%%%%%%%%%%%%%%%%%%%%%%%%%%%%%%%%%%%%%%%%%%
%%%%%%%%%%%%%%%%%%%%%%%%%%%%%%%%%%%%%%%%%%%%%%%%%%%%%%%%%%%%%%%%%%%%%%%%%%
%%%%%%%%%%%%%%%%%%%%%%%%%%%%%%%%%%%%%%%%%%%%%%%%%%%%%%%%%%%%%%%%%%%%%%%%%%
705
set(0,'DefaultAxesColorOrder',[0 0 0], ...
        'DefaultAxesFontSize', 14, ...
        'DefaultTextFontSize', 14, ...
        'DefaultLineLineWidth',2);
710

% PRC Plot
fileDirHiggs = 'D:\Documents\Research\Thesis\Results\None Skewed\VSWR\';
fileNamePRCHiggs = 'PRC_3p4_33nH.csv';
dataPRCHiggs = csvread([fileDirHiggs,fileNamePRCHiggs],1,0);
715 fPRCHiggs = dataPRCHiggs(:,1);
PRCHiggs = dataPRCHiggs(:,2);

fileDirChipOnly = 'D:\Documents\Research\Thesis\Results\IDS\ChipOnly\';
fileNamePRCChipOnly = 'PRC_ChipOnly_3mm_33nH_905MHz_15p1MHz.csv';

```

```

720 dataPRCChipOnly = csvread([fileDirChipOnly,fileNamePRCChipOnly],1,0);
    fPRCChipOnly = dataPRCChipOnly(:,1);
    PRCChipOnly = dataPRCChipOnly(:,2);

    fileDirIDSElec = 'D:\Documents\Research\Thesis\Results\IDS\Electronics\';
725 fileNamePRCIDSElec = 'PRC_Electronics_2p6mm_910MHz_12MHz_36nH.csv';
    dataPRCIDSElec = csvread([fileDirIDSElec,fileNamePRCIDSElec],1,0);
    fPRCIDSElec = dataPRCIDSElec(:,1);
    PRCIDSElec = dataPRCIDSElec(:,2);

730 % Simulated to measured comparison
    figure(31)
    plot(fPRCHiggs,PRCHiggs,'--r',fPRCChipOnly,PRCChipOnly,'--g',...
        fPRCIDSElec,PRCIDSElec,'-k');
    xlabel('Frequency (GHz)');
735 ylabel('PRC');
    grid on;
    axis([0.8 1.1 0 1.0]);
    legend('Higgs','IDS Chip Only','IDS Electronics');

740 % E-field Plot
    fileNameIDSElecXY = 'E_XY_Electronics_2p6mm_910MHz_12MHz_36nH.csv';
    fileNameIDSElecXZ = 'E_XZ_Electronics_2p6mm_910MHz_12MHz_36nH.csv';
    fileNameIDSElecYZ = 'E_YZ_Electronics_2p6mm_910MHz_12MHz_36nH.csv';
    IDSElecXY = csvread([fileDirIDSElec,fileNameIDSElecXY],1,0);
745 IDSElecXZ = csvread([fileDirIDSElec,fileNameIDSElecXZ],1,0);
    IDSElecYZ = csvread([fileDirIDSElec,fileNameIDSElecYZ],1,0);

    IDSElecXYang = IDSElecXY(:,1);
    IDSElecXYtotal = IDSElecXY(:,2);
750 IDSElecXYphi = IDSElecXY(:,3);
    IDSElecXYtheta = IDSElecXY(:,4);

    IDSElecXZang = IDSElecXZ(:,1);
    IDSElecXZtotal = IDSElecXZ(:,2);
755 IDSElecXZphi = IDSElecXZ(:,3);
    IDSElecXZtheta = IDSElecXZ(:,4);

    IDSElecYZang = IDSElecYZ(:,1);
    IDSElecYZtotal = IDSElecYZ(:,2);
760 IDSElecYZphi = IDSElecYZ(:,3);
    IDSElecYZtheta = IDSElecYZ(:,4);

    set(0,'DefaultAxesColorOrder',[0 0 0], ...
        'DefaultAxesFontSize', 24, ...
765 'DefaultTextFontSize', 24, ...
        'DefaultLineLineWidth',3);

    figure(32)
    mmpolar(IDSElecXYang.*pi/180,IDSElecXYtotal,'-k'); hold on;
770 mmpolar(IDSElecXYang.*pi/180,IDSElecXYphi,'-.r');
    mmpolar(IDSElecXYang.*pi/180,IDSElecXYtheta,'--b','style','compass',...

```

```

    'RLimit',[-40,0], 'RTickUnits','dB', 'TTickDelta',30, 'TTickSign','+',...
    'RTickAngle',165);
    legend('E Total','E Phi','E Theta');
775 % title('E Field Normalized XY Plane');

    figure(33)
    mmpolar(IDSElecXZang.*pi/180,IDSElecXZtotal,'-k'); hold on;
    mmpolar(IDSElecXZang.*pi/180,IDSElecXZphi,'-.r');
780 mmpolar(IDSElecXZang.*pi/180,IDSElecXZtheta,'--b','style','compass',...
    'RLimit',[-40,0], 'RTickUnits','dB', 'TTickDelta',30, 'TTickSign','+',...
    '+','RTickAngle',165);
    legend('E Total','E Phi','E Theta');
    % title('E Field Normalized XY Plane');
785

    figure(34)
    mmpolar(IDSElecYZang.*pi/180,IDSElecYZtotal,'-k'); hold on;
    mmpolar(IDSElecYZang.*pi/180,IDSElecYZphi,'-.r');
    mmpolar(IDSElecYZang.*pi/180,IDSElecYZtheta,'--b','style','compass',...
790 'RLimit',[-40,0], 'RTickUnits','dB', 'TTickDelta',30, 'TTickSign','+',...
    '+','RTickAngle',165);
    legend('E Total','E Phi','E Theta');
    % title('E Field Normalized XY Plane');

```

## A.2. Simulated to Measured Radiation Pattern Comparison

```

1 % This script is used for comparing simulated E-field and measured maximum
  % read range data. The data is manipulated in order to allow for a valid
  % comparison. This script plot a comparison of the antenna, frequency and
  % plane specified in the User Variables. Must change simulated plane
5 % choice manually at end of script (XY, XZ, YZ).
  %Layne Berge January 11th, 2013
  clear; clc; close all;

  % User Variables
10 EIRP = 4.0; % in watts
   TX_GAIN = 4.0; % linear
   DIST = 0.47; % in meters
   freq = 915; % in MHz
   antenna = 'Sphere1';
15 plane = 'XY';
   angleStart = 0; % in degrees
   angleStep = 10;
   angleStop = 350;
   fileType = '.csv';
20 thresh = 2;

  % File Locations
   fileDirMeas = ['D:\Documents\Research\Thesis\Testing\' ,antenna,...
   '\',plane,'\'];
25 fileDirOutput = ['D:\Documents\Research\Thesis\Testing\Interpolated\' ,...
   antenna,'\',plane,'\'];

```

```

fileDirHFSS = 'D:\Documents\Research\Thesis\Results\None Skewed\...
Polar E Plots\';
% fileDirHFSS = 'D:\Documents\Research\Thesis\Results\IDS\ChipOnly\';
30 % fileDirHFSS = 'D:\Documents\Research\Thesis\Results\IDS\Electronics\';
fileNameHFSS_XY = 'E_XY_3p4.csv';
fileNameHFSS_XZ = 'E_XZ_3p4.csv';
fileNameHFSS_YZ = 'E_YZ_3p4.csv';
% fileNameHFSS_XY = 'E_XY_ChipOnly_3mm_33nH_905MHz_15p1MHz.csv';
35 % fileNameHFSS_XZ = 'E_XZ_ChipOnly_3mm_33nH_905MHz_15p1MHz.csv';
% fileNameHFSS_YZ = 'E_YZ_ChipOnly_3mm_33nH_905MHz_15p1MHz.csv';
% fileNameHFSS_XY = 'E_XY_Electronics_2p6mm_910MHz_12MHz_36nH.csv';
% fileNameHFSS_XZ = 'E_XZ_Electronics_2p6mm_910MHz_12MHz_36nH.csv';
% fileNameHFSS_YZ = 'E_YZ_Electronics_2p6mm_910MHz_12MHz_36nH.csv';
40
% Is the antenna shifted (degrees) or the rotation direction need to be
% changed
shift = 0;
flip = false;
45
% Read Data
Pmin = [];
PminInterp = [];
for angle = angleStart:angleStep:angleStop
50   fileNameMeas = ['XY', '-Circular-H-', num2str(angle), fileType];
%   fileNameMeas = [antenna, '-', plane, '-H-', num2str(angle), fileType];
   dataMeas = csvread([fileDirMeas, fileNameMeas], 5, 0);
   % Interpolate
   dataMeasInterp = PatternInterp(dataMeas, 'hybrid', thresh);
55   % Store interpolated and non-interpolated data
   Pmin = horzcat(Pmin, dataMeas(:, 2));
   PminInterp = horzcat(PminInterp, dataMeasInterp(:, 2));
end
% Parse simulated data
60 dataHFSS_XY = csvread([fileDirHFSS, fileNameHFSS_XY], 1, 0);
dataHFSS_XZ = csvread([fileDirHFSS, fileNameHFSS_XZ], 1, 0);
dataHFSS_YZ = csvread([fileDirHFSS, fileNameHFSS_YZ], 1, 0);

% Parse Data
65 f = dataMeas(:, 1);
fIndex = find(f == freq);
PminFreq = Pmin(fIndex, :);
PminInterpFreq = PminInterp(fIndex, :);
angle = angleStart:angleStep:angleStop+angleStep;
70 angle = angle';

% Shift measured data (both non-interpolated and interpolated data)
shiftIndex = find(angle == shift);
PminFreq = vertcat(PminFreq(shiftIndex:end), PminFreq(1:shiftIndex-1));
75 PminInterpFreq = vertcat(PminInterpFreq(shiftIndex:end), ...
PminInterpFreq(1:shiftIndex-1));
if flip
    PminFreq = flipdim(PminFreq, 1);

```



```

    PminInterpFreq = flipdim(PminInterpFreq,1);
80 end
    PminFreq = vertcat(PminFreq,PminFreq(1));
    % Needs points at 0 and 360 degrees to plot
    PminInterpFreq = vertcat(PminInterpFreq,PminInterpFreq(1));
    % Needs points at 0 and 360 degrees
85
    % Manipulate data for comparison
    PminFreq = PminFreq + 16; % Compensate for system losses
    PminFreq = 10.^(PminFreq./10); % convert to linear
    PminFreq = PminFreq./1000; % Convert from mW to W
90 rPminFreq = DIST*sqrt(EIRP./(PminFreq.*TX_GAIN));
    rPminFreq = rPminFreq./max(rPminFreq); % normalize
    rPminFreq = 20.*log10(rPminFreq); % Convert to dB

    PminInterpFreq = PminInterpFreq + 16; % Compensate for system losses
95 PminInterpFreq = 10.^(PminInterpFreq./10); % convert to linear
    PminInterpFreq = PminInterpFreq./1000; % Convert from mW to W
    PminInterpFreq = 10.^(PminInterpFreq./10); % convert to linear
    rPminInterpFreq = DIST*sqrt(EIRP./(PminInterpFreq.*TX_GAIN));
    disp(['Max distance = ',num2str(max(rPminInterpFreq)),...
100 ' m Min distance = ',num2str(min(rPminInterpFreq)), ' m']);
    rPminInterpFreq = rPminInterpFreq./max(rPminInterpFreq); % normalize
    rPminInterpFreq = 20.*log10(rPminInterpFreq); % Convert to dB

    % Parse simulated data
105 XYangHFSS = dataHFSS_XY(:,1);
    XYtotalHFSS = dataHFSS_XY(:,2);
    XYtotalHFSS = 10.^(XYtotalHFSS./20); % Convert to linear
    XYtotalHFSS = XYtotalHFSS./max(XYtotalHFSS); % Normalize
    XYtotalHFSS = 20.*log10(XYtotalHFSS); % Convert to dB
110
    XZangHFSS = dataHFSS_XZ(:,1);
    XZtotalHFSS = dataHFSS_XZ(:,2);
    XZtotalHFSS = 10.^(XZtotalHFSS./20); % Convert to linear
    XZtotalHFSS = XZtotalHFSS./max(XZtotalHFSS); % Normalize
115 XZtotalHFSS = 20.*log10(XZtotalHFSS); % Convert to dB

    YZangHFSS = dataHFSS_YZ(:,1);
    YZtotalHFSS = dataHFSS_YZ(:,2);
    YZtotalHFSS = 10.^(YZtotalHFSS./20); % Convert to linear
120 YZtotalHFSS = YZtotalHFSS./max(YZtotalHFSS); % Normalize
    YZtotalHFSS = 20.*log10(YZtotalHFSS); % Convert to dB

    % Plot Data
    set(0,'DefaultAxesColorOrder',[0 0 0], ...
125     'DefaultAxesFontSize', 24, ...
     'DefaultTextFontSize', 24, ...
     'DefaultLineLineWidth',3);
    % Plot non-interpolated and interpolated measured data
    figure(1)
130 mmpolar(angle.*pi/180,PminFreq,'-r');hold on;

```

```

mmpolar(angle.*pi/180,PminInterpFreq,'--b','style',...
'compass','RLimit',[-40,20],'RTickUnits','dB',...
'TTickDelta',30,'TTickSign','+');
legend('Raw','Interp');
135
% Plot comparison between measured and simulated data.
% Must change simulated plane manually!!!!!!
figure(2)
mmpolar(angle.*pi/180,rPminInterpFreq,'-k'); hold on;
140 mmpolar(XYangHFSS.*pi/180,XYtotalHFSS,'--k','style','compass',...
'RLimit',[-40,0],'RTickAngle',165,'RTickUnits','dB',...
'TTickDelta',30,'TTickSign','+');
legend('Measured','Simulated');

145

```

### A.3. Pattern Interpolation

```

1 function interpData = PatternInterp(data,str,thresh)
%Provided a matrix of data containing frequency in column 1 and response
%data in column 2, this function finds drop-outs, removes them and
%interpolates through them. The USRP system causes drop-outs which read as
5 %20.0 or large 'spikes'.
%Layne Berge February 10th, 2013

% Point based interpolation
% If a point defined by thresh is found, it is removed and interpolated
10 % through
if strcmp(str,'point')
f = data(:,1);
P = data(:,2);
rIndex = find(P == thresh); %Find drop-outs and store index location(s)
15 data(rIndex,:) = []; % Delete offending row of data
interpP = interp1(data(:,1),data(:,2),f,'cubic');
interpData = [f,interpP];
end

20 % Difference base interpolation
% If two points change an amount greater than thresh, the point is removed
% and interpolated through
if strcmp(str,'diff')
f = data(:,1);
25 P = data(:,2);
dP = diff(P);
rIndex = find((abs(dP) > thresh)|(dP == 0));
if length(rIndex) > 0
rIndex(1) = [];
30 % first index from diff threshold is good (are others?)
data(rIndex,:) = [];
end
interpP = interp1(data(:,1),data(:,2),f,'cubic');

```

```

    interpData = [f,interpP];
35 end

% A combination of point based and difference based interpolation
if strcmp(str,'hybrid')
    f = data(:,1);
40    P = data(:,2);

    rIndex = find(P == 20); % Find drop-outs and store index location(s)
    data(rIndex,:) = []; % Delete offending row of data
    P = interp1(data(:,1),data(:,2),f,'cubic');
45    data = horzcat(f,P);

    f = data(:,1);
    P = data(:,2);
    dP = diff(P);
50    rIndex = find((abs(dP) > thresh)|(dP == 0));
    if length(rIndex) > 0
        rIndex(1) = [];
        % first index from diff threshold is good (are others?)
        data(rIndex,:) = [];
55    end
    interpP = interp1(data(:,1),data(:,2),f,'cubic');
    interpData = [f,interpP];
end

```

#### A.4. MEG and Gain Calculations

```

1 % Gain Analysis
% This script analyzes the 3D gain pattern of an antenna given in .csv
% format. It reports the MEG, minimum gain, and maximum gain.
%Layne Berge November 20th, 2012
5 clear; close all; clc;

% File Paths
filePath = 'D:\HFSS\Thesis\OutputData\Stub Matching Smith\';
filePathNone = 'D:\Documents\Research\Thesis\Results\...
10 None Skewed\Polar E Plots\';
filePathOne = 'D:\Documents\Research\Thesis\Results\One Skewed\';
filePathBoth = 'D:\Documents\Research\Thesis\Results\Both Skewed\';

% Typical block format for each antenna
15 fileName = 'Gain_3p4.csv';
% Calls function to parse and report gain data
[G3davg,G3dmin,G3dmax] = G3dinfo([filePathNone,fileName]);
disp('None Skewed');
disp(['MEG gain = ',num2str(G3davg),'db, Gain min = ',...
20 num2str(G3dmin),'db, Gain max = ',num2str(G3dmax),'db']);
disp(' ');

fileName = 'Gain_3p4.csv';

```

```

[G3davg,G3dmin,G3dmax] = G3dinfo([filePathOne,fileName]);
25 disp('One Skewed');
disp(['MEG gain = ',num2str(G3davg),'db, Gain min = ',...
num2str(G3dmin),'db, Gain max = ',num2str(G3dmax),'db']);
disp(' ');

30 fileName = 'Gain_3p0.csv';
[G3davg,G3dmin,G3dmax] = G3dinfo([filePathBoth,fileName]);
disp('Both Skewed');
disp(['MEG gain = ',num2str(G3davg),'db, Gain min = ',...
num2str(G3dmin),'db, Gain max = ',num2str(G3dmax),'db']);
35 disp(' ');

filePath = 'D:\Documents\Research\Thesis\Results\SingleDipole\';
fileName = 'SingleDipole_Gain3D_6mmHat.csv';
[G3davg,G3dmin,G3dmax] = G3dinfo([filePath,fileName]);
40 disp(fileName);
disp(['MEG gain = ',num2str(G3davg),'db, Gain min = ',...
num2str(G3dmin),'db, Gain max = ',num2str(G3dmax),'db']);
disp(' ');

45 filePath = 'D:\Documents\Research\Thesis\Results\SingleDipole\';
fileName = 'SingleDipole_Gain3D_15mmHat.csv';
[G3davg,G3dmin,G3dmax] = G3dinfo([filePath,fileName]);
disp(fileName);
disp(['MEG gain = ',num2str(G3davg),'db, Gain min = ',...
50 num2str(G3dmin),'db, Gain max = ',num2str(G3dmax),'db']);
disp(' ');

filePath = 'D:\Documents\Research\Thesis\Results\SingleDipole\';
fileNam = 'SingleDipoleSpiral_Gain3D_3mmHat_2p6mmSpiralRadius.csv';
55 [G3davg,G3dmin,G3dmax] = G3dinfo([filePath,fileName]);
disp(fileName);
disp(['MEG gain = ',num2str(G3davg),'db, Gain min = ',...
num2str(G3dmin),'db, Gain max = ',num2str(G3dmax),'db']);
disp(' ');

60 filePath = 'D:\Documents\Research\Thesis\Results\IDS\ChipOnly\';
fileName = 'Gain3D_ChipOnly_3mm_33nH_905MHz_15p1MHz.csv';
[G3davg,G3dmin,G3dmax] = G3dinfo([filePath,fileName]);
disp(fileName);
65 disp(['MEG gain = ',num2str(G3davg),'db, Gain min = ',...
num2str(G3dmin),'db, Gain max = ',num2str(G3dmax),'db']);
disp(' ');

filePath = 'D:\Documents\Research\Thesis\Results\IDS\Electronics\';
70 fileName = 'Gain3D_Electronics_2p6mm_910MHz_12MHz_36nH.csv';
[G3davg,G3dmin,G3dmax] = G3dinfo([filePath,fileName]);
disp(fileName);
disp(['MEG gain = ',num2str(G3davg),'db, Gain min = ',...
num2str(G3dmin),'db, Gain max = ',num2str(G3dmax),'db']);
75 disp(' ');

```

## A.5. MEG Function

```
1  function [G3davg,G3dmin,G3dmax] = G3dinfo(file)
   % [G3davg,G3dmin,G3dmax] = G3dinfo(file)
   % Provided a file string, this function displays the MEG (avg) over the
   % full spherical surface.
5  % Layne Berge November 29th, 2012

   % Parse data from csv
   data = csvread(file,1,0);
   % Grab gain data from file
10  gain = data(:,3);

   % Find minimum gain
   G3dmin = min(gain);
   % Find maximum gain
15  G3dmax = max(gain);

   % Reset collection variable
   gainSum = 0;
   % Reset index
20  numPoints = 0;
   % For loop parses through all 3D gain data
   for index = 1:length(data)
       % If theta > 180, step phi
       if data(index,2) == 180
25         break
       end
       % If data is non-repeated (phi = 0 = 360, theta = 0) calculate MEG
       if (data(index,1) ~= 360) * (data(index,2) ~= 0)
           gainSum = gainSum + data(index,3) * sin(pi * data(index,2) / 180);
30         numPoints = numPoints + 1;
       end
   end
   end
   % Calculate average gain
   G3davg = gainSum / numPoints;
```

## APPENDIX B. PYTHON CODE

This appendix contains all of the Python code used in this work. The python code was responsible for creating the maximum read range plots.

### B.1. Measured Maximum Read Range Plotting

```
1  # -*- coding: utf-8 -*-
   """
   Created on Wed Dec 19 22:01:34 2012

5  This script reads in the data output from the USRP1 test setup and
   parses it based upon the desired frequency set below. It then
   calculates the maximum read range and plots a logarithmic polar plot
   of the maximum read range at every angular location from the test.

10 @author: mike.reich
   Edited by: Layne Berge on January 29th 2013
   """
   import os
   import glob
15  import csv
   import numpy as np
   import matplotlib
   from matplotlib.pyplot import figure, show, rc, grid

20  #Plot Settings

   RMIN = 000
   RMAX = 5000
   RSTEP = 1000

25  def read_cal_file(freq, cal_file):

   f = csv.reader(open(cal_file))

30  for line in f:
   # Check for comment indicator (! as first char on line)
   if line[0][0] != "!":
       line_data = [float(i) for i in line]

35  # Check for the frequency of interest and extract
   if line_data[0] == freq:
       cal_value = line_data[1]

   return cal_value

40  def read_csv(freq, path):
   # Note that creating arrays like this and then appending to them
   # is very memory inefficient, but we aren't dealing with huge
```

```

# amounts of data so efficiency is not as important in this case
45 angles = np.empty(0)
points = np.empty(0)

for infile in glob.glob( os.path.join(path, '*.csv') ):
    #print "current file is: " + infile
50
    # Opens and properly closes CSV file
    with open(infile) as z:
        f = csv.reader(z)

55        for line in f:

            # Check for comment indicator (! as first char on line)
            if line[0][0] == "!":

60                # Look for the 'Angle' keyword
                substr = line[0][1:6]

                # If you found the keyword, extract the angle
                if substr == "Angle":
65                    n = len(line[0])
                    angles = np.append(angles,...
                    float(line[0][7:n])*np.pi/180)

                # Otherwise you are scanning through the data
70                else:
                    line_data = [float(i) for i in line]

                    # Check for the frequency of interest and extract
                    if line_data[0] == freq:
75                        m = len(line_data)
                        points = np.append(points, line_data[m-2])

#points = points/max(points)

80 # append the first data points to the end so that we get a
# continuous plot
points = np.append(points, points[0])
angles = np.append(angles, 2*np.pi)

85 pattern = np.array([angles,points]).T

return pattern[pattern[:,0].argsort()]

def map_nulls(a):
90 # This is a hack, but should work for now
for index, point in enumerate(a[:,1]):
    if (point == 20):
        print "Null Angle = " + str(index*10)
        #a[index,1] = RMIN
95        a[index,1] = 100

```

```

        return a

def db2linear(db):
100     return 10**(db/10)

def compute_read_range(d, EIRP, Pmin, L, Gt):
105     Pmin = db2linear(Pmin+L)/1000.0
        Gt = db2linear(Gt)

        print ("Pmin =" +str(Pmin))
        print ("Gt = " + str(Gt))
110

        r = d*np.sqrt(EIRP / (Pmin*Gt))
        print ("r max = "+ str(max(r)))
        print ("r min = "+ str(min(r)))
        return r
115

def main():

    FREQ = 915     # Sets the frequency you want to plot
    EIRP = 4.0     # EIRP in watts for baseline comparison
120    TX_GAIN = 6.0 # Transmit antenna gain in dBi
    DIST = 0.47   # Baseline distance in meters from tx antenna to tag
    SHIFT1 = 0
    FLIP1 = 0
    SHIFT2 = 0
125    FLIP2 = 0
    SHIFT3 = 0
    FLIP3 = 0
    SHIFT4 = 0
    FLIP4 = 0
130

    PATH1 = '../Testing/Interpolated/Sphere1/XY/'
    PATH2 = '../Testing/Interpolated/Sphere2/XY/'
    PATH3 = '../Testing/Interpolated/Sphere3/YZ/'
135    PATH4 = '../Testing/Interpolated/Sphere4/YZ/'

    cal_file = './cal_data.csv'
    cal_factor = read_cal_file(FREQ, cal_file)

140    p1 = read_csv(FREQ, PATH1)
        p2 = read_csv(FREQ, PATH2)
        p3 = read_csv(FREQ, PATH3)
        p4 = read_csv(FREQ, PATH4)

145    p1 = map_nulls(p1)
        p2 = map_nulls(p2)
        p3 = map_nulls(p3)

```



```

p4 = map_nulls(p4)

150 k1 = compute_read_range(DIST, EIRP, p1[:,1], cal_factor, TX_GAIN)
k2 = compute_read_range(DIST, EIRP, p2[:,1], cal_factor, TX_GAIN)
k3 = compute_read_range(DIST, EIRP, p3[:,1], cal_factor, TX_GAIN)
k4 = compute_read_range(DIST, EIRP, p4[:,1], cal_factor, TX_GAIN)

155 p1[:,1] = k1
p2[:,1] = k2
p3[:,1] = k3
p4[:,1] = k4
# Need to transpose array back so plotting works
160 p1 = p1.T
p2 = p2.T
p3 = p3.T
p4 = p4.T

165 ind = np.argwhere(p1[0,]==SHIFT1*np.pi/180)
endp1 = np.size(p1[1,:])
p1[1,:] = np.concatenate((p1[1,ind:endp1],p1[1,0:ind]),0)
print p1[1,:]
if(FLIP1 == 1):
170 p1[1,:]=p1[1,::-1]
print p1[1,:]
p1[1,0] = p1[1,endp1-1]

ind = np.argwhere(p2[0,]==SHIFT2*np.pi/180)
175 endp2 = np.size(p2[1,:])
p2[1,:] = np.concatenate((p2[1,ind:endp2],p2[1,0:ind]),0)
if(FLIP2 == 1):
p2[1,:]=p2[1,::-1]
180 p2[1,0] = p2[1,endp2-1]

ind = np.argwhere(p3[0,]==SHIFT3*np.pi/180)
endp3 = np.size(p3[1,:])
p3[1,:] = np.concatenate((p3[1,ind:endp3],p3[1,0:ind]),0)
if(FLIP3 == 1):
185 p3[1,:]=p3[1,::-1]
p3[1,0] = p3[1,endp3-1]

ind = np.argwhere(p4[0,]==SHIFT4*np.pi/180)
endp4 = np.size(p4[1,:])
190 p4[1,:] = np.concatenate((p4[1,ind:endp4],p4[1,0:ind]),0)
if(FLIP4 == 1):
p4[1,:]=p4[1,::-1]
p4[1,0] = p4[1,endp4-1]

195 # FIXME need to change horizontal axis thickness to match
# rest of grid

rc('grid', linewidth=1, linestyle='-')
rc('axes', linewidth=1)

```

```

200     rc('xtick', labelsize=15)
        rc('ytick', labelsize=15)

        # force square figure and square axes looks better for polar, IMO
205     width, height = matplotlib.rcParams['figure.figsize']
        size = min(width, height)
        # make a square figure
        fig = figure(figsize=(size, size))
        #ax = fig.add_axes([0.1, 0.1, 0.8, 0.8], polar=True, axisbg='#d5de9c')
210     ax = fig.add_axes([0.1, 0.1, 0.8, 0.8], polar=True)

        # BEGIN APP
        fig.set_facecolor('white')
        ax.set_theta_direction(-1) # clockwise rotation
215     ax.set_theta_offset(np.pi/2) # Set theta zero location
        ax.plot(p1[0,:], p1[1,:]*1000, linewidth=3, linestyle='--',...
                color='k',label='Sphere1')
        ax.plot(p2[0,:], p2[1,:]*1000, linewidth=3, linestyle='--',...
                color='r',label='Sphere2')
220     ax.plot(p3[0,:], p3[1,:]*1000, linewidth=3, linestyle='-.',...
                color='b',label='Sphere3')
        ax.plot(p4[0,:], p4[1,:]*1000, linewidth=3, linestyle=':',...
                color='g',label='Sphere4')
        ax.legend(loc="center")
225     # END APP

        ax.set_rscale('log')
        #ax.set_ylim(RMIN,RMAX)
        #ax.set_ylim(10,10000)
230     ax.set_yticks([10, 100,1000,10000])
        ax.yaxis.set_major_formatter(matplotlib.ticker.NullFormatter())
        ax.text(0.55,0.65,'10', ha='center', va='center',...
                transform=ax.transAxes, fontsize=15)
        ax.text(0.60,0.77,'100', ha='center', va='center',...
235     transform=ax.transAxes, fontsize=15)
        ax.text(0.65,0.89,'1000', ha='center', va='center',...
                transform=ax.transAxes, fontsize=15)
        ax.text(0.70,1.01,'10000', ha='center', va='center',...
                transform=ax.transAxes, fontsize=15)
240     #ax.yaxis.set_major_locator(matplotlib.ticker.LinearLocator())
        #ax.set_yticks(np.arange(RMIN+RSTEP,RMAX,RSTEP))

        grid(True)
        show()
245     print "Done"

    if __name__ == "__main__":
        main()

```